Narodowe Centrum Badań Jądrowych
National Centre for Nuclear Research
ŚWIERK

NATIONAL CENTRE FOR NUCLEAR RESEARCH

DOCTORAL THESIS

Front-end investigations of the coated particles nuclear fuel for high temperature gas cooled reactors.

mgr inż. Zuzanna Maria Krajewska

A thesis submitted in fulfillment of the requirements for the degree of Doctor of Physical Sciences in the National Centre for Nuclear Research

Supervisor: prof. dr hab. inż. Wacław Gudowski

Auxiliary supervisor: dr Agnieszka Boettcher

Warszawa 2023

Acknowledgments

I would like to sincerely express my grateful gratitude to my supervisor Prof. Wacław Gudowski for his scientific supervision, understanding, patience, trust, and all the help given to me in the completion of this work.

Furthermore, I would like to express my appreciation to everyone with whom I had the privilege to collaborate during my Ph.D., in particular, dr. Tomasz Buchwald, prof. Tomasz Tokarski, prof. Marcin Turek, dr. Krzysztof Pyszniak, and dr. Andrzej Drożdziel - thank you for the fruitful cooperation.

I would like to extend my deepest gratitude to my family and those closest to me for their encouragement and support during these years.

I would like to express my deepest respect and gratitude to my mom and dad for supporting me in difficult moments, and for their priceless suggestions, patience, and unlimited amounts of love.

TABLE OF CONTENTS

LIST OF FIGURES

LIST OF TABLES

ACRONYMS

AGR	Advanced Gas Rectors
AVR	Arbeitsgemeinschaft Versuchs Reaktor
BAF	Bacon Anisotropy Factor
BISO	Bistructural Isotropic
BWR	Boiling Water Reactors
CLSM	Confocal Laser Scanning Microscope
C2N	Coal-to-Nuclear
DOE	Department of Energy
DPA	Displacement per Atom
E_D	Threshold Displacement Energy
EPMA	Electron Probe Micro Analyzer
FC	Detailed Calculation with full Damage Cascades
FCM	Fully Ceramic Microencapsulated
FIB	Dual-beam focused ion beam

FP	Fission Products
GEN-IV	Generation IV
GFR	Gas-Cooled Fast Reactor
GIF	Generation IV International Forum
HM	Heavy metal
HTGR	High Temperature Gas-cooled Reactor
HTR	High Temperature Reactor
HTTR	High Temperature engineering Test Reactor
ID/IG	Intensity ratio of the D-Raman band and G-Raman band
INL	Idaho National Laboratory
LFR	Lead-Cooled Fast Reactor
LWR	Light Water Reactors
IPyC	Inner Pyrolytic Carbon
MCB	Monte Carlo Continuous Energy Burn-up
MCNP	Monte Carlo N-Particle Transport Code
MGR	Monitored Geologic Repository
MOX	Mixed Oxide Fuel
MSR	Molten Salt Reactor
NCBiR	National Centre for Research and Development
NCBJ	National Centre for Nuclear Research
NRT	Norgett, Robinson, and Torrens formalism
OPyC	Outer Pyrolytic Carbon
PIE	Post Irradiation Examination
PKA	Primary Knock-on Atom
PPEJ	Polish Nuclear Power Program
PWR	Pressurized Water Reactor
PyC	Pyrocarbon
QA	Quality Assessment
QC	Quality Control

QD	Ion Distribution and Quick Calculation of Damage
R&D	Research and Development
SCWR	Supercritical-Water-Cooled Reactor
SEM	Scanning Electron Microscopy
SFR	Sodium-Cooled Fast Reactor
SiC	Silicon Carbide
SMR	Small Modular Reactor
SRIM	Stopping and Range of Ions in Matter
TEM	Transmission Electron Microscopy
TRIM	Transport and Range of Ions in Matter
TRISO	Tristructural Isotropic
UCO	Uranium Carbon Oxide
UKAEA	United Kingdom Atomic Energy Authority
USNC	Ultra Safe Nuclear Corporation
VHTR	Very-High-Temperature-Reactor
XRD	X-Ray diffraction
ZrC	Zirconium carbide

Author's contribution

The present dissertation based on the listed publications:

List of journal publications:

1. Z.M. Krajewska, W. Gudowski, Raman Spectroscopy Studies of TRISO -Particle Fuel, International Conference on High Temperature Reactor Technology (HTR) 2021, Journal of Physics: Conference Series, 2048 (2021) https://iopscience.iop.org/article/10.1088/1742-6596/2048/1/012007 (IF: 0.55).

2. Z.M. Krajewska, T.Buchwald, T. Tokarski, W. Gudowski, Front -end investigations of the coated particles of nuclear fuel samples – ion polishing method, Nuclear Engineering and Technology, Vol.54, p.1935-1946 (2022) https://doi.org/10.1016/j.net.2021.12.003 (IF: 2.34).

3. Z.M. Krajewska, M. Górkiewicz, W. Gudowski, Fluence calculations for the TRISO-particle fuel ion implantation - submitted to Journal

4. Z.M. Krajewska, T.Buchwald, A. Droździel, W. Gudowski, K. Pyszniak, T. Tokarski, M. Turek, Mechanical defects in the p-TRISO-particle covering layers obtained through the ion implantation process - submitted to Journal

5. Z.M. Krajewska, T.Buchwald, A. Droździel, W. Gudowski, K. Pyszniak, T. Tokarski, M. Turek, The Influence of the Ion Implantation on the Degradation level of the Coated Particles of Nuclear Fuel Samples, Coatings 13, 556 (2023) https://doi.org/10.3390/coatings13030556 (IF: 3.24).

List of conference papers:

6. P. Temocin, Z.M. Krajewska, Socio-political and Technical Aspects for Nescent Nuclear Projects, NEREC Annual Report, p.235-246 (2019)

7. Z.M. Krajewska, T. Buchwald, W. Gudowski, The Influence of Aging Process on the Degradation of the Coated Particles of Nuclear Fuel Samples, Proceedings of ICAPP, Paper 21625 (2021)

ABSTRACT

The TRIstructural ISOtropic (TRISO) fuel, composed of a uranium kernel covered with silicon carbide (SiC) and pyrolytic carbon (PyC) coating layers, serves as the smallest component of the nuclear fuel. Thousands of the TRISO-particles are immersed in the graphite matrix, taking the form of a sphere (pebble bed reactor type) or pellet (prismatic reactor type), which are used in High-Temperature Gas-cooled Reactors (HTGRs). Due to the fuel irradiation in the reactor core, partial or complete damage to the covering TRISO layers might occur. The examination of the defects occurring in the TRISO layers is a key aspect of a good understanding of the failure-free performance of TRISO-particle fuel and is key to the safe and efficient operation of the HTGRs.

The damage-rate measurements of the TRISO-particle layers are performed at the production stage and after extracting the irradiated fuel from the reactor core. Neutron irradiation is a long-term process. The experimental, ion-irradiation method, which is suggested in the dissertation, allows the verification of the level of damage in the coating layers, without the need to deal with activated material. In addition, this method is an effective tool to reflect the neutron irradiation damage in the reactor core, by radically shortening the time for inducing damage.

The examination of the TRISO samples was carried out at the front-end stage. The purpose of this research was to verify the coating layers for damage occurrence, before the TRISO-particle fuel is placed in the reactor core, but under conditions corresponding to the irradiation of the fuel in the reactor core. The front-end stage is the initial analysis of the failure rates of freshly manufactured or stored but unirradiated samples. The experiments were performed on surrogate in-process coated particles, called p-TRISO. The unique feature of p-TRISO-particles is the absence of uranium in the kernel, which was replaced by zirconia dioxide. The p-TRISO samples were produced in 2001, retained, and never used.

The ion-irradiation experiments were conducted on both polished and unpolished p-TRISO samples, implanted with Ne^+ and He^+ ions of specific fluences and energy. The purpose of this experiment was to capture the point at which damage starts to occur to the individual layers, as well as to understand the appearance of damage at the interface of the Buffer-IPyC layers. Several diagnostic methods such as Raman spectroscopy, Scanning Electron Microscopy (SEM), and Confocal Laser Scanning Microscopy (CLSM) were used.

The performed research determines whether and how the passage of time affects the occurrence of changes in the p-TRISO fuel layers structure, and at the same time, whether it contributes to increasing the probability of damage to the examined fuel material. The experiment confirmed that significant structural changes appear after one year of ion irradiation of the samples. Significantly, with further time (i.e., after 3 and 5 years) of irradiation, no noticeable changes were observed in the p-TRISO coating layers (in comparison to the changes observed after 1 year of irradiation). Moreover, it should be taken into account that the experiments were performed on 22-year-old TRISO-particle fuel samples. Therefore, the results of the experiment allow us to conclude that also the stored but unirradiated fuel can be effectively used as fuel in the reactor core. However, the results obtained in the mentioned scope should be compared with freshly manufactured TRISO samples within the occurrence of damage in the coating layers. Then, the question of whether the damage in the TRISO sample layers is more progressive in "old" (stored, but unirradiated) fuel than in "new" (freshly manufactured) fuel could be answered. Such research, however, was not the subject of this dissertation. Nevertheless, it should be undertaken in the future.

This work confirmed that an ion irradiation technique is a quick and efficient tool for reflecting irradiation-induced damages in the p-TRISO sample layers. This method can be used at the front-end stage, to determine if the stored but unirradiated TRISO-particles pass the quality control and could be placed in the reactor core.

STRESZCZENIE

Paliwo TRISO to izotropowe, trój-strukturalne paliwo jądrowe, które składa się z jądra na bazie uranu otoczonego tzw. warstwami okrywającymi, do których należy węgiel pyrolityczny oraz węglik krzemu. Cząsteczki paliwowe TRISO są najmniejszym składnikiem budującym tego rodzaju paliwa. Tysiące cząsteczek paliwa TRISO jest zanurzonych w matrycy grafitowej, formując kulę - wykorzystywaną jako paliwo w reaktorze o złożu kulowym lub pastylkę paliwową - wykorzystywaną w reaktorze pryzmatycznym. Obie formy paliwa są charakterystyczne dla wysokotemperaturowych reaktorów chłodzonych gazem, tzw. HTGR-ów. W wyniku procesu napromieniowania paliwa w rdzeniu reaktora, może dojść do częściowego lub całkowitego uszkodzenia warstw okrywających cząsteczek TRISO. Badanie powstałych defektów w warstwach okrywających TRISO jest kluczowym aspektem dobrego zrozumienia bezawaryjnej pracy tego paliwa, a także ma kluczowe znaczenie dla bezpiecznego i wydajnego funkcjonowania reaktorów typu HTGR.

Co do zasady, badanie potencjalnych uszkodzeń warstw okrywających TRISO odbywa się na etapie produkcji lub dopiero po wydobyciu paliwa z rdzenia reaktora, tzn. po okresie jego napromieniowania. Z uwagi na fakt, iż proces napromieniowania neutronowego jest długotrwały, w niniejszej rozprawie proponuje się alternatywną metodę badania, w postaci implantacji jonowej. Metoda ta pozwala odzwierciedlić zjawisko napromieniowania paliwa w rdzeniu reaktora. Tym samym wiedzę na temat potencjalnych uszkodzeń warstw okrywających paliwa TRISO możemy uzyskać nie tylko w znacznie krótszym czasie, ale także bez konieczności obcowania z materiałem radioaktywnym.

W niniejszej rozprawie doktorskiej skupiono się na wstępnych badaniach jakości paliwa TRISO, tzn. na etapie front-end. Celem tego etapu badawczego jest zweryfikowanie warstw okrywających, pod kątem występowania uszkodzeń, jeszcze przed umieszczeniem paliwa TRISO w rdzeniu reaktora, ale w warunkach odpowiadających napromieniowaniu paliwa w rdzeniu reaktora. Taka diagnostyka cząstek TRISO może być prowadzona zarówno na świeżo wyprodukowanym paliwie jak i na paliwie zmagazynowanym i wcześniej niewykorzystywanym. W niniejszej rozprawie prowadzono badania na tzw. surogatach paliwa, nazwanych paliwem p-TRISO. Cechą szczególną cząsteczek p-TRISO jest brak uranu w jądrze, który został zastąpiony tlenkiem cyrkonu. Próbki tego paliwa zostały wyprodukowane w 2001 r., od tamtego czasu były wyłącznie przechowywane.

Podstawę badania stanowił eksperyment z wykorzystaniem techniki implantacji jonowej, przeprowadzony zarówno na przepolerowanych jak i na niepolerowanych próbkach paliwa p-TRISO. Cząsteczki p-TRISO były implantowane za pomocą jonów neonu i jonów helu o odpowiednio dobranej energii i fluencji. Celem badania było wychwycenie momentu, w którym dochodzi do powstania uszkodzenia pojedynczej warstwy okrywającej, a tym samym, zrozumienie powstawania uszkodzeń na styku dwóch warstw (tj. Buffer i IPyC). Jako metody diagnostyczne wykorzystano: spektroskopię Ramana, skaningowy mikroskop elektronowy czy też konfokalny mikroskop materiałowy.

Przeprowadzone w ramach doktoratu badania pozwoliły określić, czy i jak upływ czasu wpływa na powstawanie zmian w strukturze warstw okrywających paliwa TRISO oraz czy i jak upływ czasu wpłynął na wzrost prawdopodobieństwa uszkodzenia badanego paliwa. W eksperymencie potwierdzono, że znaczące zmiany strukturalne pojawiają się po upływie roku od napromieniowania próbek. Co istotne, wraz z dalszym okresem (tj. po upływie 3 i 5 lat) napromieniowania próbek, nie zaobserwowano zauważalnych zmian w warstwach okrywających paliwa p-TRISO, w stosunku do zaobserwowanych zmian po upływie 1 roku. Należy mieć na uwadze, iż eksperymenty przeprowadzono na 22-letnich próbkach paliwa p-TRISO. Wyniki eksperymentu pozwalają zatem uznać, że również paliwo zmagazynowane można efektywnie wykorzystać jako paliwo umieszczane w rdzeniu reaktora. Oczywiście otrzymane wyniki w ww. zakresie, dot. uszkadzania się warstw okrywających próbek p-TRISO, należałoby potwierdzić porównując je z wynikami otrzymanymi dla świeżo wyprodukowanych cząsteczek paliwa TRISO. Wówczas możliwe byłoby otrzymanie odpowiedzi na pytanie, czy uszkodzenia w warstwach TRISO postępują w takim samym stopniu w „starym" paliwie (np. zmagazynowanym) jak i w „nowym" (tj. świeżo wyprodukowanym). Badania takie nie były jednak przedmiotem niniejszej rozprawy, niemniej jednak powinny zostać podjęte w przyszłości.

Niezależnie od powyższego, przeprowadzony eksperyment potwierdził przyjętą w rozprawie tezę, że metoda implantacji jonowej jest szybkim i efektywnym narzędziem pozwalającym odzwierciedlać uszkodzenia w warstwach okrywających paliwa TRISO. Metoda ta może być wykorzystana na etapie wstępnych badań paliwa, w celu weryfikacji jakości paliwa TRISO oraz określenia czy paliwo kwalifikuje się do umieszczenia w rdzeniu reaktora.

1. INTRODUCTION

Poland faces very difficult challenges and an urgent need for energy transformation. It is not only for climate and environmental reasons, it is also because it has an aging energy park that requires an immediate replacement. First, replacing coal-burning plants with nuclear power plants will reduce the greenhouse effect by reducing CO_2 production. Second, it would provide support for renewable energy stabilizing the electricity grid and providing a reliable stable base load for the grid. Thirdly, it could be used for combined power and heat generation, providing emission-free energy for hydrogen production, synthetic fuel production, and many other energy intense industries.

In November 2022 the cooperation agreement between Poland and the United States of America to build the first nuclear reactor (advanced Light Water Reactor (LWR) - Westinghouse AP1000) in Poland has been signed. The first attempt to construct a nuclear power plant in Poland took place in the 1980s, however, the impact of the Chernobyl accident, and later political transformations in Poland and other Central European countries caused the project to be completely abandoned. Suspended for years, the plan for the construction of the Polish nuclear power plant was reopened in the 2000s, as the Polish Nuclear Power Program (PPEJ) [1]. The objective of the PPEJ is to construct and commission Generation III+ nuclear power plants. Generation IV reactors, such as High Temperature Gas-cooled Reactors (HTGR) are also considered for development in the future. Implementation of these technologies will reduce Poland's demand for natural gas and lower CO_2 emissions. The main driver for the deployment of HTGRs in Poland is the need for emission-free industrial heat, in the chemical and heavy industries. The HTGRs could also take a place of retired coal power plants, as a part of a coal-to-nuclear (C2N) transition [2]. Moreover, they would find applications in hydrogen production, which is needed in refineries and the chemical industry.

For both research and industrial HTGR projects, an important issue is to acquire the typical for these reactor types nuclear fuel, called TRI-structural Isotropic (TRISO)- particle fuel. The TRISO-particle fuel is currently experiencing a renaissance. This fuel can be used not only in HTGR-type nuclear reactors, but also in LWRs [3][4] or Small Modular Reactors (SMR) of different types [5], and also has applications in space [6]. The leading companies exploiting the potential of TRISO fuel, such as X-energy [7], Kairos Power [8], U-Battery [9], BWX Technologies [10], and Ultra Safe Nuclear Corporation (USNC) [11], work intensively on improving the quality of TRISO-particle fuel. A new concept of HTGR

fuel - Fully Ceramic Microencapsulated (FCM) fuel, has been developed by the USNC. In the FCM fuel, the TRISO-particles are overcoated by a high-density SiC matrix, which should withstand high temperatures, preventing the fission product release [12][13][14][15]. For these reasons, sourcing fuel from third-party suppliers would be the most optimal for Poland's HTR program, because purchasing fuel from politically and economically reliable countries would ensure at least at the first stage a secure supply of this fuel for the HTGR. The second option is to produce the fuel in Poland, which will guarantee independence. The eventual production of the TRISO fuel in Poland will require the establishment of a dedicated laboratory and a production line. The mission for a TRISO laboratory would be:

- the development of quality control (QC) and quality assessment (QA) methods for the TRISO-particle fuel. The aim is to prove to the Polish regulatory body that the TRISO fuel performance is adequate and complies with safety regulations. This part will be focused on the unirradiated TRISO-particles, called the front-end stage of the HTGR nuclear fuel cycle;
- the irradiation of the TRISO-particles fuel under very well-controlled conditions in the MARIA research reactor. Supplementary, Post-Irradiation Examinations (PIE) of the TRISO-particle fuel would be performed;
- the investigation of irradiated TRISO-particles with a focus on their performance as spent fuel for final disposal. The ultimate objective will be to develop an acceptable (socially and technically), proven, and economically viable concept of the final disposal of the HTGR spent fuel [16].

Large knowledge and modeling base exists on the behavior of TRISO-coated particle fuel under irradiation as well as under accident conditions, and numerous benchmarking studies comparing experimental results and calculations on TRISO-particle failures show that failure mechanisms are well understood. The Advanced Gas Rectors (AGR-1 and AGR-2) experiments on TRISO fuel conducted at Idaho National Laboratory (INL) have confirmed that the probability of damage to this fuel is very low. The PIE studies show that irradiation in the reactor core results in the partial or complete formation of a gap between Buffer-IPyC layers, as well as IPyC-SiC layers, which can lead to further damage (cracks) and release of fission products. Within reactor neutron irradiation experiments of TRISO-particle fuels are difficult because such experiments are expensive, and are a very time-consuming processes. The irradiation cycle lasts for 3-5 years [17][18][19]. After that, the spent fuel might be reprocessed, stored in the Monitored Geologic Repository (MGR) – short-term, or stored on-site – long-

term. At the current moment storing spent fuel is a more popular option, due to the fact that the reprocessing of TRISO fuel (separation of the TRISO-particles from the graphite matrix) is still a challenging process [20][21][22]. In terms of social and economic aspects, it is necessary to develop the technology for uranium recycling from the spent fuel, as well as the reprocessing of stored TRISO fuel. The examination of damage that occurs in TRISO layers (especially damage to TRISO-coating layers after removal of irradiated fuel from the reactor core) is a key aspect of a good understanding of the failure-free performance of TRISO-particles fuel, as well as a key to the safe and efficient operation of HTGRs.

This thesis is an additional source of new empirical knowledge in the field of diagnostic methods for TRISO fuel focusing on Raman spectroscopy and ion irradiation. The experimental ion irradiation method proposed here makes it possible to verify the level of damage in the coating layers, i.e. Buffer and IPyC, without the necessity of interacting with the activated material. In addition, this method is an effective tool for reflecting neutron irradiation damage in the reactor core by radically reducing the damage induction time. The experiments were conducted on surrogate particles called p-TRISO. The p-TRISO samples were manufactured in 2001, retained, and never used. Ion irradiation experiments were conducted on polished and unpolished p-TRISO samples implanted with Ne^{+} and He^{+} ions of specific fluences and energies. The use of stored but unirradiated fuel (rather than newly produced) is a deliberate effort to achieve the intended purpose of the work, i.e. to determine whether the passage of time affects the occurrence of changes in the structure of TRISO fuel layers, and at the same time whether it contributes to the likelihood of damage to the fuel material under study. Another cognitive goal of the work is to gain new empirical knowledge about a poorly studied aspect of the damage, which is capturing the moment when damage occurs at the Buffer-IPyC layer interface.

This dissertation aimed at two practical goals. First, to derive conclusions from empirical analysis on the modification of QC and QA methods for TRISO-particle fuel. Second, to detect damaged TRISO-particles before placing them into reactor core (front-end investigation). In specific, for the production laboratory. These goals were supported by seeking answers to the following questions:

- Whether or not structural damages may be detected based on Raman spectroscopy?
- Whether the ion irradiation method can mimic the neutron irradiation in the reactor core?

The answers to these questions are expected to support the thesis that ion irradiation and Raman spectroscopy methods are quick and effective diagnostic methods of TRISO-particle fuel.

The objectives of the work are in harmony with the research methodology and are arranged in the following sequence of activities:

- gathering information on TRISO fuel and surrogate particles, called p-TRISO;
- preparation of the material for examination - mechanical and ionic polishing;
- ion implantation (determination of the ion fluence needed for the ion irradiation experiment);
- case analysis;
- derivation of conclusions.

The investigation of TRISO fuel failure as described here enables the modification of QC and QA methods, which makes possible the detection of damaged fuel before being placed in a reactor core. To achieve the intended research goals, the following diagnostic tools were used such as ion implantation - to reflect neutron irradiation, Raman spectroscopy - to measure defects, and SEM - to visualize the structure. The layout and content of the dissertation derive from the stated goals. The dissertation consists of 7 chapters. Chapter 2 focuses on the general knowledge of the neutron and ion interactions with matter and the reactor technology, with the distinction of the HTGR technology. Chapter 3 presents in detail the TRISO-particle fuel. In Chapter 4 the diagnostic tools used in the experiments are described. Finally, Chapter 5 explains the performed experiment on p-TRISO samples. In Chapter 6 the results obtained based on performed experiments are summarized. The last chapter shows the literature based on which the papers and the dissertation were possible to describe.

2. DESCRIPTION OF THE MATERIAL DAMAGE PROBLEM

During nuclear reactor operation partial damage or weakening of the structure of nuclear materials like graphite, etc. may happen. Understanding the radiation effects on the structural materials is a key factor to improve the quality of the materials placed in the reactor core. In this dissertation, two mechanisms of defect-induced formation were selected, such as neutrons and ions. Both of these forms of radiation might displace the atoms from their lattice structure. Presented thesis shows, based on performed experiments, that ion implantation can effectively reflect the neutron irradiation process. The Displacement Per Atom (DPA) factor was used to find the connection between neutrons and ions.

2.1. NEUTRON INTERACTIONS WITH MATTER

Nuclear fuel consists of uranium. Natural uranium contain of 99.3% ^{238}U and 0.7% ^{235}U, too little too sustain fission chain reaction in light water cooled reactors, therefore most reactors use the enriched (level of 3–5 %) uranium [23][24]. The other fissile materials are ^{233}U, ^{239}Pu and ^{241}Pu and they do not exist naturally, but can produced through neutron capture reactions. In a nuclear reactor, a self-sustaining fission chain reaction generates energy, it involves the fission of the ^{235}U nucleus, which occurred after the capture of one thermal neutron, producing several (the average 2.47) fast neutrons, belonging to the next generation. ^{235}U is the primary fissile material that drives nuclear power generation. It split into two parts, giving rise to two new nuclei, energy and a number of new highly energetic neutrons. Each generation of neutrons creates the following generation. A ratio of neutrons in the next generation to neutrons in the previous generation is called as multiplication factor *k*. When more neutrons are produced than are consumed than the neutron population grows (k>1 = supercritical); and when fewer neutrons are produced than are consumed than the neutron population shrinks (k<1 = subcritical). In the situation when neutron population is in balance the *k* factor is equal to 1 (critical).

Any type of interaction of neutrons with matter, such as graphite, can cause radiation damage. Neutrons transfer their kinetic energy to the atoms of the target material, then form vacancies, which are responsible for the formation of clusters of defects or microstructural changes. Neutrons can cause two types of damage in carbon-based materials, such as a ballistic damage, which causes atomic displacements, or the excitations and ionizations generated by electronic interactions with recoil atoms [25][26][27].

Radiation damage analysis is possible only during the PIE, after the irradiation process. For these reasons, the use of the ion implantation technique makes it possible to reflect the damage induced by neutrons. Ion beam irradiation can produce cascades that are similar to those created by neutrons in the nuclear reactor.

Ions are formed by the addition (positively charged ions – cations) or removal (negatively charged ions – anions) of an electron to the neutral atoms or molecules. They can serve as a surrogate for neutron irradiation and damage formation, without activation of the irradiated materials. To produce radiation damages similar to those produced in nuclear reactors, the energy and fluence of incident ions are described in this thesis Chapter 5.2.

The radiation damage is initiated by the energy transfer of an energetic particle like a neutron or ion to the target material. The damage formation process has been described in terms of ions. Ion irradiation involves displacing an atom from its place in the lattice, leaving a vacant space (vacancy). The displaced atom can rest in a place that is between the lattice sites, creating the interstitial atom. The vacancy-interstitial pair is central to radiation effects in the crystalline structure and is known as the Frenkel pair. The stable point defects Frenkel pairs involve the displacement of an atom from a lattice node to an inter-nodal position. When the place left by the knocked-out atom is occupied by an ion from the bombarding beam, and an atom of the lattice material lodges in the inter-nodal position, such a collision is called a basal collision. The other point defect that can arise from the interaction of an energetic ion with the target is the Schottky effect (vacancy creation), which is characterized by the absence of an atom at a lattice node. As a result of the elastic collision of an ion with a target atom, that atom can be displaced from its nodal position, and therefore a radiation defect might occur. The process of ion implantation is accompanied by the phenomenon of defecting of the irradiated target. The number and type of defects produced along the path of the penetrating ion sample depend on the mass, charge, energy, and fluence of the implanted ions. Additional factors include the mass of the target, crystal structure, and temperature. In order for a chemical bond to be broken and an atom to be displaced from a node of the crystal lattice structure, the energy transmitted by the ion to the lattice atom must be greater than the threshold displacement energy (E_D). The radiation damage event, known as displacement cascade, is formed by the primary knock-on atom (PKA), which may further displace other atoms in the lattice, which is present in Fig. 2. 1. The PKA is an atom in the target material which interacts with the incident particle, and by receiving energy greater then E_D it leaves the lattice site. The whole event lasts about 10^{-11} s [24][28]. Nevertheless, the knocked-out atoms which have sufficiently high energy

become secondary projectiles. They are then able to cause the displacement of neighboring lattice atoms, i.e., they can create the formation of a so-called knock-out cascade. The remaining PKA might combine and agglomerate into clusters or generate micro-structural changes, which depend on the initial amount of defects and the temperature [29]. We can distinguish three classes of ion–atom collisions:

- 1st - light energetic ions - $E_i > 1$MeV;
- 2nd - highly energetic heavy ions - $E_i \sim 100$MeV;
- 3rd - lower energy heavy ions - $E_i < 1$MeV.

The 3rd class of ions can be produced by an accelerator, and this type of ions was used in the experiment presented in this dissertation.

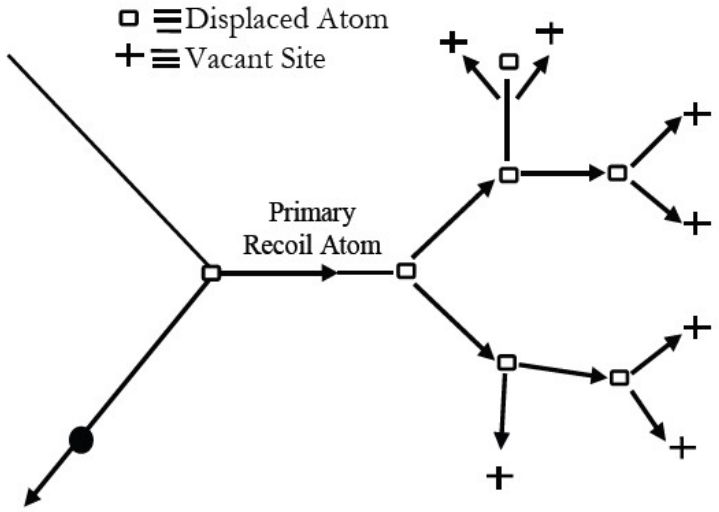

FIG. 2. 1 SCHEMATIC REPRESENTATION OF THE FORMATION OF DISPLACEMENT CASCADE BY A PKA [30].

The DPA is a standard parameter in the determination of radiation damage in materials. Is the number of Frenkel pairs produced by a PKA at the end of a displacement cascade. The calculation of the rate of DPA per second is performed by following formula [31]:

$$DPA = \int_0^\infty \emptyset(E)\sigma_{dpa}(E)dE$$

where, $\emptyset(E)$ is the differential neutron flux density [n/cm^2/s/MeV], and $\sigma_{dpa}(E)$ is the cross-section of the DPA [cm^2].

In order to conduct comparative calculations for damage induced by neutrons and ions, it is necessary to calculate the neutron flux and neutron fluence parameters. The neutron flux (ϕ) is defined as a number of neutrons crossing the area in all directions per unit of time (neutrons/cm^2/s). It is calculated by multiplying the neutron density (n) by the neutron velocity (v) and can be presented as a scalar form.

$$\phi(\vec{r}, E, t) = \int_{4\pi} v\, n\left(\vec{r}, E, t, \vec{\Omega}\right) d\vec{\Omega} \quad (1)$$

Knowing the neutron flux it is possible to calculate the neutron fluence. Neutron fluence is the time integral of the neutron flux, expressed as the number of neutrons per cm^2.

$$\phi = \int \varphi(t) dt \quad (2)$$

With the use of the DPA parameter, it is possible to recalculate the neutron fluence to the ion fluence with which the ion irradiation can be performed.

The ion irradiation is a good reflection for neutron damage occurrence because ion-induced damage also causes atomic displacements from the crystal lattice. Ion irradiation with the use of self (He^+ ions) or heavy ion irradiation can produce damage in analyzed structure in a much shorter time, within hours/days instead of months or years, in comparison to neutron irradiation. In addition, using the ion irradiation method is cost and time effective, and the irradiated specimens are not activated (radioactive) after the ion irradiation process.

2.2. NUCLEAR REACTORS

The most important component of the nuclear reactor is the core, where the radioactive fuel is placed, a coolant, and a moderator. Nuclear fuel commonly takes the form of cylindrical pellets which are packed in long metal tubes to form fuel rods. The fuel rods are grouped into fuel assemblies that are used to build up the core. Fuel is encapsulated in a cladding material with low absorption of neutrons, like zircaloy or graphite. The main role of this material is to prevent any radioactive materials to escape into the coolant and contaminate it. Only neutrons can go through the cladding during normal operating conditions. The speed of the nuclear reaction is controlled by control rods, which serve to absorb neutrons, slowing down the fission reaction. Control rods are composed of neutron-absorbing material including silver, boron, iridium, or cadmium. The position of these control rods in the reactor core determines the rate of the fission chain reaction. After loading the fuel inside the reactor core the controlled fission reaction can occur, which steadily generates heat, after which the heat is utilized via the Rankine cycle (or other power cycles). The released heat energy is used to heat water and produce high-pressure steam, which turns a turbine connected to a generator, that allowed to generate

electricity. The coolant flowing through the channels within the fuel assemblies removes the heat generated by nuclear fission. Typically, the coolant is a liquid (water) or gas (helium), the other coolants include air, carbon dioxide, liquid sodium, and a sodium-potassium alloy. In reactors using light water (H_2O), or heavy water (D_2O), the coolant also serves as the moderator. The moderator is a material that decelerates the scattered neutrons generated by the fission reaction and cools the fuel cladding. The typical moderators are water and graphite, but also deuterium and beryllium.

Presently, we can distinguish five generations of nuclear reactors (Fig. 2. 2). The first generation (Generation I) of reactors is called breeder reactors, characterized by the process of converting fertile materials into fissionable fuels known as the breeding process. The breeder reactors used fertile materials as fuel, such as natural uranium ^{238}U or thorium ^{232}Th. The fertile material transforms into fissionable fuel due to the bombardment with the neutrons, e.g. the ^{238}U can be made fissile in about 2½ days. The characteristic feature of this type of reactor is that about ~2.7 neutrons are generated for one absorbed neutron to produce fission, while 1.7 neutrons produce fuel breeding [32]. Another reactor classified as first generation is an early prototype of Boiling Water Reactors (BWR), nevertheless, none of the first generation reactors is in use to this day. The second generation (Generation II) includes mainly the BWR, AGR and Pressurized Water Reactor (PWR), and refers to the class of commercial reactors. The Generation III and Gen III+ nuclear reactors are based on Generation II reactor design, with improved fuel technology, increased efficiency, modularity, and safety.

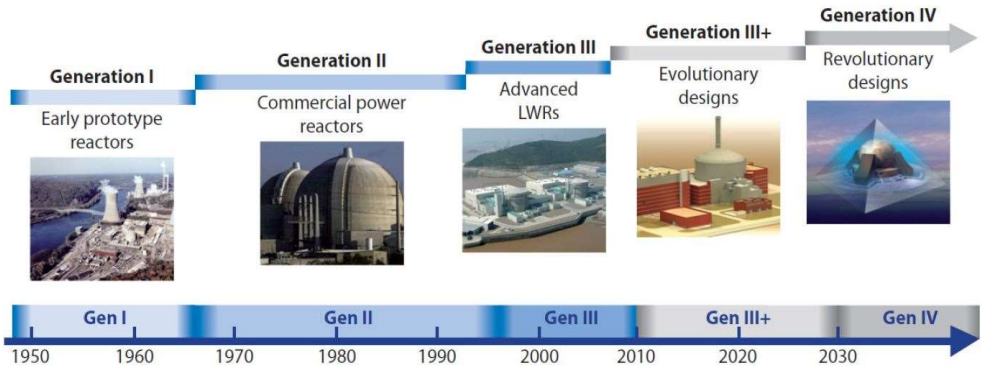

FIG. 2. 2 GENERATIONS OF NUCLEAR POWER: TIME RANGES CORRESPOND TO THE DESIGN AND THE FIRST DEPLOYMENTS OF DIFFERENT GENERATIONS OF REACTORS [33].

Generation IV (Gen-IV) is a common name for ongoing research projects of future-oriented nuclear reactor concepts with hydrogen production capabilities. The basic features to be met by these reactors are safety, reliability, efficiency, sustainability, proliferation resistance, and low production costs. Six reactor concepts were selected by the Generation IV International Forum (GIF). The GIF was established as an initiative of the US Department of Energy (DOE) to lead

international cooperation on Research and Development (R&D) of the next generation of nuclear reactors. For further development and commercial implementation we can distinguish Sodium-Cooled Fast Reactor (SFR), Lead-Cooled Fast Reactor (LFR), Molten Salt Reactor (MSR), Gas-Cooled Fast Reactor (GFR), Supercritical-Water-Cooled Reactor (SCWR), and the Very-High-Temperature-Reactor (VHTR) – presented in Fig. 2. 3. All of these rectors based on the different technology, including the usage of the thermal or fast neutrons, open or closed fuel cycle, and the source of coolants such as helium, water or sodium, lead/bismuth, and salts of fluorine. Nevertheless, all of the reactor types operate at higher temperatures than the LWRs reactors [33][34][35][36][37][38].

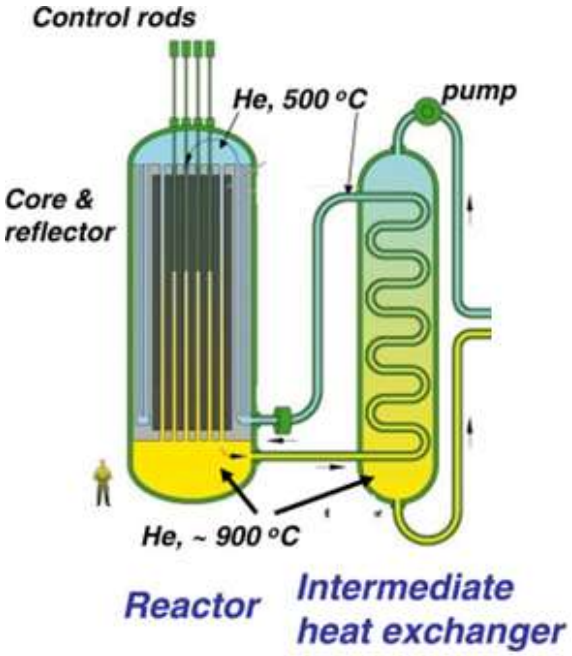

Fig. 2. 3 The VHTR – a helium-cooled, graphite-moderated thermal-neutron reactor [36].

Both, the VHTR and HTGR concepts provide several inherent safety advantages due to the specific design features, physical laws, and due to the reactor material behavior, such as low-power density in the reactor core, a large heat capacity of the core, and an inert coolant (that can mitigate severe accidental consequences during loss-of-coolant accident scenarios). Due to these specific features and the excellent performance of the fuel, these reactors have been recognized as an inherently safe type. The safety is provided by several barriers that prevent fission product release into the environment, like the TRISO-particle coatings, graphite matrix, the reactor pressure boundary, the containment vessel, and the reactor building [23][39][40][41].

2.2.1. HIGH TEMPERATURE GAS-COOLED REACTOR

The development of the HTGRs starts in 1960 with the United Kingdom demonstration (prismatic) reactor named Dragon [25][42][43], and the experimental reactor for electricity generation, the pebble-bed fuel type – Arbeitsgemeinschaft Versuchs Reaktor (AVR)- of the German production [23][25][42][44]. At the same time, the pilot prismatic core designs were developed in the United States within the Peach Bottom project [25][42], and later, the demonstration Fort St. Vrain reactor [25][45][46][47][48][49][50]. Since 1980, the R&D of the HTGRs has significantly expanded, resulting in the current projects, such as the China HTR-10 [25][42][51] pebble-bed type test reactor, and the demonstration pebble-bed HTR-PM [25][52][53] plant, and the Japan prismatic core block High Temperature engineering Test Reactor (HTTR) [25][42]. At the same time, many scientific projects on HTGR technology improvement are currently running worldwide [43][54][55][56][57].

HTGR uses a TRISO fuel in the reactor core with a graphite moderator and helium as coolant [33][42][58]. The HTGRs operate in an open fuel cycle with single-cycle uranium fuel, with the use of the thermal neutrons, assuming a reactor outlet temperature between 700 - 950°C even up to 1000 °C (VHTR) [20][23][33][59][60][61]. Such a high temperature allows the use of process heat to drive a thermochemical cycle or use generated energy for hydrogen production (Fig. 2. 3). The hydrogen production might be due to the electrolyzing process of the alkaline water to produce hydrogen or by converting hydrocarbons into hydrogen [20][34][37][39][62].

As mentioned above, two types of HTGR cores were designed, the prismatic core design and the pebble-bed design [20][36][58], presented in Fig. 2. 4. In both cases the TRISO-coated particles are covered with graphite matrix to moderate neutrons, and because graphite can keep the radioactive materials up to the 1600°C [20][39][40][43][54][59]. In the pebble-bed type, around 9000-18000 [23][59][63] TRISO-particles are immersed in the graphite matrix, forming the sphere of the shape and the size of the tennis ball. In the case of the prismatic design, around 1500-4000 [43][64][65] TRISO-particles are covered with graphite forming cylindrical compacts - pellets. The overcoating process of the TRISO-particles was broadly explained in Ref. [23][59][66].

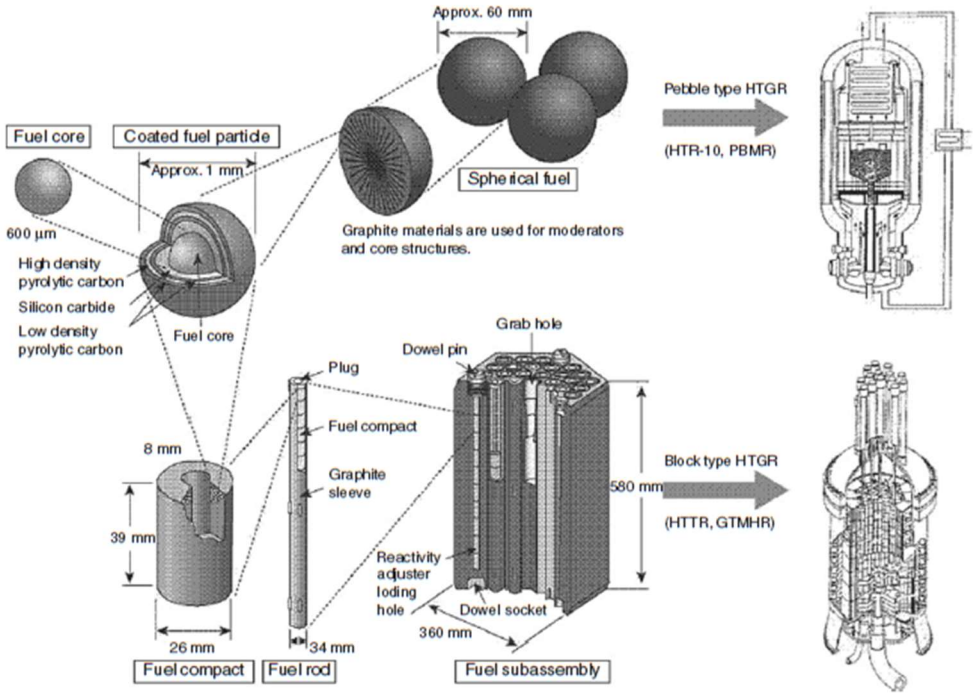

FIG. 2. 4 HTGRS AND FUEL FORMS [39].

The pebble-bed concept is based on the spherical fuel elements with a 60 mm diameter piled in a reactor vessel, which consists of an inner 50 mm diameter fuel zone surrounded by a 5 mm thick fuel-free shell of the graphitized fuel matrix material [23][25][43]. The prismatic core design includes hexagonal shape blocks circa 800 mm high and circa 360 mm across flats, fabricated from graphite, in which the separate fuel and coolant holes are drilled. The cylindrical fuel compacts circa 12.5 mm in diameter and circa 50 mm long (containing the over-coated fuel particle), are stacked in the fuel channels [20][23][43].

It is also worth noting that although modern HTGRs guarantee reactor operation without damage to the TRISO covering layers, the thermal properties of compact/sphere graphite matrix are only known up to 1000°C. This presents a licensing risk since an HTGR proposal that presents a lack of 1600°C data could be quickly dismissed. For that reason, new measurements and computer simulations are urgently needed to clarify these issues. Therefore, it is very important to carry out comprehensive research on this technology and prepare the future workforce for the responsible operation of HTGRs.

3. TRISO-COATED PARTICLE

TRISO-particle fuel is a type of nuclear fuel commonly used in HTGRs since the 1960s when these reactors were developed and constructed. The precursors in coating fuel particles were the United Kingdom Atomic Energy Authority (UKAEA) & Battelle, and R. Huddle who in 1957 proposed this solution for emerging nuclear systems [20][23][60][67]. Since then, experiments on various forms of coated-particle fuel with a spherical kernel of fissile or fertile material, have been developed and performed. The earliest version of coated-particles involved fuel kernels coated with only a single pyrolytic carbon layer intended to protect the kernel during fabrication, which was performed during the initial stages of the British Dragon Project. Until the 1980s, two types of fuel constructions were used on a large scale, the two layers Bi-structural (BISO) fuel [20][23][43], and the TRISO fuel. The BISO fuel consisted of a porous, low-density Buffer layer, and a high density isotropic pyrocarbon layer. The evolution of the particle design is depicted in Fig. 3. 1.

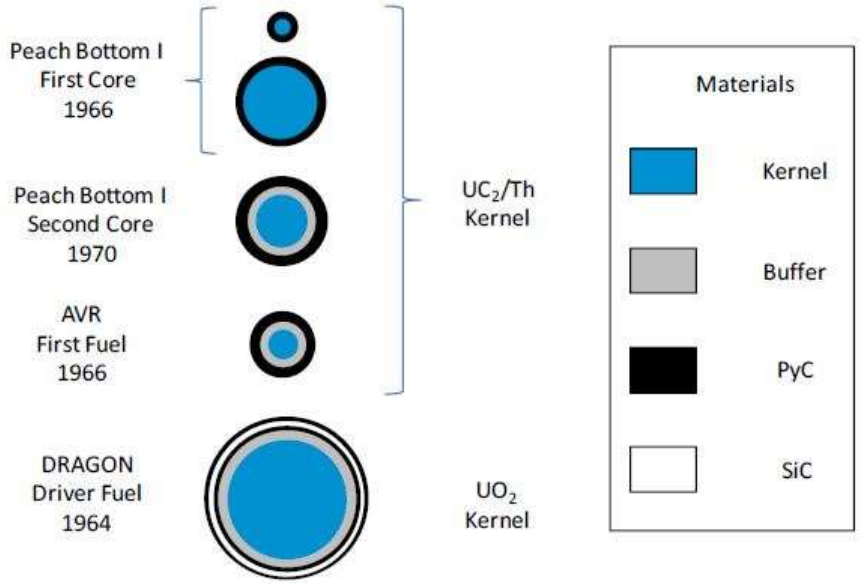

FIG. 3. 1 EARLY COATED –PARTICLE DESIGN [43].

A TRISO-coated particle is spherical and consists of a dense fuel kernel of heavy metal oxide, carbide, or a mixture of both. HTGR fuel is typically based on enriched uranium (UO_2 or UCO) but also thorium or mixed oxide fuel (MOX)-based TRISO fuel is possible. The MOX fuel use depleted uranium enriched with recycled plutonium [20][23][59][61]. The uranium carbon oxide (UCO) fuel kernel limited the production of the CO and CO_2 gases [68][69]. The fuel kernel is surrounded by four coating layers, a low-density porous pyrocarbon Buffer layer, a dense and highly isotropic inner pyrocarbon layer (IPyC), a silicon carbide (SiC) layer, and an outer dense pyrocarbon layer (OPyC) [20][36][43][57]. The typical TRISO-coated particles

have an overall diameter in the range of 500 to 1000 µm [20][57]. Fig. 3. 2 shows the cross-section of the typical TRISO-coated particle fuel, with information about layer types and their thicknesses, which could be observed on that particle [23][43][70].

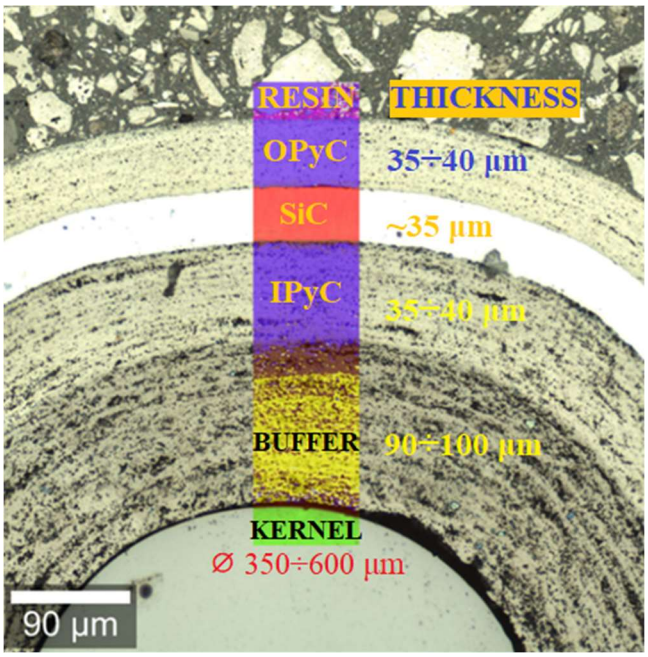

FIG. 3. 2 TRISO FUEL CROSS-SECTION WITH THE FOLLOWING DIMENSIONS OF EACH LAYER FOR TYPICAL TRISO-COATED PARTICLE FUEL [71].

The assumptions for the design and fabrication of the coated fuel were to remain intact and retain radionuclides over the range of conditions that could be encountered in normal operation and accident conditions [43][59][69]. The BISO fuel was able to contain gaseous fission products, but at elevated temperatures, the diffusive release of certain metallic fission products (cesium, strontium, and silver) occurred from the BISO coatings [23]. Due to that, currently, all modern HTGRs use TRISO-coated particles. The experiences in manufacturing the TRISO coated-particle fuel have demonstrated the feasibility of producing large quantities of particles with a simultaneously low defect level, that approach the failure probability of 10^{-5} for the PyC layers [20][23][43][72][73][74] and 10^{-6} for the SiC layer [68].

These manufactured particles must be able to accommodate the following effects [43][74]:

- high-energy neutron-induced changes in material microstructure (reduction of the SiC layer strength, expansion, or anisotropic shrinkage in the PyC layers);
- chemical reaction with particle layers and redistribution of fission products (FP) within the particle (migration of the kernel, chemical attack on the SiC layer);
- fission-induced changes in the kernel (FP isotopes production, kernel swelling due to solid/gaseous FP, lattice dislocation by FP recoil);

- buildup of pressure within the particle (release of noble gas FP from the kernel).

The development of research on coated-particle fuel has been carried out in many countries, including Germany, France, Russia, the USA, South Africa, Japan, South Korea, and China. Based on numerous studies, it was proved that the TRISO-type fuel particles were able to meet the quality and efficiency of fuel required in modern HTGRs [20][23][43].

3.1. TRISO COATING LAYERS

The coating layers of the TRISO fuel particle inhibit the release and migration of FP from the fuel particle, so they serve as a functional containment for the fuel kernel and act as a primary barrier to prevent the release of FP. During irradiation and in case of hypothetical accidents, they function as a pre-stressed pressure vessel, thereby containing the inner pressure which builds up due to the generation of fission gases and release of oxygen from the fuel [20][23][36][43].

Functions of the individual layers are shown in the Tab.3. 1 [20][43][59][69].

TAB.3. 1 FUNCTIONS OF THE TRISO LAYERS

TRISO	*Functions*
Kernel	• serves as a barrier to radionuclide release; • serves as a substrate for the deposition of the PyC layers.
Buffer (low-density porous PyC)	• provides a space for the accumulation of gaseous FP released from the kernel; • serves as a protective layer for the subsequent covering of IPyC and SiC layers, by absorbing the kinetic energy of fission fragments ejected from the kernel surface; • serves as a mechanical separation between the kernel and the coating layers to accommodate kernel swelling, by reducing the buildup of stress in the outer coating layers during irradiation.

IPyC (high-density isotropic PyC)	• provides a smooth substrate for the SiC layer deposition; • serves as a barrier against the pressure exerted by gaseous FP and reaction products (CO, CO_2) created in the kernel and Buffer layer; • provides a deposition surface for the SiC layer and acts as a seal layer to protect the kernel from corrosive gases (HCl, Cl_2) released during the SiC coating process; • it shrinks during the neutron irradiation process (Fig.3.4) –helping to reduce tensile stresses in the SiC layer.
SiC	• serves as the metallic FP diffusion barrier; • has sufficient strength to withstand the internal pressure produced during irradiation, which provides a high level of assurance the SiC layer will remain intact during reactor operation.
OPyC	• serves as the last FP barrier; • serves as a bonding surface for graphite matrix coating process for sphere/compact molding; • protects the SiC layer from mechanical damage during particle transfer; • it shrinks during the neutron irradiation process (Fig.3.4) – helping to reduce tensile stresses in the SiC layer.

The materials of the cover layers are referred to pyrolytic because they are formed by pyrolysis (thermochemical decomposition) of organic material caused by the application of heat. Pyrolytic carbon is a carbon-based material deposited from gaseous hydrocarbon compounds on suitable underlying substrates, which can appear with different microstructures, such as isotropic, laminar, columnar, or granular [54][59]. Detailed explanation of the TRISO coating technology is described in Ref. [20][23][43][59][75].

The experiments performed on the TRISO-particles with the zirconium carbide (ZrC) layer (instead of the SiC layer), proved that the use of that layer enables an increase in the power density and core power with the same coolant outlet temperature. At the same time, the ZrC layer exhibits greater resistance to the chemical attack by the FP, and have shown no corrosion by palladium, and has a good retention capability of cesium. Nevertheless, due to the thermomechanical material property degradation under accident conditions, and the difficulty

in the layer fabrication, caused the idea of replacing the SiC layer with a ZrC layer was suspended [20][33][60].

3.2. TRISO FUEL FAILURES

During irradiation in the reactor core, partial or complete failure of the TRISO-particle coating layers may occur [20][68]. A large knowledge and modeling base exists on the behavior of TRISO-coated particles under irradiation as well as under accident conditions, and numerous benchmarking exercises comparing experimental results and calculations on TRISO failures show that failure mechanisms are rather well understood [20][43][68].

For the purpose of performed experiments, the TRISO fuel failure mechanisms have been divided into three categories: damage location, damage factor, and cause of the damage.

- *Criterion of damage location*

A TRISO fuel failure can be considered in terms of damage location, distinguishing as an external and internal area of the particle. As an external area, the OPyC layer is contemplated. Damage to this structure usually occurs as a result of some physical force and is created mainly during the production process of TRISO fuel (bad quality of the layer microporosity and anisotropy). The damage to the OPyC layer can be observed by one of the tools for imaging a fuel particle, e.g. optical microscopy. As an internal area considered damages placed in the kernel, Buffer, IPyC, and SiC layers. The damages are observed on the surface of each layer or at the interface of these layers. These failures are mainly caused by mechanical or chemical factors.

- *Criterion of damage factor*

There are two types of factors causing damage in the TRISO fuel particle, mechanical and chemical. Mechanical failures can appear in each of the structural layers, like in a Buffer, IPyC, SiC, and OPyC layer. They arise as a result of the deformation of the layers due to their mutual interactions. A layer may be damaged by the initiation and propagation of a crack or by stress or friction which exceeds the strength criterion of the material. The chemical kind of damage is caused by the interaction of chemical elements and by the presence of FP that accumulate inside the particle during irradiation. The phenomena accompanying this type of failure are corrosion, decomposition, and weakening of layers.

- *Criterion due to the cause of the damage*

The TRISO fuel damage is caused by mechanical and chemical causes, presented in Fig. 3. 3. The chemical damage includes:

- kernel migration – is a movement of the kernel towards the TRISO-particle layers. This phenomenon is called the "amoeba effect", which may be caused by extreme operating conditions and asymmetrical kernel production during manufacturing (aspherical particle); it can lead to complete failure of the coating layers. Kernel migration depends on power density, temperature and temperature gradient across the fuel, and the thicknesses of the Buffer, and IPyC layers. The amoeba effect is likely happening for the UO_2 kernel then for UCO kernel [20][36][43][68][76].
- chemical attack – during irradiation the thermo-chemical conditions are not conducive to the formation of stable oxides of noble metals like palladium, rhodium, ruthenium, and silver [57][77][78]. The fission products can be transported from the kernel to the inner layers, where they interact and potentially can fail the SiC layer. These noble metals can migrate out of the kernel, for example, palladium can penetrate the SiC layer causing the thinning of the layer, which in the consequence can lead to particle failure. The migration of the FP is a function of time at temperature, temperature gradient, and burn-up [20]. Measurements of the FP release (i.e. silver, cesium, strontium, and krypton) from the TRISO-particles, performed in the experiments and simulations, are described in detail in Ref. [64][70][79][80].

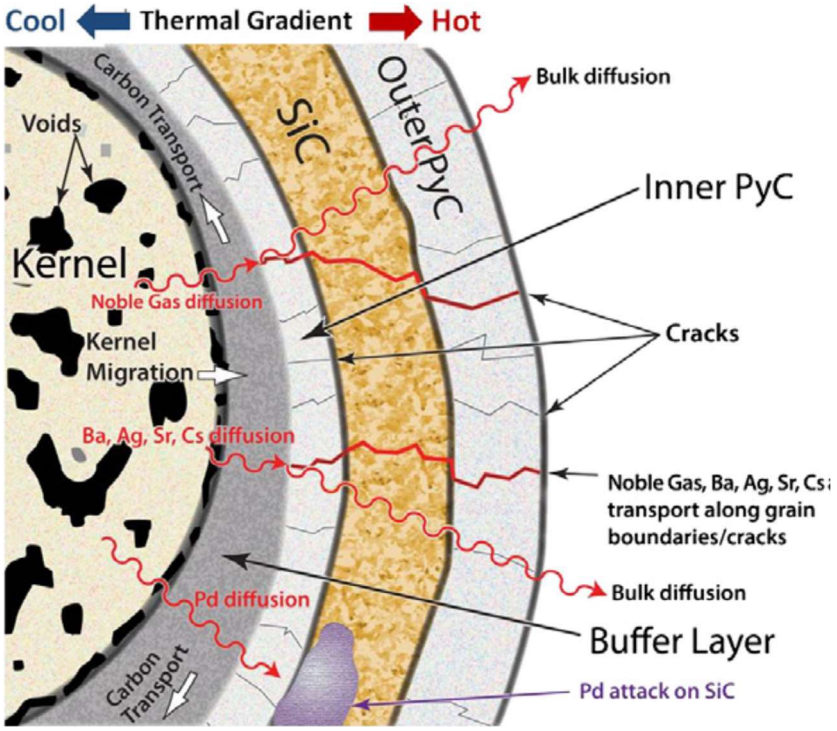

FIG. 3. 3 SCHEMATIC OF PROCESSES IN A TRISO-PARTICLE THAT ARE OBSERVED DURING HIGH BURN-UP [81][82].

Mechanical damage can be caused by overpressure [20]. During irradiation of TRISO-particle, the FP are released from the particle kernel into the Buffer, and then the PyC layers might shrink and creep. The PyC layers shrink in the radial and tangential directions during neutron irradiation. Shrinkage produces tensile stresses in the PyC layers, which might cause crack formation in that layers. Then the radial crack in the IPyC layer creates tensile stress in the SiC layer, leading to particle failure. This phenomenon (Fig. 3. 4) causes an increase in the internal gas pressure. When the Buffer thickness decrease, the volume available to store fission gas also decreases. As a result, high pressure and higher stress in the SiC layer have been created. The layer which can bear most of the internal pressure forces is the SiC layer because it has a much higher elastic modulus than the PyC layers. The SiC layer will remain intact, when compression or tensile stress in the layer, will not exceed its strength [43][74].

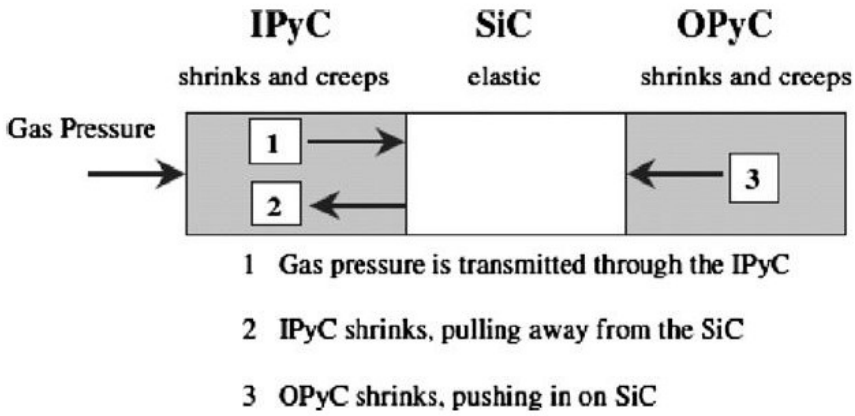

FIG. 3. 4 BEHAVIOR OF COATING LAYERS IN A FUEL PARTICLE [57][83].

The most common partial or complete failure mechanisms of TRISO-particles under irradiation are described below, and are shown in Fig. 3. 5 [43]:

- irradiation-induced failure of the OPyC layer, the IPyC layer, and potential SiC cracking;
- failure of the SiC layer, caused by: heavy metal (HM) dispersion in the Buffer and IPyC layers, FP or CO interactions with the SiC layer;
- failure of the SiC layer as a result of thermal decomposition, and kernel migrations;
- pressure vessel failure of the: intact particles (without manufacturing defects) or particles with defective or missing layers.

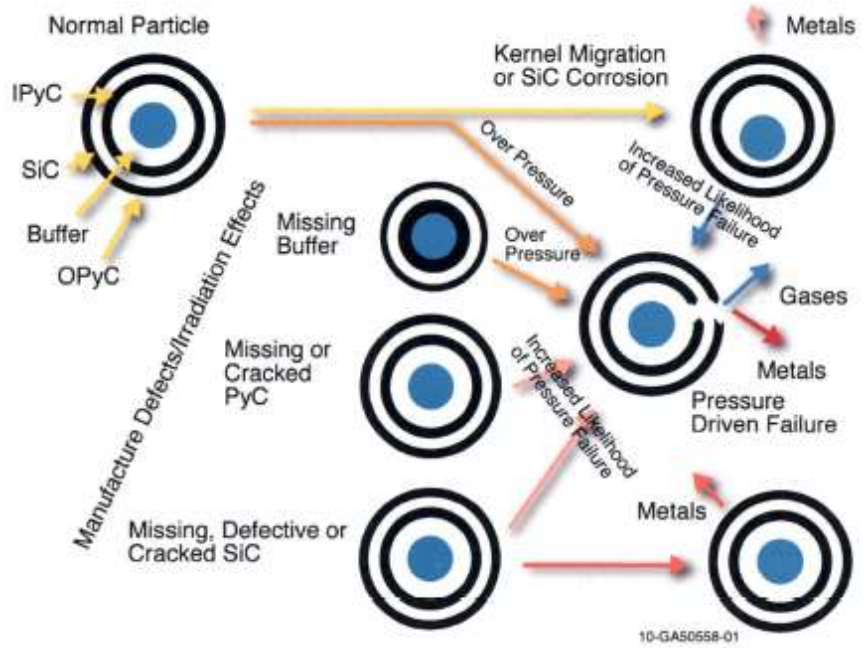

FIG. 3. 5 TRISO-PARTICLE FAILURE MECHANISMS [43].

We can distinguish two cases of SiC failure, that enables the layer to retain the FP: the diffusive release through intact SiC, and the SiC degradation resulting in permeability to the FP. A detailed explanation of the SiC layer-induced failures is described in Ref. [20][43]. The mechanical failure probability [74]:

- increased as the thickness of the SiC layer decreased because there is less structural material to retain the fission gas pressure;
- increased as the thickness of the IPyC layer increased because thicker PyC experiences higher stress levels in early irradiation. This results in a higher IPyC cracking probability causing localized stress concentrations in the SiC layer.

Due to the irradiation-induced shrinkage, the debonding at the Buffer-IPyC [84][85][86], and IPyC-SiC [20][43][57][68][75] interface is observed. In the case of the IPyC-SiC interface, the debonding occurs based on the weak bonding between both of these layers, and the generation of the tensile stresses by IPyC shrinkage.

The subject of this dissertation thesis focuses on the two failure mechanisms of the TRISO-particles, distinguished as the irradiation-induced PyC failures, and the Buffer-IPyC interface partial debonding. The reasons for the failure creation are the influence of the fast fluence, and temperature, which might cause the dimensional changes in the PyC layers (PyC: density, thickness, anisotropy, and strength), and the consequence changed the nature of the layer interface. Counteracting the formation of such failures is the proper application of coating

layers. Being aware of the occurring damage mechanisms in TRISO-particles, this work focuses on verifying the quality of the produced fuel at the front-end stage.

3.3. TRISO QUALITY CONTROL

The TRISO-coated particles after fuel fabrication must pass a QC test, to determine if the fuel meets the standards e.g. coating defects rates. The TRISO-coated particle fabrication process starts from the fuel kernel obtained by the sol-gel technique [76][87][88]. The kernels are first sorted to choose the most spherical ones, then are overcoated with the pyrolytic carbon, and silicon carbide layers.

The qualification of the TRISO-coated particle fuel involves the verification of the TRISO-particle fuel failures rates in three different stages: at the front-end (fabrication), during irradiation in the reactor core, and in the frame of post-irradiation examinations and post-irradiation accident testing. The front-end stage is the initial analysis of the produced samples before they are placed in the reactor core. The following stage is the observation of damage that occurs in TRISO samples as a result of irradiation of these samples in the reactor core.

The front-end stage focused only on the TRISO-particles, and include methods to verify the size, integrity, and roundness of the fuel particles. The over-sized, under-sized, and odd-shaped particles are removed and collected for recycling. The next stage of verification is devoted to the compacts/pebbles, where the particle distribution is measured. Then there is the post-irradiation examination to determine how many particles have failed SiC layers and/or complete TRISO failures (failure of all three TRISO layers, IPyC, SiC, and OPyC). The QC for TRISO fuel includes some parameters on kernel, coatings, compacts, and defect population that may impact performance. The inspection techniques include density, sphericity measurements, and destructive testing [60]. Presented parameters (Tab.3. 2) are analyzed using various research methods, both after the fuel particle fabrication and after irradiation of the sample in the reactor core, to check the failure rate in the TRISO-particle. The detailed explanation of the quality assurance and quality control methods are broadly explained in the IAEA report [76], and by W.W. Delle et.al, and H.J. Hantke et.al. [20][59][89][90].

TAB.3. 2 FUEL SPECIFICATIONS [89][91]

Fuel Kernel

Heavy metal loading	Transfer of kernels into a stoichiometrically well-defined state and chemical analysis
O/M ratio	Potential controlled coulometry
Isotope composition	Mass spectrometry concerning to ^{234}U, ^{235}U, ^{238}U
Carbon content	Oxidation of kernels, chemical analysis of CO_2
Oxygen content (UCO)	Hot extraction of oxygen, transfer into CO and chemical analysis of CO, infrared spectrometry
Diameter	Optical imaging with particle size analyzer, X-ray micro-radiography
Sphericity	Counting a fraction of odd-shaped particles, Multiple measurements of maximum and minimum diameter, Micro-radiography, stereo-microscope
Density	Optical particle size analyzer to measure mean diameter; Air pycnometer to measure the volume
Structure	Measurement of reflection on defined lattice planes, X-ray with Debye-Scherrer goniometer
Weight	Weight of counted number of kernels and determine the mean weight
Impurities	Spectral photometry, Atom absorption spectrometry

Coated Fuel Particle

Diameter	Optical particle size analyzer
Layer thickness	X-ray projection micro-radiography (only OPyC and SiC), X-ray contact micro-radiography, Microscopic analysis of ceramographic sections, Optical particle size analyzer
Density	Weight of counted number of particles and determine the mean weight
Density of highly dense layers	Liquid density gradient column with calibration bodies Gas pycnometer
Optical anisotropy factor OAF (in air) or OPTAF (in oil), Bacon anisotropy factor (BAF)	Ceramographic sections exposed to polarized light, OPTAF is the ratio of reflected light intensity vertically to deposition direction over reflected light intensity in deposition direction; Correlation between OPTAF and BAF
Growth features, size, and distribution	Etching of ceramographic sections by wet oxidation, plasma oxidation, or ion bombardment, Scanning electron microscopy (SEM), Transmission electron microscopy (TEM)
Heavy metal content	Grinding of particles and transfer into distinct compounds of U by oxidation, quantitative chemical analysis of U
Surface contamination	Leaching of particles with HNO_3, quantitative chemical analysis of U
Defective SiC layers	Burn-Leach method
Heavy metal migration	Micro-radiography, visual inspection of Buffer layer
Tightness of IPyC	Micro-radiography, visual inspection of Buffer and IPyC layers after leaching with HNO_3

Micro-porosity	Determination of fractions of layer mosaic components in PyC by X-ray small-angle diffraction
Pore structure	Quantitative image analysis and determination of pore size distribution
Ultimate tensile strength of SiC and PyC	Determination of fracture load by crushing between sapphire plates, Hemispherical bursting, Ring compression test
Micro-hardness	Vickers or Brinell hardness
Young's modulus: PyC, SiC	Crushing between sapphire plates and recording stress-strain curve

The anisotropy parameter, defined by the Bacon Anisotropy Factor (BAF), is measured in the PyC layers. BAF is determined by measuring the change of polarized light reflected on a polished cross-section, and in the PyC layers is equal to 1.035 [69]. This parameter must be dense and isotropic to be able to sustain the neutron irradiation and to avoid the occurrence of shrinkage or creep in the PyC layers.

The experimental and simulations tests performed in normal and accident conditions are checking if the TRISO-particles may robust under accident conditions in temperatures up to 1600, 1700, and 1800 °C [20][23][33][43][60][70]. The temperature of 1800°C is the temperature at which the degradation performance of the SiC layer is expected to begin.

4. TRISO DIAGNOSTIC TOOLS

The most common diagnostic methods for the TRISO-coated particle include [88]:

- Raman spectroscopy;
- Scanning Electron Microscopy (SEM);
- Transmission Electron Microscopy (TEM);
- X-Ray diffraction (XRD);
- X-Ray Tomography;
- Electron Probe Micro Analyzer (EPMA);
- Dual-beam focused ion beam (FIB);
- Knudsen Cell Effusion Mass Spectrometry;
- Hardness measurements (nano- & micro indentation).

The Raman spectroscopy method was selected as the main screening method for monitoring the changes in the Raman spectra of the "virgin" and ion-irradiated TRISO fuel particles. In addition, SEM was used to visualize the structural changes taking place in the analyzed layers. The scientific process is completed as follows:

- Prepare samples for examination: polishing methods, Confocal Laser Scanning Microscopy.
- Calculate ion irradiation energy and fluences: Stopping and Range of Ions in Matter and the Transport and Range of Ions in Matter codes.
- Sample implanting: ion implanter.
- Sample measurement before and after irradiation: Raman spectroscopy, SEM.

4.1. EXPERIMENTAL METHODS

4.1.1. MECHANICAL POLISHING METHOD

Mechanical polishing is a standard method of TRISO sample preparation [92][93][94]. The polishing procedure takes into account several stages at which different abrasives like diamond paste [27][95], sand paper [96][97], etc. can be used. In the case of the TRISO samples used in this dissertation, the mechanical polishing procedure was performed in the three steps [71]:

- 1st step - immersing the TRISO samples (fife TRISO-particles) in thermosetting resin;
- 2nd step - polishing with an abrasive paper, starting with a grit size of 300 and finishing with a grit size of 2000;

- 3rd step - polishing on the 3 µm and 1 µm diamond suspension, with final polishing using colloidal silica suspension.

The mechanical polishing process was performed with the use of the Struers Tegramin device [98]. Fig. 4. 1 presents fife TRISO-particles which were polished by the mechanical method.

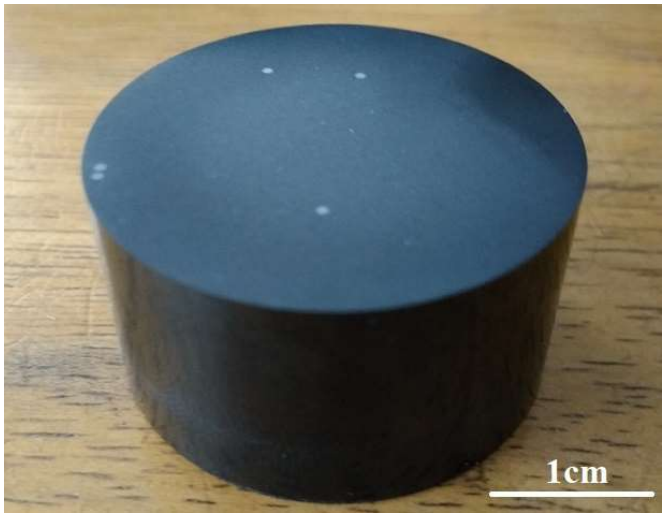

FIG. 4. 1 FIFE P-TRISO POLISHED SAMPLES.

4.1.2. ION POLISHING METHOD

The ion polishing method is non-invasive method of the TRISO sample preparation. The ion polishing process on the single TRISO sample was performed in the three steps [71]:

- 1st step - precisely positioning the TRISO sample on the aluminum holder - Fig.4. 2 (particle is fixed by the application of several drops of silver conducting glue);
- 2nd step – attaching the holder to the mechanical positioning system (allow for precise alignment of the cutting mask and sample position with respect to the ion beam);
- 3rd step - ion milling using Ar^+ ions accelerated in the potential of 6 keV - Fig.4. 3.

The ion polishing process was performed with the use of the Hitachi IM4000Plus system [99].

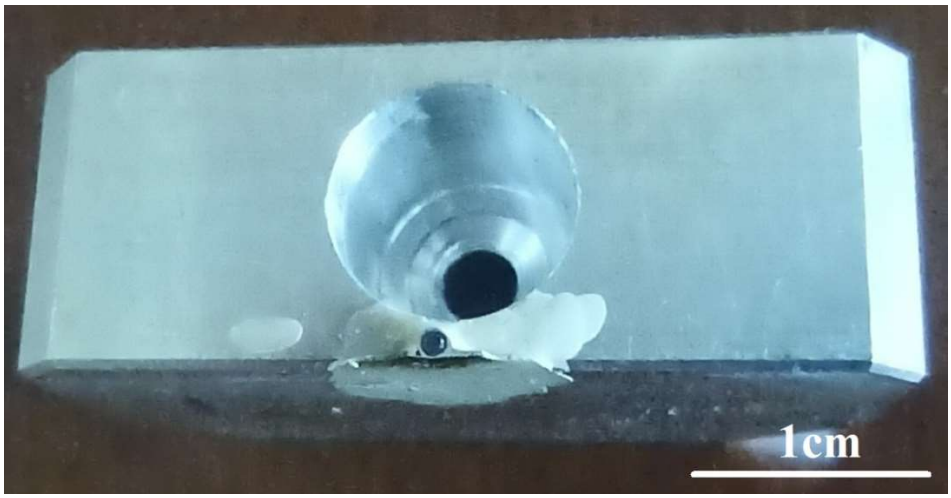

FIG.4. 2 TRISO ON THE METAL HOLDER.

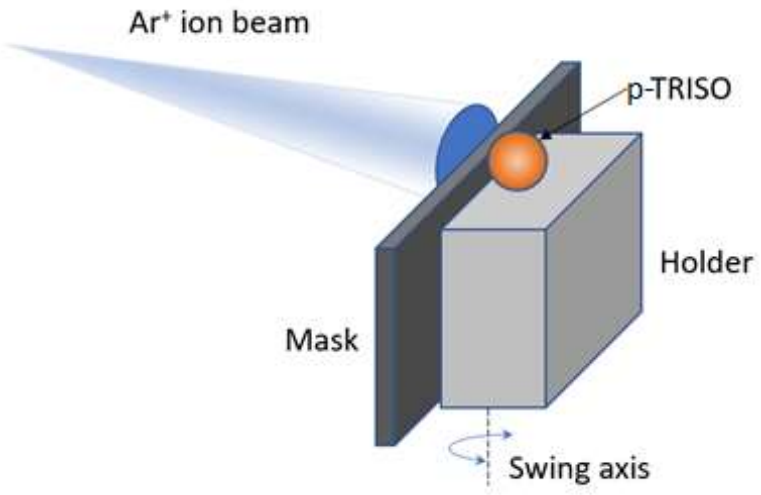

FIG.4. 3 THE ION POLISHING METHOD FOR TRISO-PARTICLE [71].

4.1.3. SCANNING ELECTRON MICROSCOPY

The Scanning Electron Microscope is a measurement device used to characterize the surface of the sample. The SEM tool uses electrons in the beam, which interact with the sample creating various signals, which get information about the composition and surface topography of the analyzed material [100]. When the primary electron beam reaches the sample surface, some of the electrons travel a certain distance into the sample. Secondary electrons are created by inelastic collisions, where some of the primary electrons knock out the electrons from energy levels of atoms in the sample. The secondary electrons have such low energy that they can only be detected if they are produced from the surface of the sample. They are useful for topographic information and high-resolution studies. In this experiment, the secondary electrons were used to study the surfaces of the PyC layers [101].

Observation of the TRISO cross-sections were performed using the SEM FEI Versa 3D device [102]. In order to alleviate the charging effects of the non-conducting ZrO_2 kernel, an accelerating voltage of 5 kV was used during the observations [71].

4.1.4. CONFOCAL LASER SCANNING MICROSCOPY

The confocal laser scanning microscope is an advanced variant of the fluorescence microscope, in which the source of a light is a laser. This equipment is dedicated to analyze optical cross-sections in continuous time located on the surface, or in the depth of a preparation for nanometer-level surface imaging, the 3D imaging and for the roughness measurement [103][104].

Measurements on TRISO samples were carried out by the Olympus Lext OLS4100 microscope [105]. CLSM device measures the surface roughness of micro geometries at high resolution, and it is capable of recognizing the peaks of reflected light intensities originating from multiple layers. The measurements enable the analysis of multiple layers, measuring the shape and roughness of each layer as well as the thickness of the surface layer can be measured.

4.1.5. RAMAN SPECTROSCOPY

The Raman micro-spectroscope is a tool used for recording the Raman scattering spectra, which shows the chemical components characteristic for the analyzed material. The Raman scattering spectrum is excited in the visible, near-infrared, or ultraviolet region, and is an oscillation-rotational spectrum [106]. Each spectrum provides information about the oscillational and rotational energy levels of the molecules. The molecule is characterized by the number of vibrations, their frequency, and amplitude. Raman scattering spectrum is presented in the form of a band with characteristic contours in the form of the bell curve, which is a feature of the interaction of substances with radiation. The bell curve band is dependent on the intensity of the amplitude (I) of absorption, emission, or scattering on the frequency (v) of radiation interacting with the analyzed system [16][107][108]. With the Raman spectrum, is possible to observe the symmetrical vibrations of the molecule, vibrations of the carbon skeleton of the molecule, and vibrations between atoms with double and triple bonds [109][110].

Raman spectroscopy is one of the methods to show the changes in the TRISO-particle fuel structure induced by irradiation [27]. With this method it is possible to observe, among others, damage appearing in the TRISO-particle, as well as determine the concentration of carbon in each layer. Obtained results provide a fingerprint to identify the chemical component, analyze them, and to better understand their structures. By measuring the particles before and after irradiation, it is possible to compare the changes that have occurred as a result of irradiation in the reactor. In this dissertation, Raman spectroscopy was selected as a research method for monitoring the changes in spectra, for a “virgin” and ion-irradiated samples of TRISO-particles.

Raman spectroscopy can be implemented to determine the structure of nuclear fuel materials because is an efficient, non-destructive, non-contacting, and quick measurement method to characterize the structure of graphitic materials such as TRISO-particles. Regardless of the specific model and manufacturer, each Raman spectroscope is equipped with electronic devices and a computer that controls the measurement process, it analyzes and processes the spectra. Raman spectroscope contains important basic elements such as an excitation source,

monochromator, detector, optical system, and recording system. The measurements performed on the p-TRISO samples were carried out by an inVia Renishaw micro-Raman system, and the spectra were collected by focusing a 785 nm laser beam in the spectral range of 200-3200 cm^{-1} [111].

4.1.6. ION IMPLANTER

The ion beam irradiation was performed using the UNIMAS ion implanter [112]. The most important parts of the ion implanter are the ion source, the acceleration system, and the target chamber. Before irradiating a given material, it is necessary to determine such parameters as energy and fluence. The dose of implanted ions must be precisely defined, reproducible, and homogeneous over the entire surface of the irradiated sample. In addition, the temperature of the bombarded target must be adjustable over a wide range (e.g. 77 K to 1300 K) [113] both during the implantation process and during the annealing of the samples after irradiation.

During irradiation experiment, the samples were attached to the sample holder using conducting carbon tape. The ion beam was produced using a universal arc discharge ion source. The irradiation current density was in the range from 0.01 $\mu A/cm^2$ up to 1 $\mu A/cm^2$ depending on the selected fluence. The pressure in the chamber was approximately 10^{-6} mbar. Residual gas pressure at the implantation stage is negligible and was not included in the performed experiment. In addition, the samples were irradiated at room temperature, and the thickness of the implanted layers ranges from a fraction to a single micrometer.

4.2. SIMULATION METHODS

In order to carry out the ion implantation experiment, it was first necessary to determine the value of the ion fluence at which the fuel samples under investigation would be implanted. The Stopping and Range of Ions in Matter (SRIM) and the Transport and Range of Ions in Matter (TRIM) programs were used to determine the proper ion fluence.

4.2.1. SRIM

SRIM program models the particle energy losses (electrons, protons, and neutrons), nuclear collision energy losses, as well as atomic collisions for ion beam irradiation [114][115][116][117]. This tool is commonly used to calculate the radiation damages that occur in the investigated material, which are generated by ion irradiation. SRIM enables calculations to obtain information on stopping powers, range, and straggling distribution parameters.

The SRIM data are produced for any ion type, at any energy, and for any specified target material. For the dissertation purpose, SRIM was used to determine the depth of ion penetration into the TRISO covering layers. Due to the measurement limitations of the Raman spectroscope, the depth of ion penetration could not be too shallow or too deep. Considering the small energy range (100-220 keV) of the ion implanter used in the experiment, the choice of energy was strictly dependent on the depth of ion penetration. To verify the parameters such as the depth of the ion penetration into the target or the energy level with which the target should be irradiated, the Ion Stopping and Range Tables were used.

4.2.2. TRIM

TRIM is an additional SRIM function that allows one to calculate the interactions of particles like ions or neutrons with a target. In the case of ions, two typical options for ion-induced damage profile calculations are used, namely: „Ion Distribution and Quick Calculation of Damage" (QD), and „Detailed Calculation with full Damage Cascades" (FC). The FC damage method simulates the overall collision cascade, while the QD method simulates only the trajectories of primary ions and the production of PKA [118][119][120][121][122]. The huge advantage of the TRIM code is the possibility to simulate neutron induced damage. The two possible modes of neutron calculations are: „Recoil cascades from neutrons, etc. (full cascades)", or „Recoil cascades from neutrons, etc. (quick KP damage)". Both methods require a TRIM.dat data file, which can be obtained by an external program such as Monte Carlo N-Particle Transport Code (MCNP). A detailed explanation of the TRIM.dat file was presented in Ref. [120][123][124][125][126]. For both ion and neutron simulations, the full calculation method was chosen. The full damage calculation mode provides a more accurate determination of damage energy, number of dislocations, and damage depth profiles than the fast damage calculation.

Users of the TRIM code have to specify several parameters such as the "DAMAGE", which sets options for calculations – ions vs neutrons and quick vs full simulation method; the "ION DATA", which specifies the ion type with which the target material will be bombarded, as well as its energy; and the "TARGET" material, which specifies the name of the target, its density, and thickness, as well as the chemical components of the target material. At the very end, the number of ions (app. 10000 ions) hitting the material is declared. Fig.4. 4. presents the event tree, which illustrates the penetration of ions into the structure of the material under investigation ("Depth vs Y-Axis"). A detailed description can be found in "9- TRIM: Output files" [127][128].

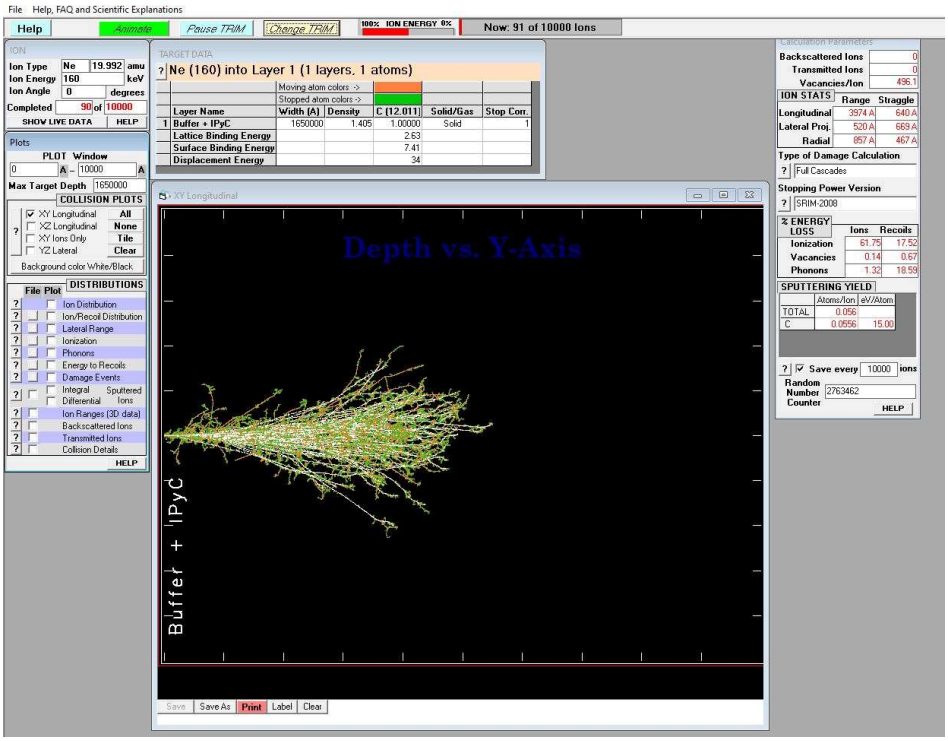

FIG.4. 4 TRIM – RUNNING CASE.

4.2.3. DPA

DPA is the parameter that provides information about the structural changes in the analyzed material. It is a number of point defects, meaning the average number of times an atom is displaced from the original lattice, which is widely used as an exposure parameter to evaluate the atomic-level structural damage in irradiated materials. The DPA parameter is used to make quantitative comparisons among ion and neutron irradiation and can be calculated using the Norgett, Robinson, and Torrens (NRT) formalism [129][130][131][132][133][134][129][135][136].

$$\text{NRT}=0.8\frac{T_d}{2E_D} \tag{3}$$

where, T_d is damage energy - energy that is available to generate atomic displacements by elastic collisions; E_D is threshold displacement energy – the minimum recoil energy to create stable defects.

E_D is a parameter that defines the minimum recoil energy to create stable defects, which might be obtained for any chemical component by an irradiation experiment, or predicted by molecular dynamics simulations [114][137]. The E_D is dependent on the lattice structure and can be obtained from ASTM Standards - E521.

5. EXPERIMENT

The assumptions for the design and fabrication of the TRISO-particle fuels were that the particles would remain intact and retain radionuclides over the range of conditions that could be encountered in normal operation and accidental conditions. The characterization of the TRISO-coating layers at the interface (junction) between the Buffer and IPyC layers remains unexplored. The need to investigate this problem derives from the fact that a potential mechanism of coating failure for TRISO-particles during irradiation is cracking of the IPyC layer due to densification of the Buffer layer when it is strongly bonded to the IPyC layer. Consequently, cracks in the IPyC layer may lead to the attack of the FP on the SiC layer [75]. The other possible scenario is the gap formation between the Buffer-IPyC interface. The main goal of this dissertation was to find a quick and efficient method for detecting layer failures in TRISO-particles at the front-end stage.

The experiment focused on irradiation-induced failures, and was conducted in two stages:

- stage I - analysis of the intact "virgin" sample;
- stage II - analysis of the sample after ion implantation.

To investigate specific damage phenomena, irradiation of the samples in the reactor core may be reflected by the ion implantation technique. Ion implantation is faster and easier to control than costly and time-consuming neutron irradiation process in the reactor core. Moreover, the results obtained from ion-irradiation gives a reasonable understanding of TRISO behavior. In this work, the phrase ion implantation is used alternatively with ion irradiation. The ion-irradiation experiment is explained in Section 5.2.

To perform ion implantation on TRISO samples, it is firstly necessary to properly prepare the samples. The samples must be polished to expose all the layers of which the tested fuel sample is composed. The uncovering of the TRISO sample layers is associated with damage occurring during the polishing stage itself. This mechanical damage is the result of the polishing method. To obtain the least distorted TRISO baseline structure, a suitable polishing method is required. The polishing procedure is explained in Section 5.1.

The main tool used to analyze the TRISO fuel particles is the Raman spectroscopy method. The measurements were performed in two steps, analysis of virgin samples and then of samples after ion irradiation. This means that in both stages, each of the TRISO layers was investigated in terms of the Raman spectrum, which represents the chemical composition of each coating

layer. In this work, the phrase coating layers is used alternatively with covering layers. Detailed information of the diagnostic methods is shown in Section 5.1.

5.1. P-TRISO

The experiment was performed on the coated-particle fuels produced at the Centre d'Études Nucléaires de Grenoble (CEA/Grenoble) in 2001. These nuclear fuel samples were manufactured for a TRISO fuel development, production and examination High Temperature Reactor project. Because the samples did not contain a uranium kernel and are made of one or two coating layers, they could be referred to as BISO particles. However, because these particles are predecessors to TIRSO, they are better described as an intermediate product, referred to as "p-TRISO". The batch of the p-TRISO samples is shown in Fig. 5. 1.

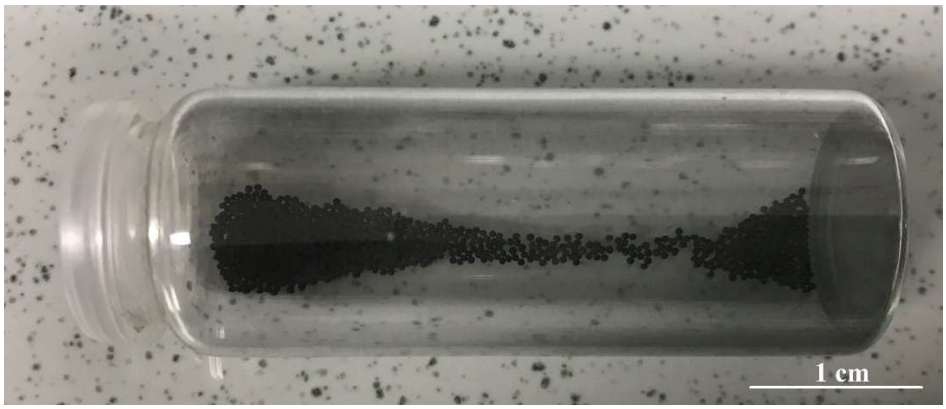

FIG. 5. 1 P-TRISO SAMPLES.

The surrogate p-TRISO samples consist of a zirconia dioxide (ZrO_2) kernel covered with pyrocarbon layers. The p-TRISO kernel is made of ZrO_2 94,% , Y_2O_3 5% with a density of 6 g/cm^3 and a diameter of 550 μm. Based on the composition of the covering layers, the p-TRISO samples were divided into three groups. Each group of particles has a different layer composition, and is described with a different symbol: Sample-1 (S-1), Sample-2 (S-2), Sample-3 (S-3) – shown in Fig. 5. 2. The S-1 samples are characterized by the fact that the kernel is covered with a Buffer layer; for S-2, the kernel is covered with an IPyC layer; and the kernels in the S-3 samples are covered with both Buffer and IPyC layers. Tab. 5. 1 provides information about the sample composition and the thickness of the layers. The thicknesses of the analyzed layers were measured with the use of optical microscope images using the ImageJ program.

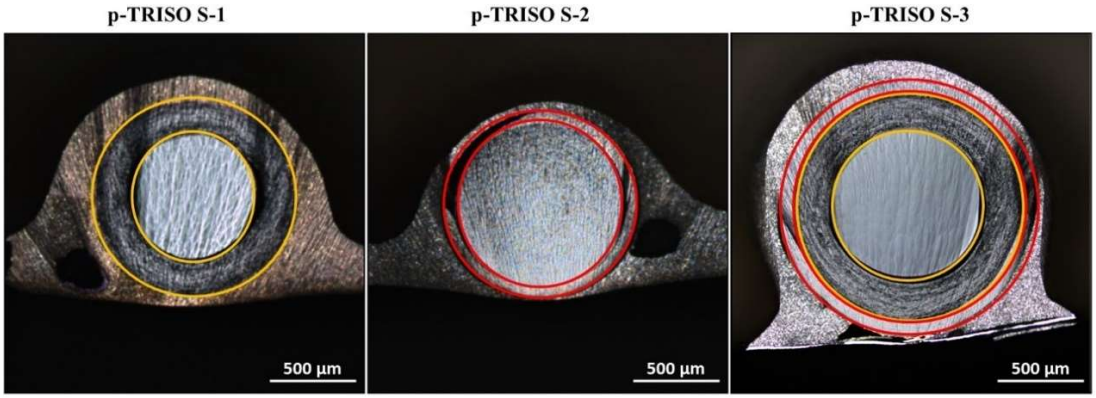

FIG. 5. 2 SEM IMAGES OF THE CROSS-SECTIONS OF THE P-TRISO SAMPLES BEFORE ION IMPLANTATION, WHERE WITH THE YELLOW COLOR THE BUFFER LAYER, AND WITH RED COLOR THE IPYC LAYER WERE MARKED [138].

TAB. 5. 1 THE P-TRISO SAMPLES.

Name of the sample	*Sample composition*	*Thickness of covering layer*
S-1	Kernel + Buffer	~ 120 µm
S-2	Kernel + IPyC	~ 45 µm
S-3	Kernel + Buffer + IPyC	~ 165 µm

5.1.1. POLISHING PROCEDURE

Preparing the samples for the ion-irradiation experiment involved polishing procedure for the p-TRISO samples. The reason for polishing the samples is the need to expose all of the layers of which the sample is composed. The preparation of the p-TRISO-particle must expose the interior with the least possible deformation of the surface structure. Two methods of polishing the TRISO samples have been applied, the mechanical and ionic. The mechanical polishing method can be invasive, and lead to significant damage in the p-TRISO layers at the polishing stage itself. For the mechanical polishing process, five fuel samples of the S-1 and S-2 type were selected. Fig. 5. 3. presents the SEM image of the S-2 p-TRISO sample polished by the mechanical method, with noticeable cracks on the IPyC layer. For the ion polishing process several samples from the S-1, S-2, and S-3 type were selected. Fig. 5. 4. presents the SEM image of the S-3 p-TRISO sample polished by the ionic method. The ionic polishing method does not interfere in the structure of the covering layers.

To verify which polishing method is better for further examination, the polished p-TRISO samples were measured with the use of several techniques, explained in detailed in Ref. [71]. Fig. 5. 5, Fig. 5. 6, and Fig. 5. 7 present the roughness measurements performed with the CLSM method on the S-1, S-2, and S-3 p-TRISO samples, respectively, with varying polishing methods.

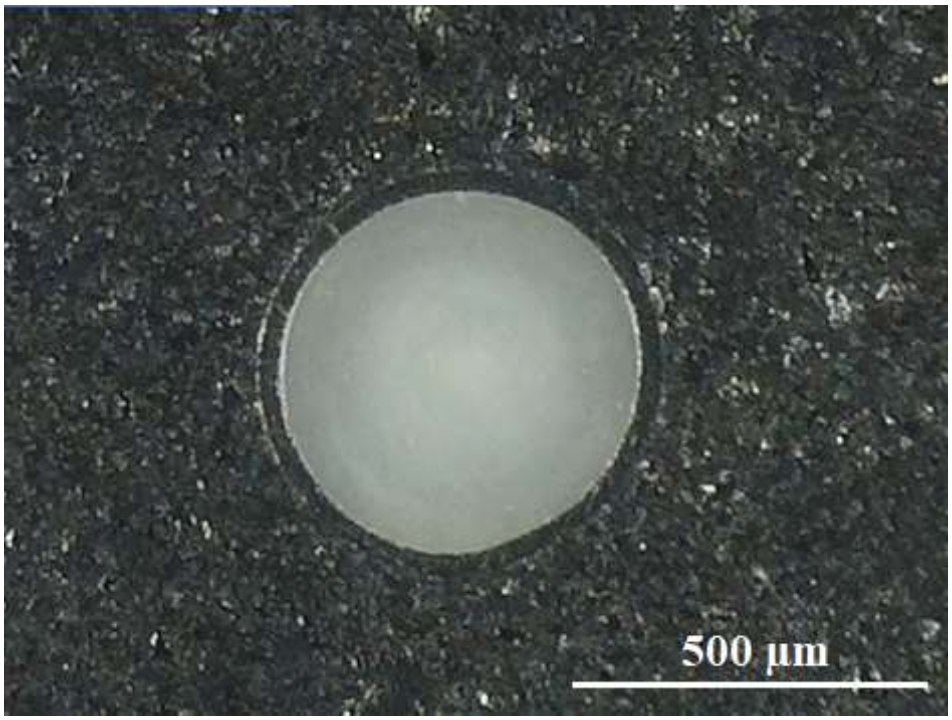

FIG. 5. 3 THE SEM IMAGE OF THE MECHANICAL POLISHED S-2 P-TRISO SAMPLE – WITH NOTICEABLE CRACKS IN THE COVERING LAYER.

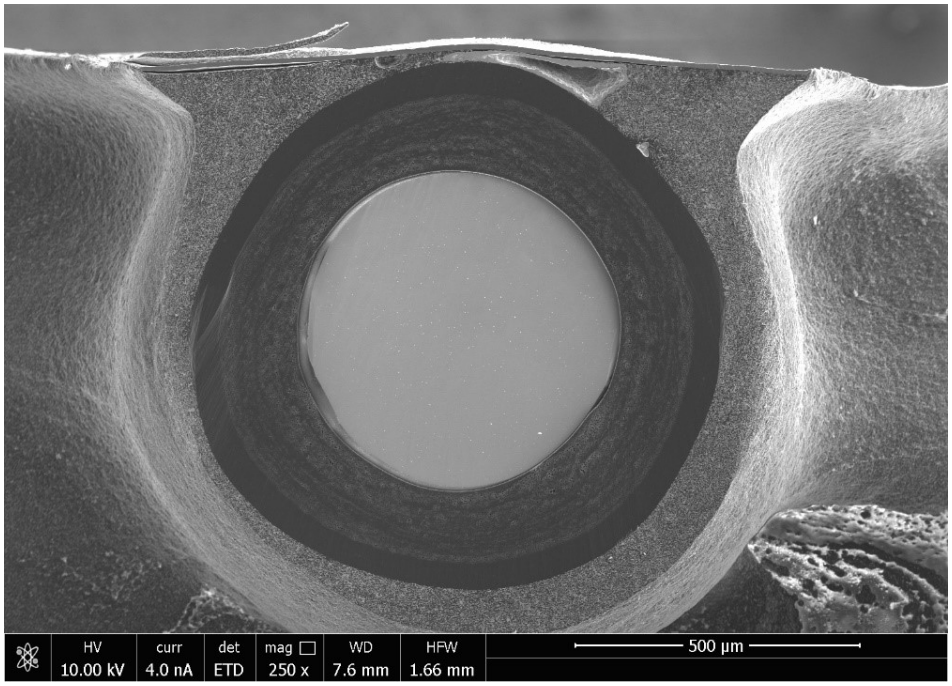

FIG. 5. 4 THE SEM IMAGE OF THE IONIC POLISHED S-3 P-TRISO SAMPLE - WITHOUT NOTICEABLE CRACKS IN THE COVERING LAYERS.

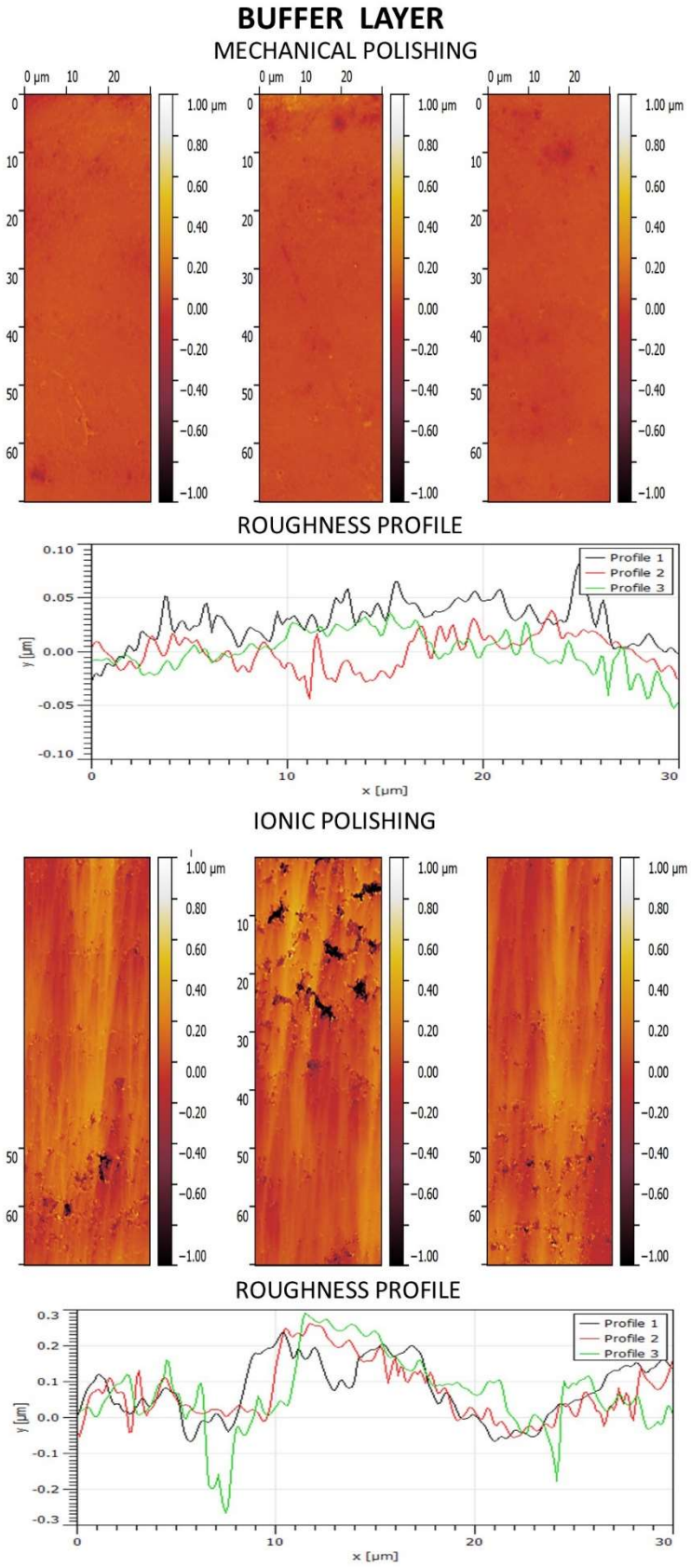

FIG. 5. 5 CLSM ROUGHNESS MEASUREMENTS ON THE BUFFER LAYER OF S-1 P-TRISO.

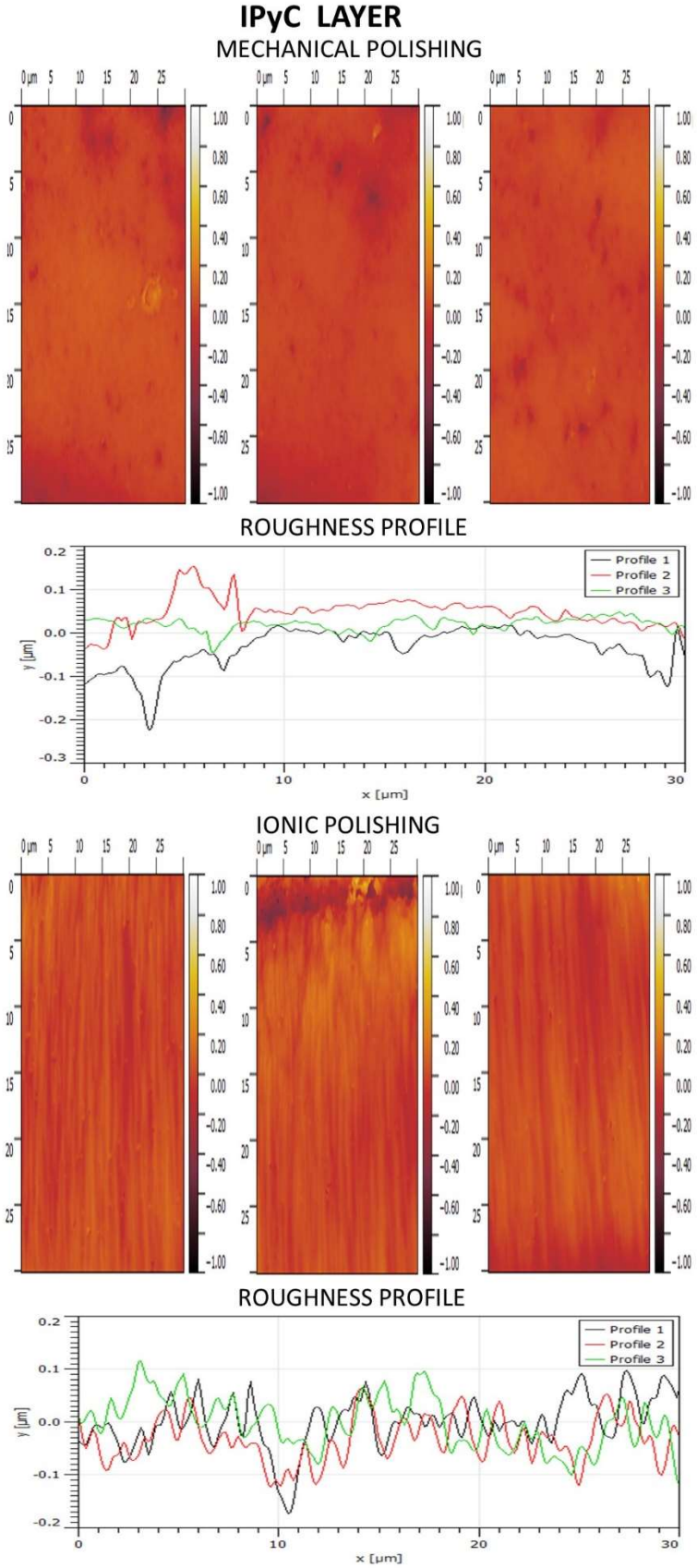

FIG. 5. 6 CLSM ROUGHNESS MEASUREMENTS ON THE IPYC LAYER OF S-2 P-TRISO.

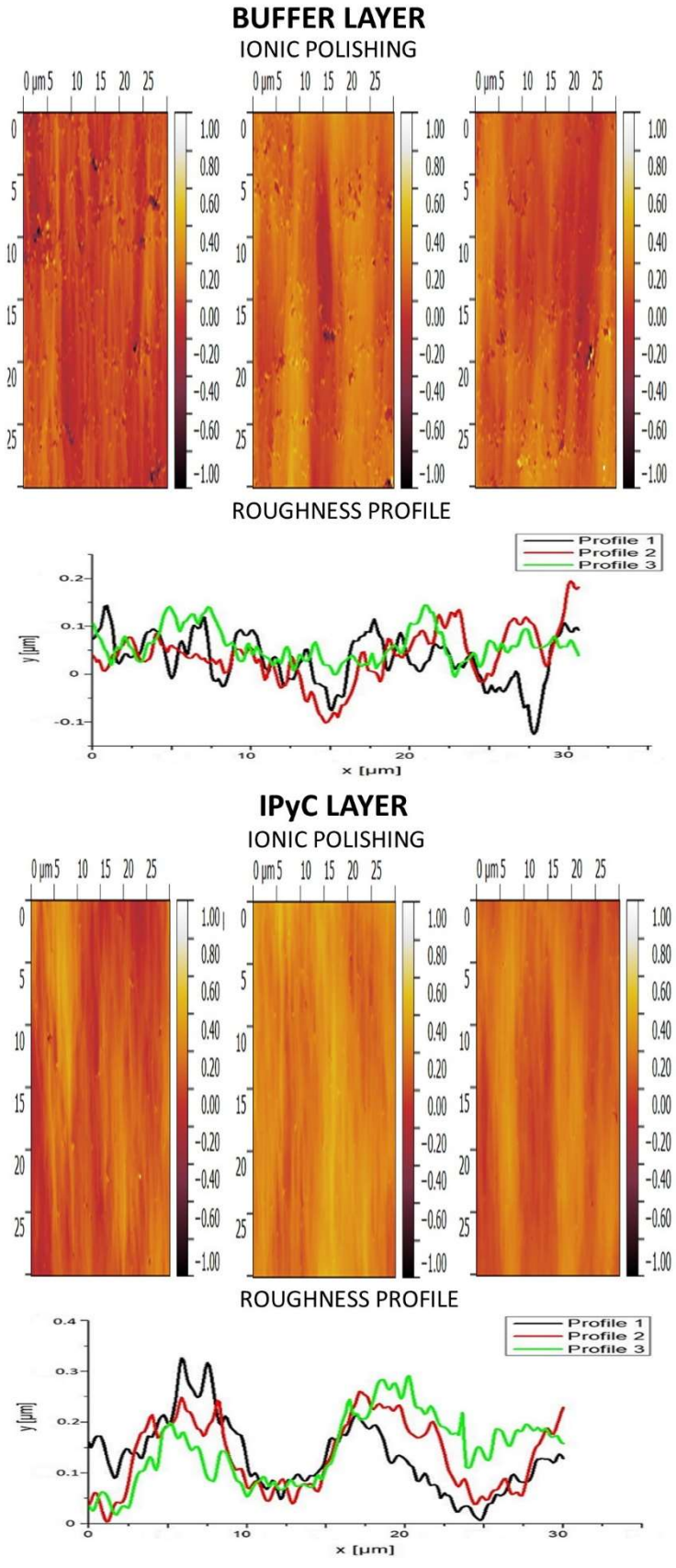

FIG. 5. 7 CLSM ROUGHNESS MEASUREMENTS ON THE BUFFER & IPYC LAYERS OF S-3 P-TRISO.

The most noticeable differences generated by polishing methods occur for the Buffer layer. Fig. 5. 8 shows the comparison of two polishing methods for the Buffer layer of the p-TRISO sample. As demonstrated by the CLSM, the mechanical polishing method spreads the polished material over the entire surface of the sample causing clogging of the pores of the Buffer layer, which simply smooths the analyzed surface. Due to the nature of the Buffer layer, i.e. its porosity, it is important for the further experiment to keep its structure unchanged. Any changes in the structure of that layer can affect the result of the further experiment. The ionic polishing method keeps the porous structure preserved, so that the difference between the Buffer and IPyC layers is visible.

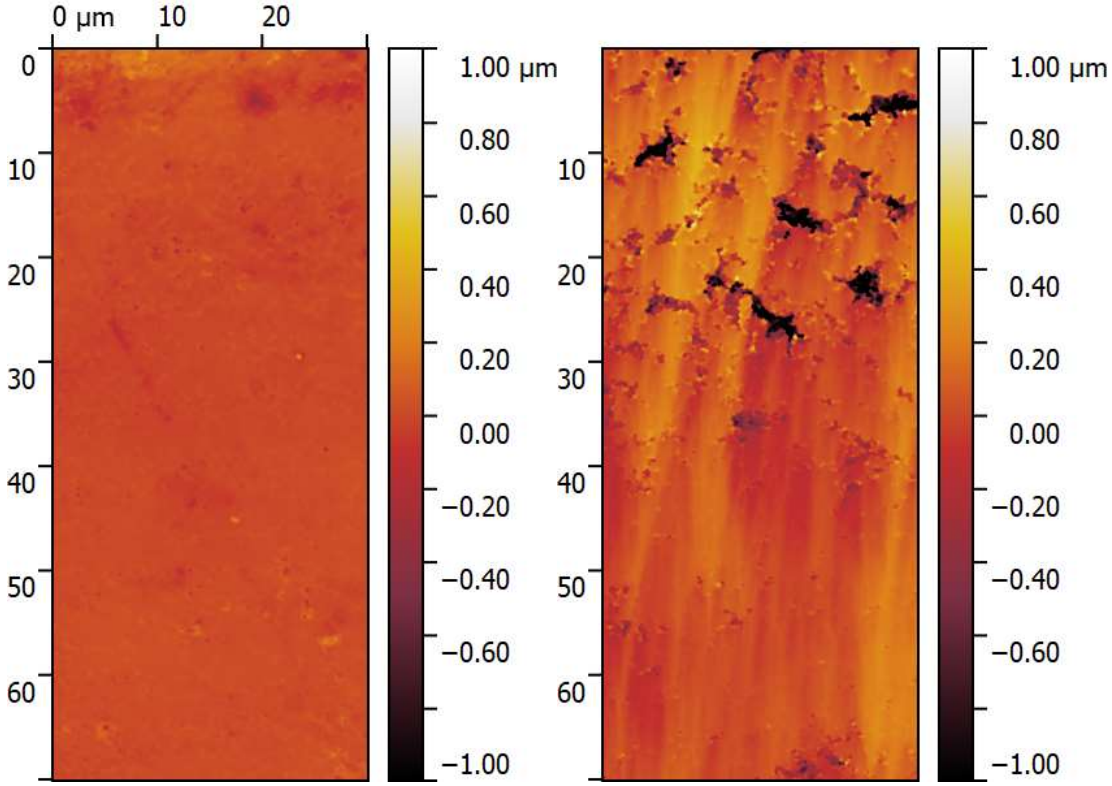

FIG. 5. 8 THE CONFOCAL LASER SCANNING MICROSCOPE IMAGE OF THE BUFFER LAYER. ON THE LEFT SIDE – MECHANICAL POLISHED BUFFER LAYER, ON THE RIGHT SIDE – THE ION POLISHED BUFFER LAYER.

Based on the obtained results it was concluded that the ion polishing method is a less invasive polishing procedure for p-TRISO samples. This method allowed using constant parameters, has repeatability (reliability) of results, and had a shorter lead time. With this, the ion polishing method interferes less with the structure of the tested material, which has the potential to improve further testing.

5.1.2. RAMAN SPECTRA OBTAINED FOR A PRISTINE GRAPHITE SAMPLE

The first stage of the ion-irradiation experiments on the p-TRISO-particles was devoted to graphite samples (Goodfellow, size: 50 x 50 mm, density: 2.26 g/cm^3). Graphite is structured in layers or lamellae with a hexagonal arrangement of covalent bonds, which as such is similar to the graphite-based material, like Buffer and IPyC layers. The structure of the graphite material is made of the localized in-plane sp^2 bonds and delocalized out-of-plane π bonds. The in-plane bonds are hybrids, while the delocalized are orbital bonds [96][139]. Since the analyzed p-TRISO samples consist of pyrolytic carbon layers, the use of graphite material helped to determine the energy and fluences required for the ion implantation of the p-TRISO samples.

The Raman spectrum of the pristine graphite sample shows well-ordered structure. The pristine graphite sample exhibited a characteristic G-band at the position of 1580 cm^{-1}, D-band at the position 1360 cm^{-1}, and a D'-band at the position of 1615 cm^{-1}. The G-band (G - graphite) is allocated to zone canter phonons at E_{2g} symmetry and is caused by the in-plane bond-stretching motion of sp^2 C atoms. The D-band (D - disorder) is allocated to the A_{1g} zone-boundary mode, which induces a band gap at 2D Brillouin zone of the carbon based materials. The second-order Raman spectrum reveals the three main bands, such G*-band (2450 cm^{-1}), 2D-band (2680 cm^{-1}), and 2D'-band (3250 cm^{-1}), where the 2D-, and 2D'-bands are the harmonics of Raman inactive fundamental modes in ordered carbons [140][141][142][143][144]. All of the bands are shown in Fig. 5. 9.

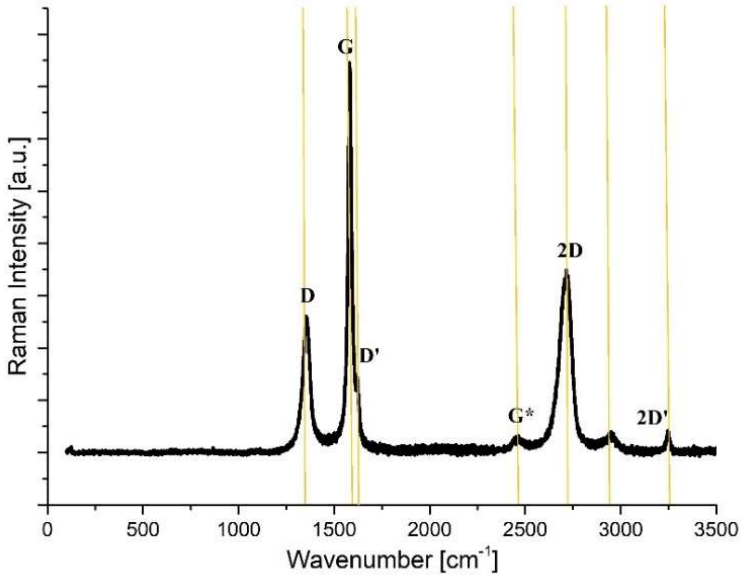

FIG. 5. 9 THE RAMAN SPECTRA FOR A PRISTINE GRAPHITE [145].

To determine the initial fluence for the p-TRISO samples, an ion-irradiation examination with Ne^+ ion implantation of fluences in the range of 10^{13} - 10^{16} ions/cm^2 was performed on the graphite samples. The Raman spectra were collected by focusing a 514.5 nm laser beam. Detailed explanation is presented in Ref. [138].

At the first stage of the graphite analysis, the graphite samples were irradiated with a fluence equal 10^{14} ions/cm^2, and with different energies. The energies: 100 keV, 130 keV, 160 keV, 190 keV, 220 keV were selected to estimate the optimal parameter with which the p-TRISO samples would be implanted. Fig. 5. 10 presents Raman spectra obtained with the dose of 10^{14} ions/cm^2 but with different implantation energies. The energy level does not influence the shape of Raman spectra. Considering the in-depth measurement of the sample, too high implantation energy may cause the ions to penetrate too deeply into the p-TRISO structure, and therefore cause a lack of observable results in the Raman spectra. In contrast, too low implantation energy significantly increases the sample implantation time. Based on that, the energy of 160 keV was selected due to the depth of ion penetration into the target layer, and due to the capabilities of the ion implanter device, and also by the limitations of the Raman spectroscope device.

In the second stage of the graphite analysis, the graphite samples were irradiated with an energy of 160 keV and with different fluences. The fluences: 10^{13} ions/cm^2, 10^{14} ions/cm^2, 10^{15} ions/cm^2, 10^{16} ions/cm^2 were selected to determine from what fluence the p-TRISO irradiation experiment should be started. Fig. 5. 11 shows significant G-, and D- band changes, which increase as the fluence increase. Due to that, and since the p-TRISO samples have different layer structure compared to the graphite samples, for the experiment with p-TRISO samples an initial fluence of 10^{12} ions/cm^2 was established.

Carbon based materials are difficult to study by SEM, because in comparison to other atoms at room temperature, their migration energy is low. Nevertheless, the major features of defect production and annealing can be well understood by assuming that vacancies govern the production and dynamics of radiation defects in graphitic materials. The PyC layer structure can be identified as isotropic, laminar, granular or columnar [146]. Fig. 5. 12, Fig. 5. 13, Fig. 5. 14, Fig. 5. 15, Fig. 5. 16, Fig. 5. 17, and Fig. 5. 18 show the SEM images of the graphite sample, which were irradiated with fluences in the range of 10^{13} - 10^{16} ions/cm^2. The defect agglomeration is seen as a continuous rupture of the basal planes, which ultimately leads to amorphization. This is noticeable with an increase of the ion irradiation fluence.

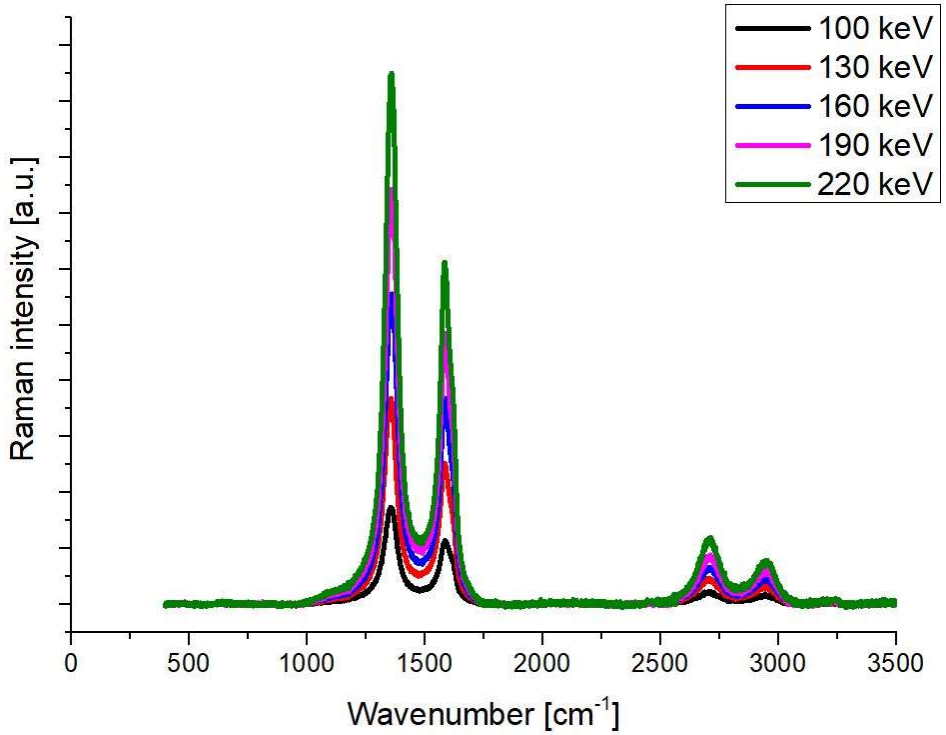

FIG. 5. 10 RAMAN SPECTRA OBTAINED FOR GRAPHITE (Ne^+, 10^{14} IONS/cm^2) - WITH RESPECT TO THE ENERGY WITH WHICH THE SAMPLE WAS IMPLANTED.

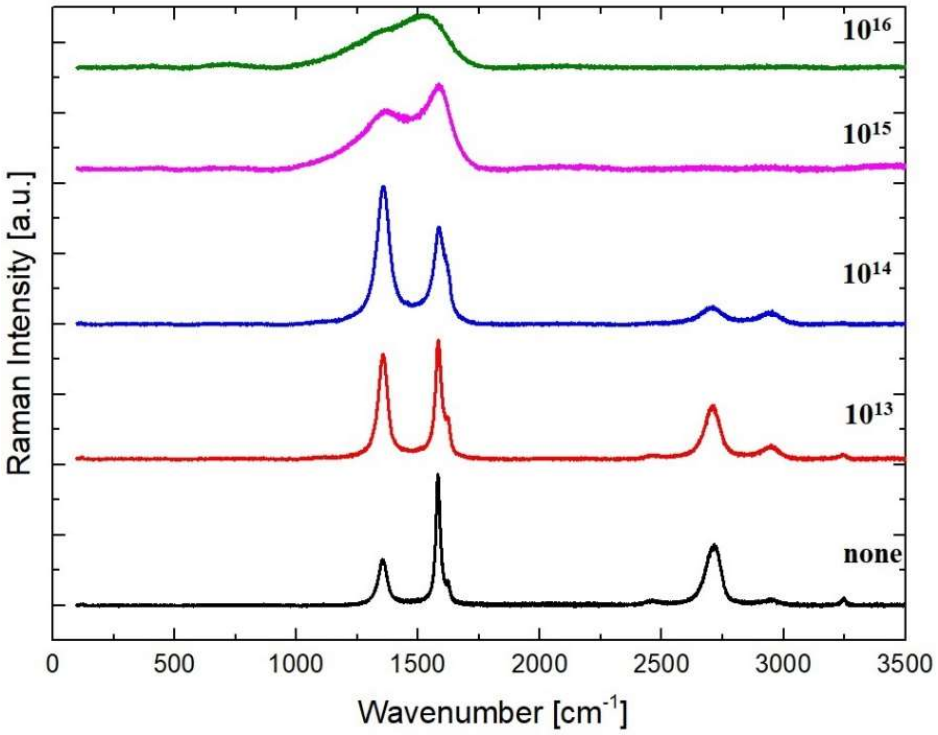

FIG. 5. 11 RAMAN SPECTRA OBTAINED FOR GRAPHITE (Ne^+, 130KEV) - WITH RESPECT TO THE IMPLANTATION DOSE, STARTING FROM A NON-IMPLANTED (PRISTINE) SAMPLE.

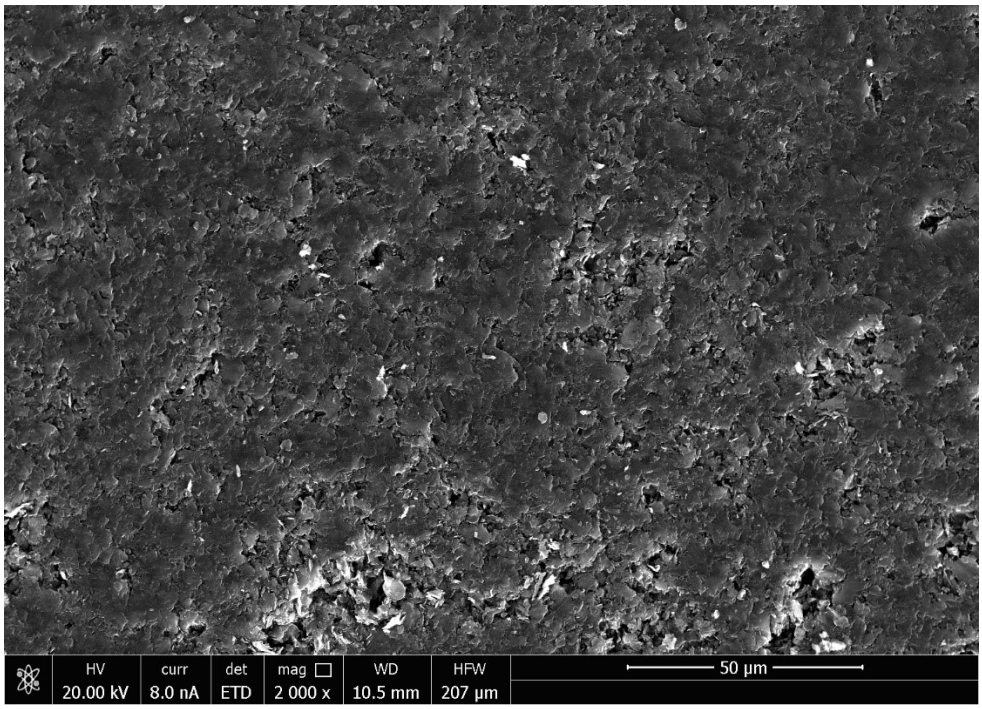

FIG. 5. 12 NON-IMPLANTED GRAPHITE.

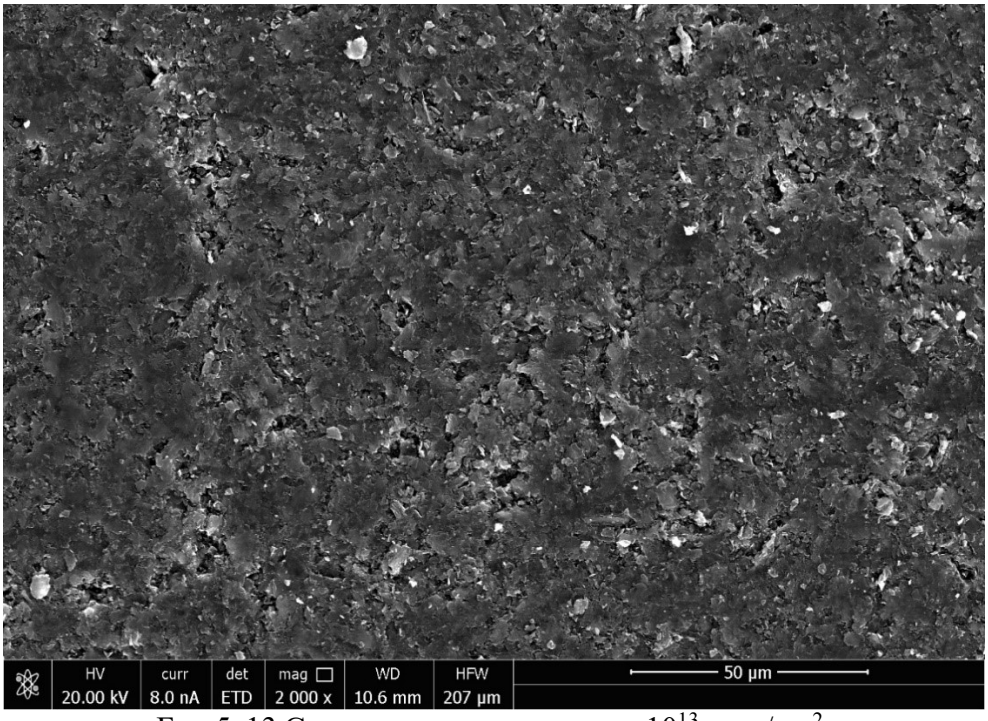

FIG. 5. 13 GRAPHITE IMPLANTED WITH 10^{13} IONS/CM^2.

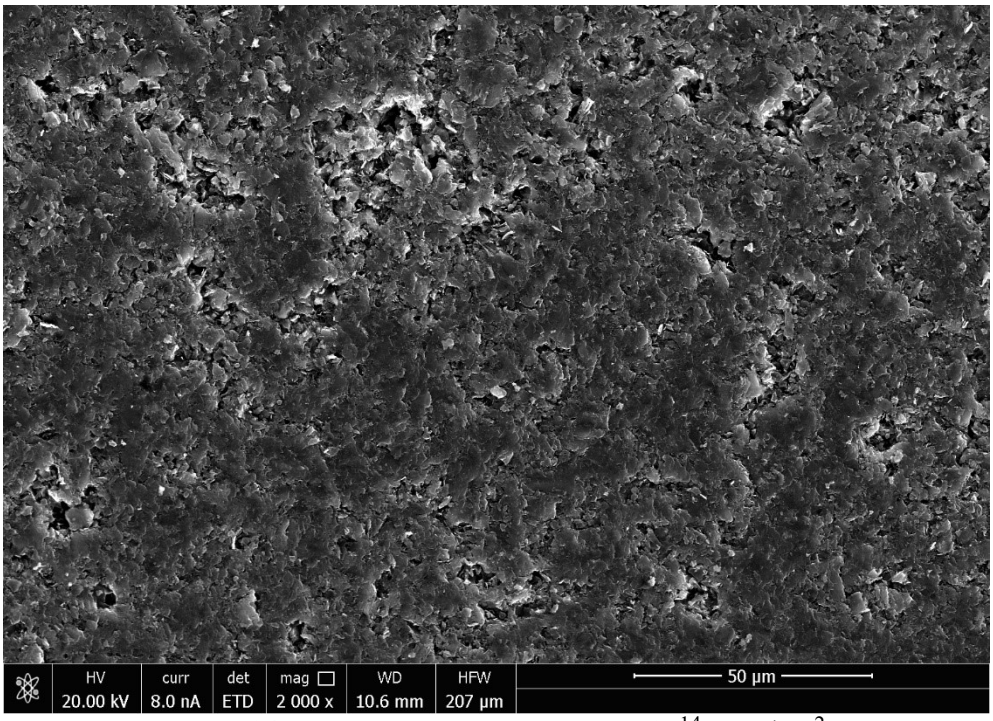

FIG. 5. 14 GRAPHITE IMPLANTED WITH 10^{14} IONS/CM^2.

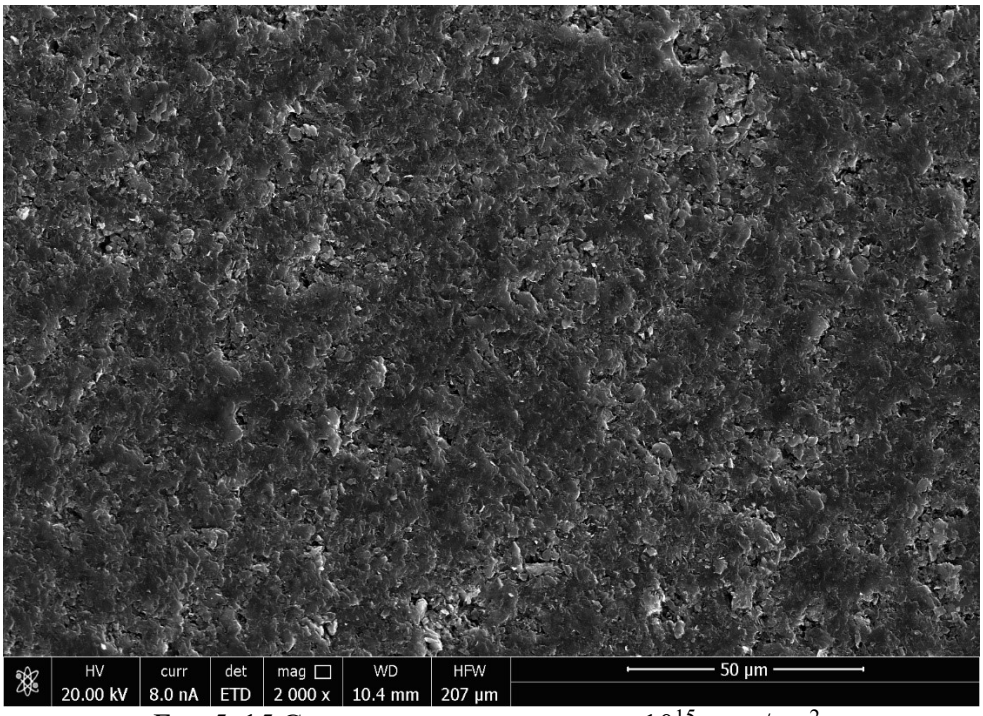

FIG. 5. 15 GRAPHITE IMPLANTED WITH 10^{15} IONS/CM^2.

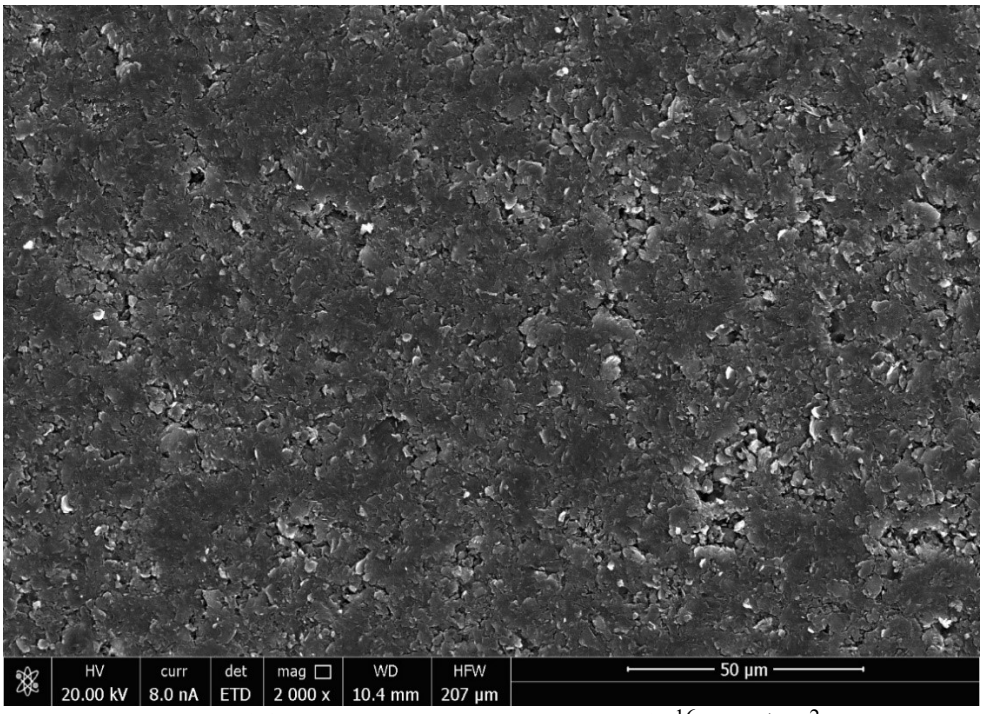

FIG. 5. 16 GRAPHITE IMPLANTED WITH 10^{16} IONS/CM^2.

The SEM images in the magnification (Fig. 5. 17, Fig. 5. 18) shows in detail the graphite structure damage due to increasing ion irradiation fluence.

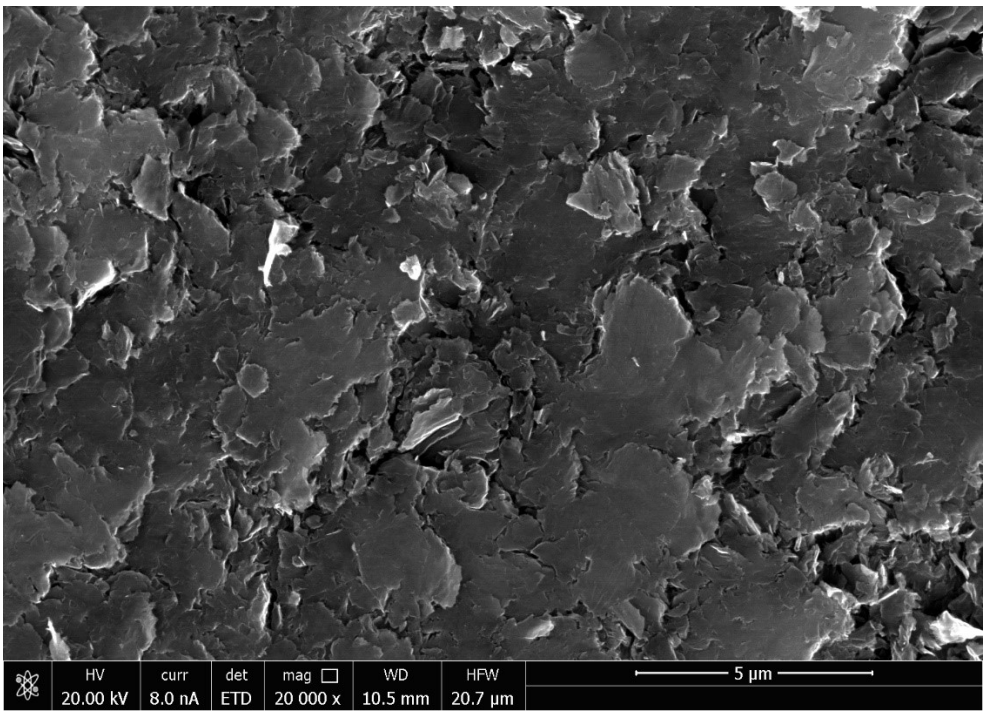

FIG. 5. 17 NON-IMPLANTED GRAPHITE – MAGNIFICATION.

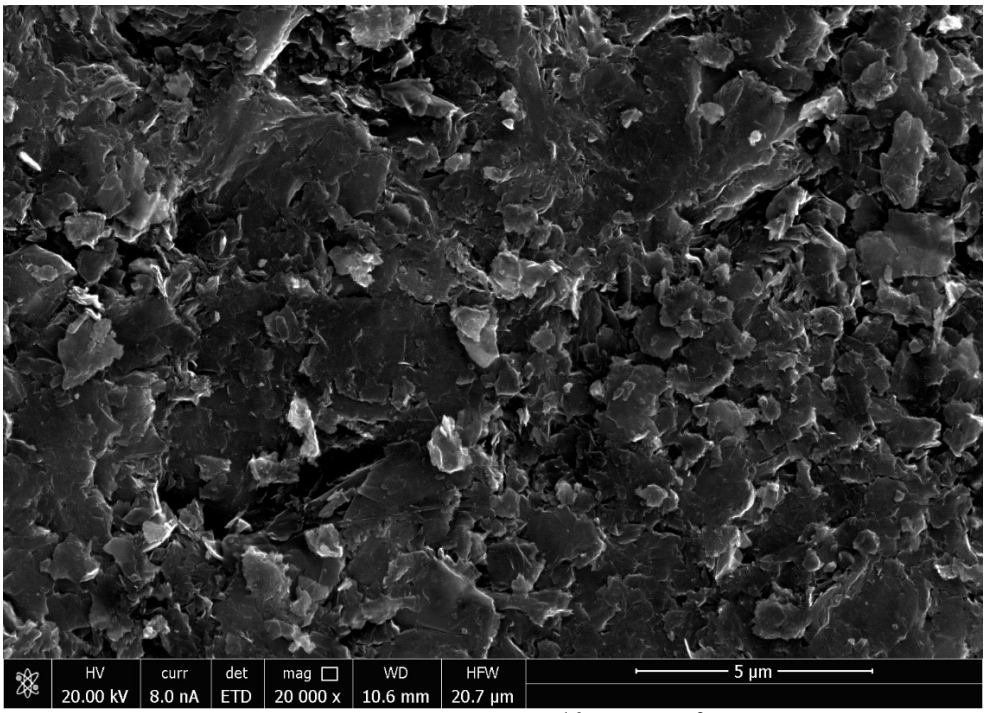

FIG. 5. 18 GRAPHITE IMPLANTED WITH 10^{16} IONS/CM^2 – MAGNIFICATION.

In conclusion, the experiment conducted on graphite has determined that ion implantation on p-TRISO-particles will be carried out at an energy of 160 keV starting with a fluence of 10^{12} ions/cm^2.

5.2. ION-IRRADIATION

The ion-irradiation technique was used to reflect the neutron irradiation process in the reactor core. This method allows determination of the level of damage occurring with irradiation to the p-TRISO-particles at a significantly faster rate, and without the necessity to deal with activated materials. The damaging processes that occur in the TRISO-particles loaded into the reactor core as nuclear fuel are more complicated than relatively simple radiation damage induced by ions. However, it is of real interest to assess and quantify the damage contribution coming from the interactions of ions with the TRISO layers. The differences between neutron irradiation and ion implantation, like energy (ions have smaller energies [keV] than neutrons [~ 2 MeV in fission system]) [147], charge (neutrons have no charge), and size; can potentially influence the experimental results. Nevertheless, this dissertation shows the advantages of using ion irradiation as a quick and efficient tool for p-TRISO sample investigation at the front-end stage.

Typically an ion irradiation experiment is performed with a noble-gas ions like: Ar^+, He^+, Xe^+, Ne^+, and Kr^+ [148][149][150][151]. The choice of the Ne^+ ions as a projectile is a trade-off between a long projected range of impinging particles, and the ability to produce damage due to the nuclear stopping mechanism, which gets stronger with the ion mass. The Ne^+

bombardment is considered as a tool for the generation of point defects [152] that accumulate both in metals [153] or semiconductors[154]. The reason for choosing helium ions comes from the fact that the ion penetration of these ions is deeper compared to the neon ions. In addition, helium is a chemical component that serves as a coolant in the HTGRs. Using He^+ ions as self-ions for damage creation allows ion irradiation to simulate the reactor core environment [155]. The disadvantage of ion implantation is that, even if high fluence can be achieved in a short time, the depth of penetration of the sample is shallow.

In this dissertation the results for Ne^+ and He^+ ion irradiation, with fluences that correspond to neutron irradiation in the reactor core of 1, 3 and 5 years are presented. Chapter 5.2.2 focuses on how different layers react to the ion irradiation induced damages, and verifies if the Raman spectroscopy tool can capture the changes. Chapter 5.2.3 focuses only on the S-3 p-TRISO samples. The goal of that experiment, was to reflect the damage that might occur after 1 and 5 years of neutron irradiation, at the interface of Buffer-IPyC layers. Finally, Chapter 5.2.4. focuses on the non-polished spheres of the p-TRISO samples. The goal for that experiment was to verify if the ion implantation process can be performed on the outer layer of the TRISO sample, and if the obtained results provide insight into the structural behavior caused by ion irradiation.

5.2.1. SRIM/TRIM CALCULATIONS FOR NEON AND HELIUM IONS

For the ion implantation experiments we selected two types of ions, neon (Ne^+) and helium (He^+), with which the p-TRISO samples were irradiated. The first experiment used only neon ions, and was performed on the S-1, S-2, and S-3 p-TRISO samples. The second experiment used neon and helium ions, and was performed on several S-3 p-TRISO samples, some of which were polished, and some not. To perform the ion irradiation experiments parameters like ion energy and ion fluence were calculated with the use of the SRIM/TRIM codes.

I. Energy level

The first step of the SRIM simulations was to select the energy level with which the p-TRISO samples were to be irradiated. Due to the measurement device's limitations, an energy of 160 keV was selected for both ion implantation experiments (explained in Chapter 5.1.2). Fig. 5. 19 describes that an incident energy of 160 keV allows Ne^+ ions to penetrate into p-TRISO layers to a depth of 4257 Å and to a depth of 9361 Å for He^+ ions. The reported values were obtained for a density of 1.405 g/cm^3, which is the sum of the densities of the Buffer (0.97 g/cm^3) and IPyC (1.84 g/cm^3) layers. The knowledge of the depth of ion penetration

confirms that Raman spectroscopy may be used for defect detection within p-TRISO-coating layers for the defined incident energy of 160 keV.

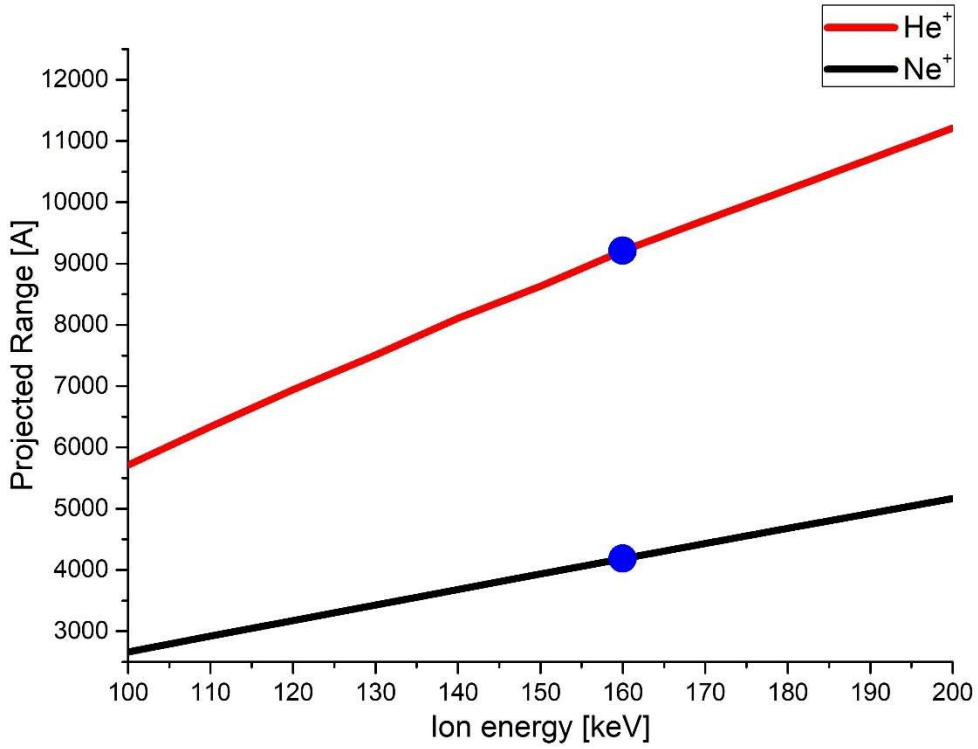

FIG. 5. 19 THE DEPTH OF NE^+ AND HE^+ IONS PENETRATION INTO P-TRISO SAMPLE.

II. Ion fluence

The calculation of the proper ion fluence that reflects the neutron fluence in the reactor core is performed in a few steps:

A. calculating the neutron fluence with the use of the MCNP code;

B. performing neutron and ion simulations in the TRIM code;

C. calculating the neutron DPA parameter;

D. recalculating the ion fluence with the use of the DPA from above.

A. For the neutron irradiation simulation in the TRIM code, the neutron fluence was calculated with the use of the Monte Carlo Continuous Energy Burn-up (MCB) code [156][157]. The calculations assumed the maximum neutron flux (sum of the thermal and fast neutron flux) of the HTR-10 reactor is $5.02*10^{13}$ n/cm^{2}s [31][158]. Based on the Go-HTR MCB model, performed in the frame of the studies in the strategic Polish program of scientific research and development work "Social and economic development of Poland in the conditions of globalizing markets GOSPOSTRATEG", part of "Preparation of legal, organizational and technical instruments for the HTR implementation" co-financed by the National Centre for Research and Development (NCBiR) in Poland, the neutron fluence was equal is $1.6*10^{13}$

neutrons/cm^2 after a year of constant irradiation. The applied Go-HTR model was developed for the purpose of the Polish national research program on HTGR industrial applications, as a heat source. In this model, each fuel rod in the reactor core is surrounded by a graphite sleeve and inserted into a cooling channel as originally designed for the Japanese HTTR. The detailed process of neutron fluence calculation with the use of the Go-HTR-MCB model was described in Ref. [124].

B. To perform the neutron and ion simulations in the TRIM code, several parameters had to be obtained. The implantation on the p-TRISO fuel was performed on the polished samples, and average values were used from the Buffer and IPyC layers for the target layer parameters in TRIM. The reason is that the polished sample is a cross-section on which ions fall perpendicularly on the surface of the layers, hitting the Buffer and IPyC layers equally. In the case of ion-irradiation on un-polished p-TRISO samples, the ions can hit the surface only from the outside, then only the IPyC layer is considered. It should be highlighted that in the case of neutron irradiation, the movement of neutrons is performed from the inside of the TRISO kernel, as well as from the outside. In that case, for the simulation, two separate layers of Buffer and IPyC layer were created. The values used in the simulations are shown in Tab. 5. 2.

TAB. 5. 2 INPUT PARAMETERS TO START TRIM SIMULATIONS

TRIM simulation	*p-TRISO sample composition*	*Layer thickness [µm]*	*Layer density [g/cm^3]*	*Threshold displacement energy (eV)*	*Lattice binding energy (eV)*	*Surface binding energy (eV)*
FC (ion)	Buffer + IPyC	165	1.405	34	2.63	7.4
full-damage (neutron)	Buffer IPyC	120 45	0.97 1.84	34	2.63	7.4

The Buffer and IPyC layers of p-TRISO samples could be considered as a comparable material to nuclear graphite because of the density of each layer, which is in the range of the density values of nuclear graphite [27][159][160]. Due to this fact, it was established that the E_D parameter for graphite-based structures is in the range of 30 - 35 eV. In the case of the analyzed p-TRISO particles, the E_D parameter was set a value equal to 34 eV [137][161][162][163][164][165][166][167]. The remaining two parameters lattice binding

energy, and the surface binding energy takes respectively the value of 2.63 eV and 7.4 eV [114]. These parameters allowed to perform the simulations of ions and neutrons collisions with the p-TRISO sample.

The TRIM plots (Fig. 5. 20, Fig. 5. 21.) describe the incident ion implanted concentration as a function of depth. As the figures show, for the collisions between implanted ions and the target, the trajectories of projectiles with the energies and angles of incidence on the sample deviate differently from the initial direction of the ion beam's incidence on the surface of the sample. The length of the path along which the bombarding ion travels in the target, from the point of entering the target, up to the point of complete stopping, is called as the total range of the ion or damage event tree.

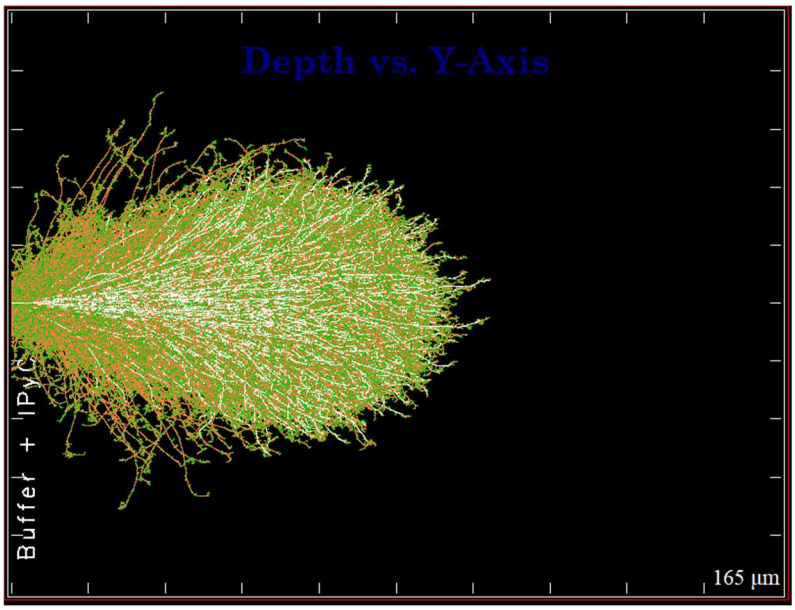

FIG. 5. 20 THE EVENT TREE FOR THE Ne^{+} ION IMPLANTATION.

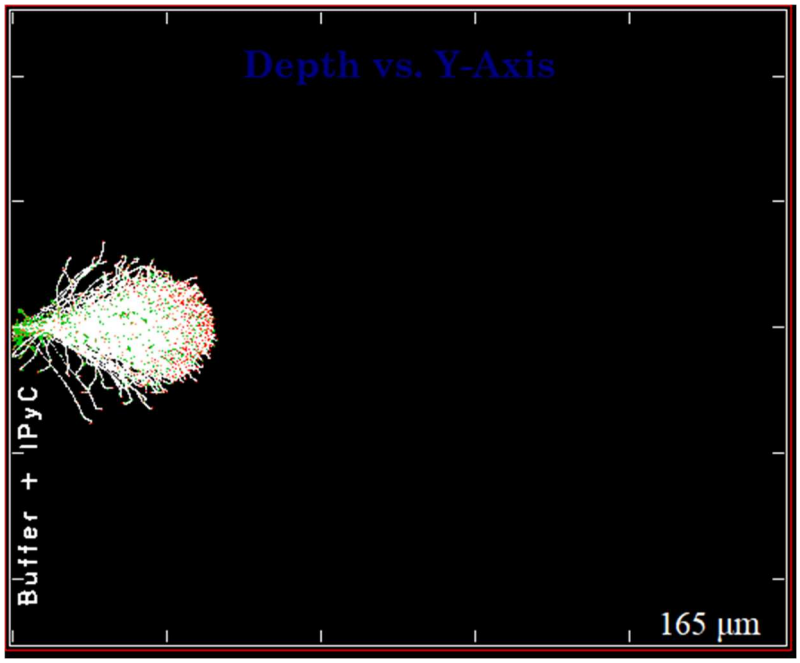

FIG. 5. 21 THE EVENT TREE FOR THE HE^+ ION IMPLANTATION.

C. The neutron fluence value ($1.6*10^{13}$ neutrons/cm^2) was used to calculate the neutron DPA distribution. The DPA parameter was used to make quantitative comparisons among ion and neutron irradiation data, which allowed to recalculate the ion fluence. The formula to calculate the DPA is as follows [120][148][151][168][169]:

$$DPA = \frac{\Phi * damage-rate * 10^8}{N} \quad (4)$$

where, Φ is the fluence, the damage-rate is in vacancies/ion/Å obtained with TRIM calculations based on summing columns from Vacancy.txt: „C vacancies" and z Novac.txt „number", across the width of "each incremental depth", and N is the atomic number density equal $7.169*10^{22}$ atoms/cm^3 for p-TRISO-particles.

D. Based on the neutron DPA the ion fluence was recalculated. Obtained on the external border of the p-TRISO-particle, the DPA value established the ion fluence value equal to $3.8*10^{16}$ ions/cm^2. For the ion implantation experiment, the ion fluence of $3.8*10^{16}$ ions/cm^2 reflect one year of neutron irradiation.

In the Chapter 5.1.2 several fluences were selected to check how the sensitive pyrocarbon layer responds to ion-induced damages. These fluences were used in the first part of the ion-irradiation experiment on the p-TRISO samples, to measure the particle behavior before reaching 1 year of irradiation. The first part of the ion irradiation experiment focus on the S-1, S-2, and S-3 p-TRISO samples (with an averaged layers width of 100 µm, and averaged density of 1.405 g/cm^3) subjected to ion-irradiation (Ne^+, 160 keV). Using the full cascades calculation method and taking into account ion penetration to a depth of 4183 Å in the Buffer+IPyC layers,

the DPA parameter was equal to: DPA (NRT)= 0.00189, and DPA (Fluence 10^{13})=0.00224. The previous values were obtained from the graph Fig. 5. 22 at the position 0.42 µm, because the aspect of ion penetration was taken into account.

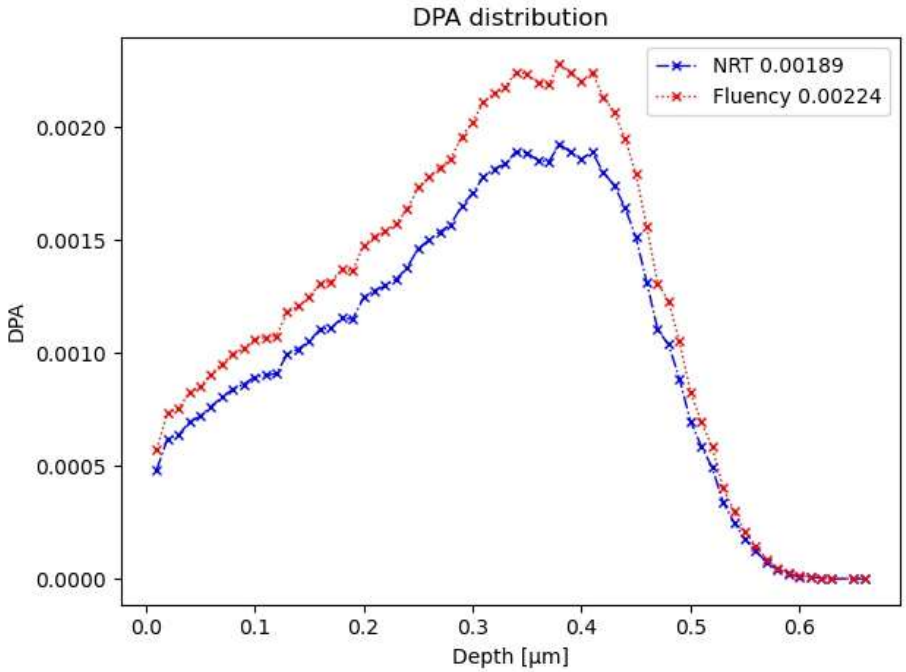

FIG. 5. 22 THE DPA PARAMETER OBTAINED FOR P-TRISO SAMPLE, CALCULATED WITH THE NRT FORMULA, AND "FLUENCY" FORMULA. THE DPA VALUES WERE READ FOR 4183Å DEPTH.

The fluences, which were used in the first part of the experiment, as well as the calculated DPA parameters are show in the Tab. 5. 3.

TAB. 5. 3 THE DPA VALUES OBTAINED DUE TO THE FLUENCES

Fluence [ions/cm^2]	*DPA*
$1*10^{12}$	0.000224
$1*10^{13}$	0.00224
$1*10^{14}$	0.0224
$1*10^{15}$	0.224
$1*10^{16}$	2.24

It can be noticed that with the increasing fluence of ion implantation the DPA parameter increases. An increase in the DPA parameter indicates that p-TRISO covering layers have experienced some damage. Fig. 5. 23 present the depth distribution of the DPA over each selected fluence.

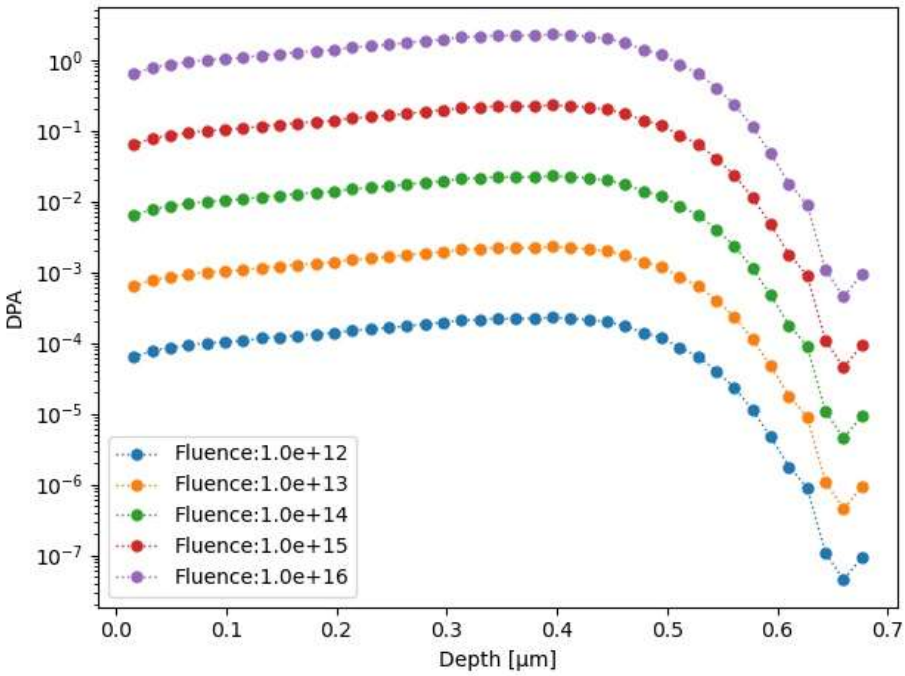

FIG. 5. 23 THE DEPTH DISTRIBUTION OF THE DPA.

In the second part of ion irradiation experiment Ne^+ and He^+ ions were used. The neon ions were used to irradiate the polished p-TRISO samples with the fluence that corresponds to 1, 3 and 5 years of neutron irradiation. In addition, the non-polished p-TRISO samples were irradiated with helium ions at a fluence that reflects 3 years of neutron irradiation. The summarize data are presented in the Tab. 5. 4. The DPA parameter was calculated for the Ne^+ and He^+ ion- irradiation experiment assuming several fluences that correspond to the neutron irradiation times of the TRISO samples in the reactor core.

TAB. 5. 4 SUMMARIZED DATA FOR ION-IRRADIATION

Ion energy	*Fluence [ions/cm^2]*	*DPA*	*Year of neutron irradiation*
	$3.8*10^{16}$	8	1
Ne^+ (160keV)	$1.1*10^{17}$	23	3
	$1.9*10^{17}$	40	5
He^+ (160keV)	$1.05*10^{18}$	24	3

Under reactor conditions, the majority of atomistic displacements in TRISO-particle fuel occur due to elastic and inelastic scattering of the neutrons. An increase in the DPA parameter indicates that p-TRISO covering layers have initiated some damage. The higher the value of the DPA the more likely structural defects are observed.

5.2.2. EXPERIMENT ON S-1, S-2, S-3 P-TRISO SAMPLES

In this part, the results from the ion implantation experiment, performed on S-1 (Buffer), S-2 (IPyC), and S-3 (Buffer+IPyC) p-TRISO samples are presented. Each of the p-TRISO samples was implanted with Ne^+ ions with a fluence in the range of 10^{12}- 10^{16} ions/cm^2. This experiment was conducted in several steps:

- Polishing the sample with ion-polishing method;
- Raman spectroscopy measurement on the polished intact surface;
- Ne^+ ion irradiation with a fluence equal 10^{12} ions/cm^2;
- Raman spectroscopy measurement;
- SEM imaging;
- Ne^+ ion re-irradiation up to a fluence of 10^{13} ions/cm^2;
- Raman spectroscopy and SEM measurements;
- etc.

Ion implantation was performed on three p-TRISO samples, one of each type (S-1, S-2, S-3). This means that each sample was firstly implanted with the first dose (10^{12} ions/cm^2), and then after SEM and Raman spectroscopy measurements, it was re-implanted to achieve the second dose (10^{13} ions/cm^2). The procedure was repeated until the samples were implanted with the fluence of 10^{16} ions/cm^2. The ion implantation was performed over the entire surface and perpendicular to the polished surface of each analyzed p-TRISO samples. Due to that, the obtained results will be the same no matter on which spot of the layer the further measurement will be performed. The measurements on the implanted p-TRISO samples were carried out by an inVia Renishaw micro-Raman system. The Raman spectra were collected by focusing a 785 nm laser beam in the spectral range of 200 - 3200 cm^{-1}. Compared to graphite, pyrolytic p-TRISO layers are much softer. Measurements conduced with 514 nm laser beam caused burns in the structure of the analyzed layers. In comparison, the 785 nm laser beam did not interfere with the structure of the layer allowing measurements to be taken. The obtained Raman spectra were normalized and fitted to the convolution profile of Gaussian and Lorentzian functions using WiRE 3.4 software. At the time of matching, the program determines for itself where the background is and disregards it. The intensity of the background did not change/make a difference in the obtained values of the intensity of the bands. Fig. 5. 24, Fig. 5. 25, Fig. 5. 26, and Fig. 5. 27 shows Raman spectra obtained for different fluences with which each sample was irradiated.

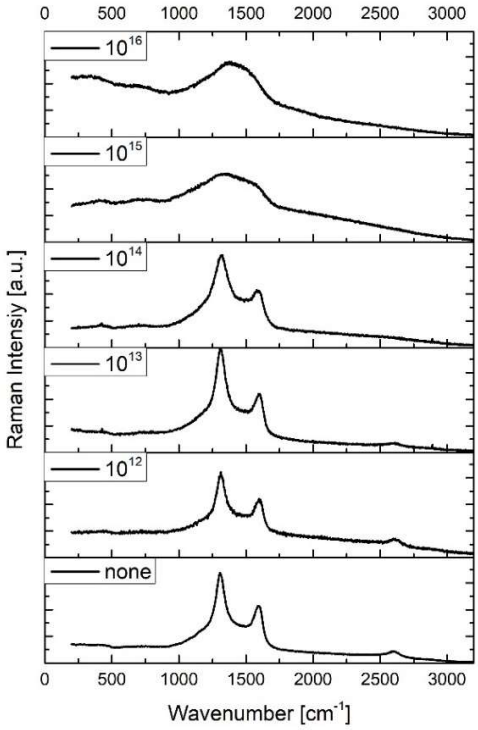

FIG. 5. 24 THE RAMAN SPECTRA OF THE BUFFER LAYER OF THE S-1 P-TRISO SAMPLE FOR DIFFERENT ION FLUENCES.

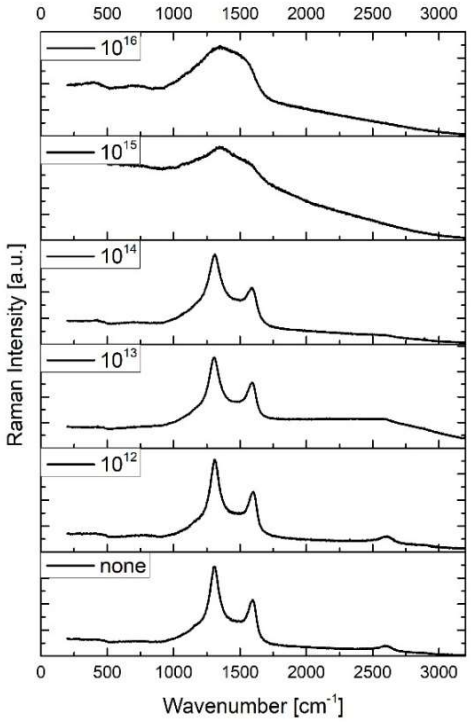

FIG. 5. 25 THE RAMAN SPECTRA OF THE BUFFER LAYER OF THE S-3 P-TRISO SAMPLE FOR DIFFERENT ION FLUENCES.

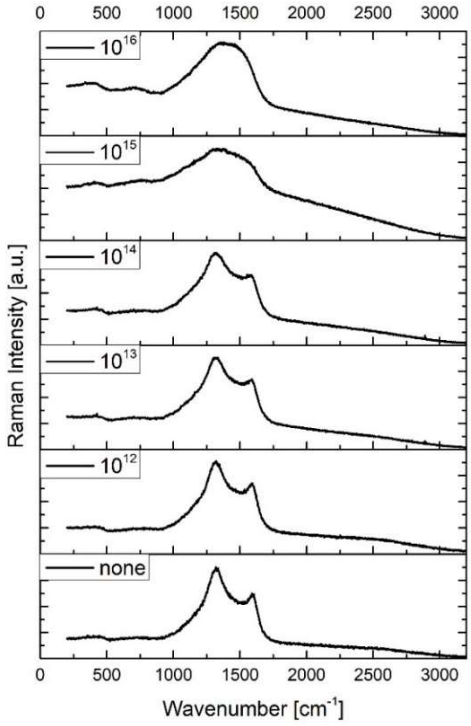

FIG. 5. 26 THE RAMAN SPECTRA OF THE IPYC LAYER OF THE S-2 P-TRISO SAMPLE FOR DIFFERENT ION FLUENCES.

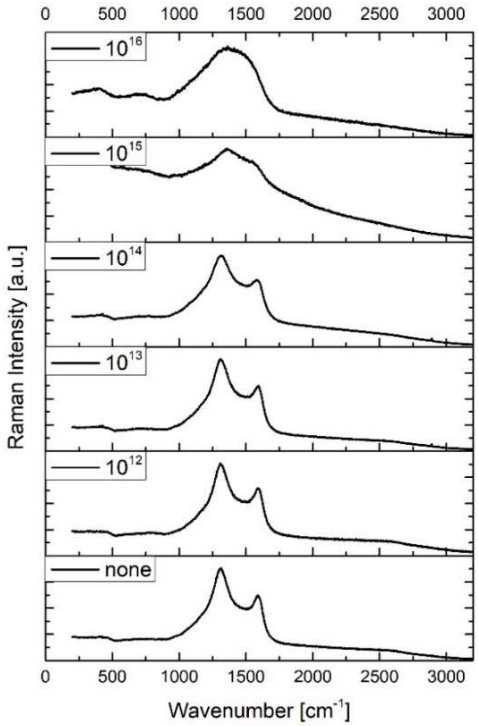

FIG. 5. 27 THE RAMAN SPECTRA OF THE IPYC LAYER OF THE S-3 P-TRISO SAMPLE FOR DIFFERENT ION FLUENCES.

Based on the presented figures it is concluded, that due to the increasing fluence, the change in the position of the D- and G- bands is observed, described in the Tab. 5. 5, Tab. 5. 6, Tab. 5. 7, and Tab. 5. 8. The D-band has changed in the range of 1310 cm^{-1} - 1370 cm^{-1}, and G-band changed in the range of 1520 cm^{-1} - 1580 cm^{-1}. An increase in the width of the D- and G- bands as well as an increase in the position of these two bands indicates the formation of a defect. The increase in the D-band intensity indicates a decrease in the crystallite size. The most noticeable change is observed in the bandwidth of the Raman spectrum at the fluence of 10^{14} ions/cm^2, which is more noticeable for the Buffer layer, and less for the IPyC layer. As the fluence further increases (fluence of 10^{15} ions/cm^2), the Raman spectrum changes in a manner that from two separate bands only one band was formed. To distinguish the two bands, a deconvolution method was used to decompose that bands that overlap with each other. Due to that, it was assumed that the ion irradiation reduces the dimensions of the ordered layer structure, which is due to the appearance of the ID/IG ratio at low defect levels. The single wide peak is known as the D''-band, located at around 1500 cm^{-1}, which originates due to the merging of D-, and G bands. The D'' -band indicates the destruction of the graphitic microcrystals and cause the formation of an amorphous structure [27][139][170]. The amorphous material is material where the structure is fully disordered.

A detailed analysis of the Raman spectra for each p-TRISO samples is presented in the tables below (Tab. 5. 5, Tab. 5. 6, Tab. 5. 7, Tab. 5. 8). The presented tables include data related to the parameters such as the width of the G-, and D-bands; and the ratio of the band intensity of the D-Raman band, and the G- Raman band (ID/IG). The ID/IG ratio was calculated from the band intensity and the area (integral intensity).

TAB. 5. 5 PARAMETERS OBTAINED FOR THE BUFFER LAYER OF SAMPLE S-1

Fluence	*Position*		*Width*		*ID/IG*	*ID/IG*
	D- band	**G-band**	**D- band**	**G-band**		*area*
before implantation	1310.3±0.6	1583.2±0.9	141.1±4.1	109.2±2.4	1.63±0.04	2.1±0.06
$1*10^{12}$	1313.9±0.7	1587.3±0.4	138.9±4.3	113.2±2.3	1.72±0.04	2.1±0.06
$1*10^{13}$	1312.7±0.9	1584.3±1.4	125.5±12.2	119.8±6.6	2.03±0.11	2.15±0.24
$1*10^{14}$	1316.5±0.3	1577.2±0.6	195.3±8.4	139.8±5.5	2.16±0.1	3.73±0.6
$1*10^{15}$	1348.5±3.5	1564.3±2.3	520.4±26.5	143.9±6.5	4.87±0.42	23.93±4.57
$1*10^{16}$	1373.7±10.9	1532.3±7.1	414.9±20.5	166.5±21.1	4.4±1.46	15.8±8.98

TAB. 5. 6 PARAMETERS OBTAINED FOR THE BUFFER LAYER OF SAMPLE S-3

Fluence	*Position*		*Width*		*ID/IG*	*ID/IG*
	D- band	**G-band**	**D- band**	**G-band**		*area*
before implantation	1309± 0.4	1583.8±1.1	140.5±3.1	106±2.3	1.69±0.03	2.05±0.03
$1*10^{12}$	1310.7±0.9	1584.2±1.5	134.9±4.6	111.7±3.9	1.66±0.04	2.01±0.05
$1*10^{13}$	1308.8±1.6	1581.8±1.6	141.5±9.7	116.2±3.7	1.79±0.09	2.18±0.08
$1*10^{14}$	1310.9±1.6	1575.1±1.5	196±15.5	140.7±7	1.95±0.08	3.09±0.25
$1*10^{15}$	1372.8±6.3	1579.7±2.5	513.1±65.5	130.5±21.9	6.47±1.96	39.97±26.81
$1*10^{16}$	1355.2±7.2	1549.8±13.7	487.6±26.5	134.6±21.5	4.25±0.54	21.45±6.05

TAB. 5. 7 PARAMETERS OBTAINED FOR THE IPYC LAYER OF SAMPLE S-3

Fluence	*Position*		*Width*		*ID/IG*	*ID/IG*
	D- band	**G-band**	**D- band**	**G-band**		*area*
before implantation	1315.6± 1.5	1578.2±0.6	243.3±3.2	129±2.5	1.56±0.06	3.34±0.25
$1*10^{12}$	1317.4±0.7	1579.9±0.6	242.4±6.2	134±1.4	1.76±0.05	3.59±0.26
$1*10^{13}$	1312.1±4.6	1577.5±1.3	243.8±19.2	132.8±3.2	1.89±0.09	4.05±0.76
$1*10^{14}$	1314.8±3.8	1574.3±0.9	277.7±18.6	138.3±2.2	2.09±0.09	5.29±0.94
$1*10^{15}$	1377.6±15.9	1569.8±7.3	419.1±27.3	167.1±30.9	3.28±0.33	9.78±3.29
$1*10^{16}$	1327.5±7.5	1521.1±4.1	434.6±16.7	193.1±9.8	2.69±0.41	7.92±2.08

TAB. 5. 8 PARAMETERS OBTAINED FOR THE IPYC LAYER OF SAMPLE S-2

Fluence	*Position*		*Width*		*ID/IG*	*ID/IG*
	D- band	**G-band**	**D- band**	**G-band**		*area*
before implantation	1335.4± 4.6	1580.9±0.9	281.9±18.7	144±9.1	2.09±0.07	4.21±0.37
$1*10^{12}$	1328.3±4.4	1577.7±1.8	293.3±17.1	139.9±3.3	2.09±0.2	5.68±1.21
$1*10^{13}$	1326.2±1.9	1577.3±0.9	299.1±11.3	135.4±2.2	2.12±0.11	6.28±0.92
$1*10^{14}$	1328.9±1.1	1576.4±0.8	349.3±4	137.6±0.8	2.49±0.04	9.12±0.35
$1*10^{15}$	1349.6±7.5	1560.3±2.9	515.8±30.9	144.9±10.5	4.93±0.85	23.54±7.67
$1*10^{16}$	1339.8±11.0	1525.1±7.8	439.3±21.0	179.1±17.1	2.89±0.64	9.55±3.76

An interesting phenomenon is the decreasing value of the position and width of the D- and G- bands at fluence of 10^{16} ions/cm^2. This behavior may be evidence of repair in the damaged structure. This is due to the mechanism of returning the knocked-out atoms to their previous position in the structure. The presented analysis of the obtained Raman spectra was performed for samples S-1, S-2 and S-3. It can be concluded that regardless of which sample was

measured, the same defect formation mechanics occur for the Buffer layer (in sample S-1 and S-3) and the IPyC layer (in sample S-2 and S-3).

The change in the structure of the covering layers is observed at each of the p-TRISO layers, which arise due to the increasing ion-irradiation fluence. The main interesting aspect of damage formation at the covering layers appears at the interface of Buffer-IPyC layers of the S-3 p-TRISO sample. Due to that, more detailed analysis was performed on the S-3 p-TRISO sample. Fig. 5. 28, Fig. 5. 29, and Fig. 5. 30 presents the Raman maps obtained for the S-3 p-TRISO sample. The maps were obtained for a non-implanted sample, and then after ion implantation with the fluence equal 10^{14} ions/cm^2, and 10^{16} ions/cm^2. Each map is an representation of the Buffer-IPyC interface. In all presented cases, the Buffer layer is at the bottom (0-15 µm), when the IPyC layer is at the top (15-30 µm) of the Raman map.

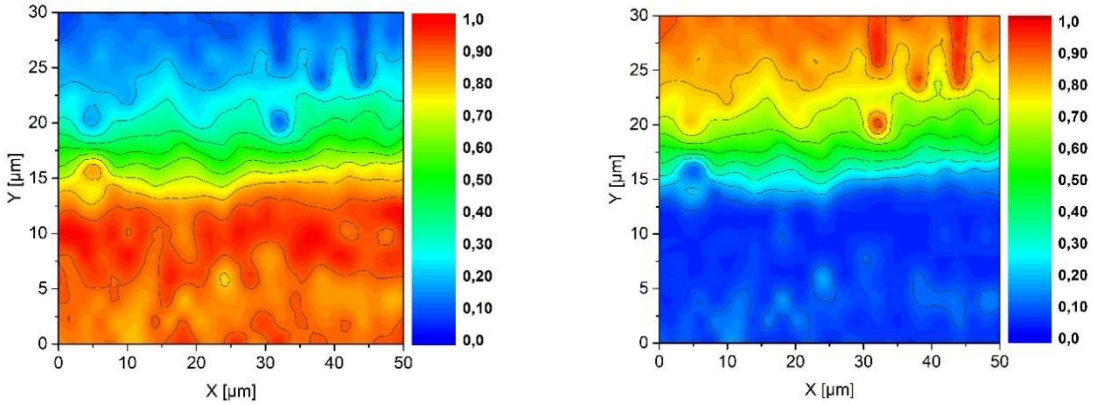

FIG. 5. 28 THE RAMAN MAP IMAGES OF SAMPLE S-3- NON-IMPLANTED.

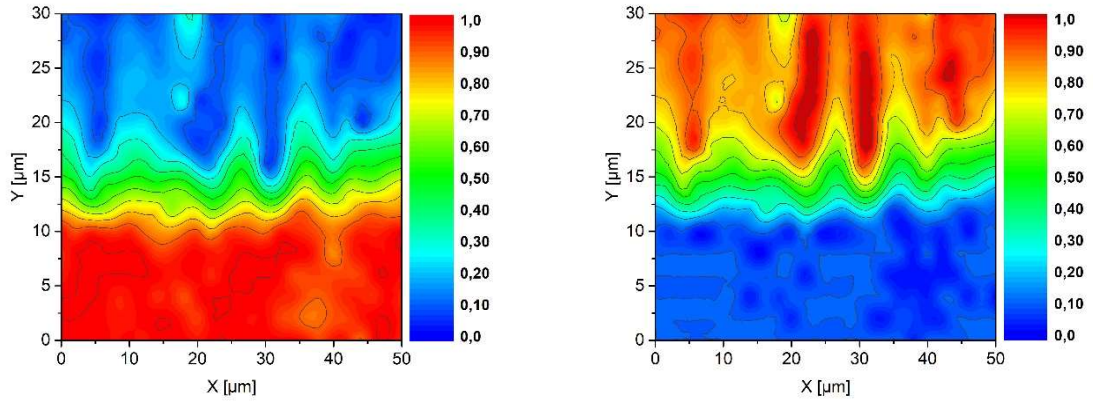

FIG. 5. 29 THE RAMAN MAP IMAGES OF SAMPLE S-3- WITH THE FLUENCE OF 10^{14} IONS/CM^2.

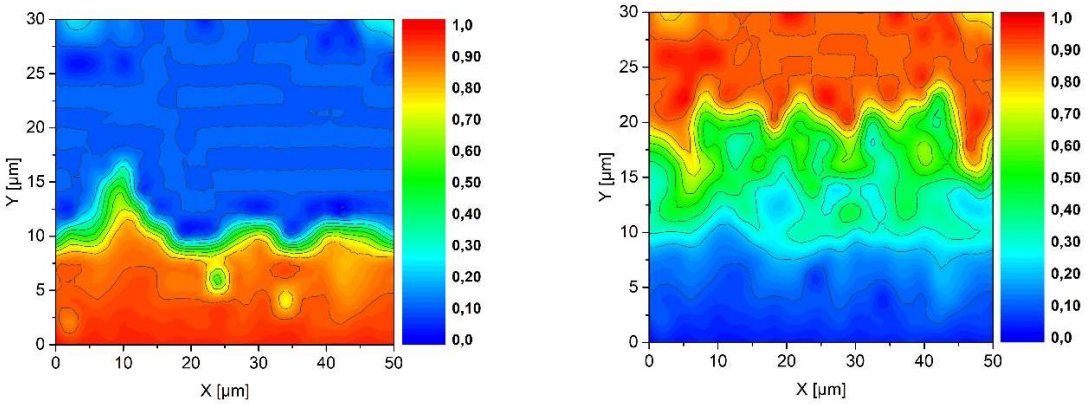

FIG. 5. 30 THE RAMAN MAP IMAGES OF SAMPLE S-3- WITH THE FLUENCE OF 10^{16} IONS/CM^2.

Creating a surface Raman map involves selecting a field of the p-TRISO sample that includes all the layers that the S-3 p-TRISO sample is made of. In a given field of 30x50 µm the Raman spectra were collected. During the measurement, Raman spectra were collected every 1 µm step. The goal of the measurement was to obtain a large amount of data from the selected field. As it is presented on Fig. 5. 28, Fig. 5. 29, and Fig. 5. 30 the level of 15 µm is in the middle of the selected field, which represents the Buffer-IPyC interface (junction). Analyzing each map separately, it should be understandable that the red color represents 100% of the concentration of analyzed layer in the measured field. Due to that, in the non-implanted S-3 p-TRISO sample the Buffer- IPyC interface was in the middle of the selected field. But with the increasing fluence the Buffer-IPyC interface start to change its position. What is observed on the maps is the mixing of the two Buffer and IPyC causing the formation of a transitional interlayer. The fluence that creates this interlayer reflects only several months of hypothetical TRISO neutron irradiation in the reactor core. It shows that the ion implantation process induces the amorphization process in the structure, because the irradiated area gradually loses its crystallinity.

Additional results based on Tab. 5. 5, Tab. 5. 6, Tab. 5. 7, and Tab. 5. 8 in the form of the Raman maps are shown in Fig. 5. 31. The obtained Raman maps for G- and D-band position and width, as well as for the intensity ratio ID/IG, presents also the Buffer layer on the bottom, and IPyC layer on the top of the analyzed measurements field. At a fluence of 10^{14} ions/cm^2, an increase in the intensity of the D-band is noticeable, which is related to the formation of damage. With an increased fluence, we observe a mixing of dislocations in both coating layers, which confirms the effect of amorphization of the structure. To confirm that the p-TRISO samples start to damage, the SEM analysis was performed.

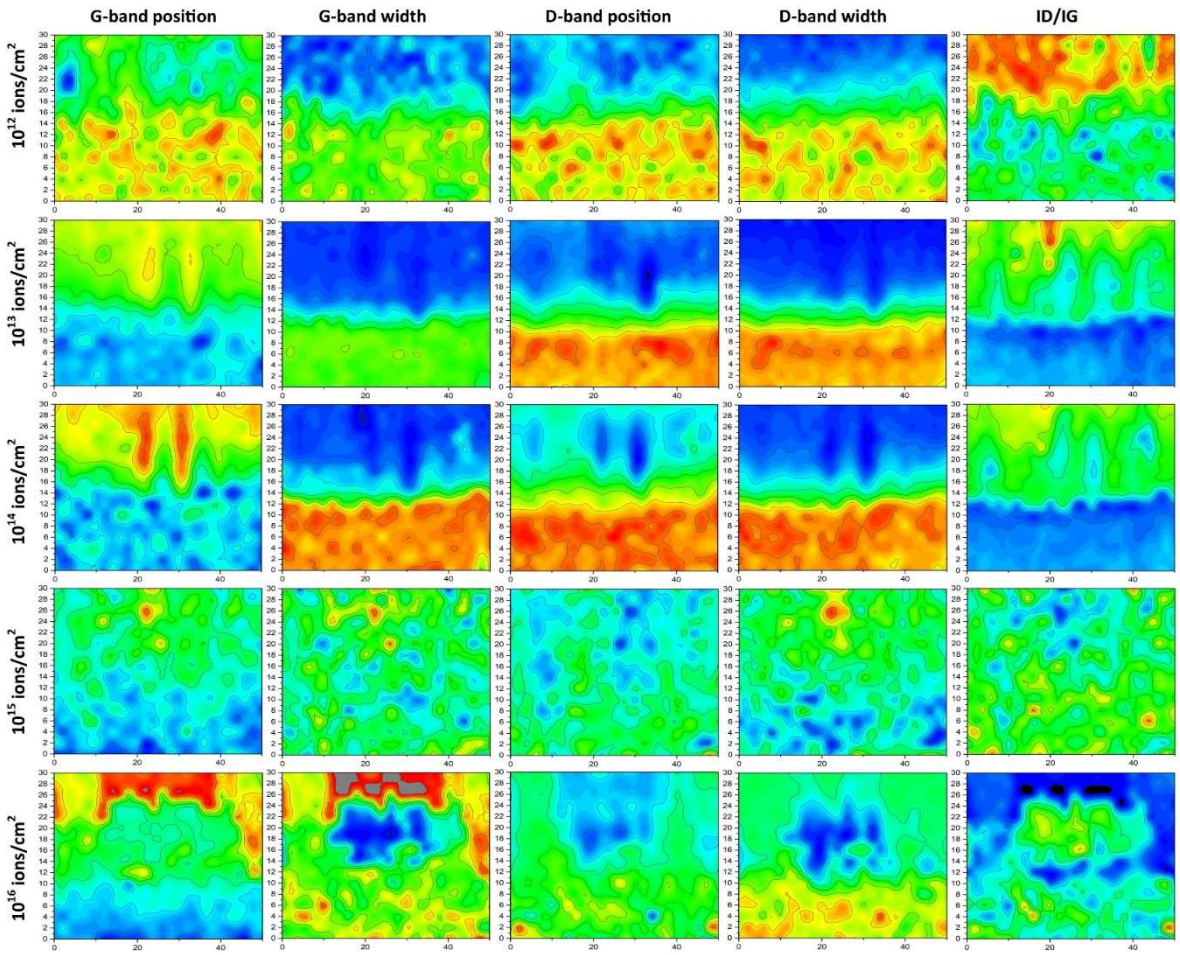

FIG. 5. 31 G-BAND AND D-BAND CHANGES DUE TO THE INCREASING FLUENCE.

During ion irradiation, several carbon atoms are displaced, causing defects along the basal planes as well as between the basal planes. Also, some of these carbon atoms lose their original sp^2 bond and form a new sp^3 bond. The increase of the ion fluence causes an increase in defects along and between basal planes, and an increase in formation of sp^3 clusters. Graphite-like layers gradually lose their ordering, causing a significant reduction in the degree of preferred orientation of pyrocarbon layers, and then the PyC surface layer becomes amorphous. The annealing of PyC after ion implantation can repair the structure to its original form only for slightly damaged PyC samples, which is confirmed by Raman spectra analysis. Similar SEM effects on the Buffer and IPyC layers are observable in Ref. [171].

The SEM measurements were performed on the S-1, S-2, and S-3 p-TRISO samples, for the non-implanted samples as shown at Fig. 5. 32, Fig. 5. 33, Fig. 5. 34, and those implanted with the fluence equal 10^{14} ions/cm^2 illustrated at Fig. 5. 35, Fig. 5. 36, Fig. 5. 37, and 10^{16} ions/cm^2 at Fig. 5. 38, Fig. 5. 39, and Fig. 5. 40. The increase in the irradiation fluence leads to the embrittlement processes of the near-surface layer, which can cause structural distortions.

Radiation damage leads to the formation of microcracks and pores, which results in decrease in both the strength and radiation damage resistance of the analyzed structure [169]. Increasing the implantation fluence to 10^{16} ions/cm^2 causes the volumes of damaged areas to increase to such level, that at some point they begin to overlap, filling the entire implanted layer quite uniformly, which can lead to amorphization. In addition, as the fluence increased for each p-TRISO sample, an increase in pore size and amount of porosity was observed in the Buffer layer. However, the IPyC layer had a uniform laminar structure with almost no visible porosity. During implantation, the volume of the Buffer layers decreased, and there was a decrease in the content of graphitic sp^2 compounds in the analyzed structure.

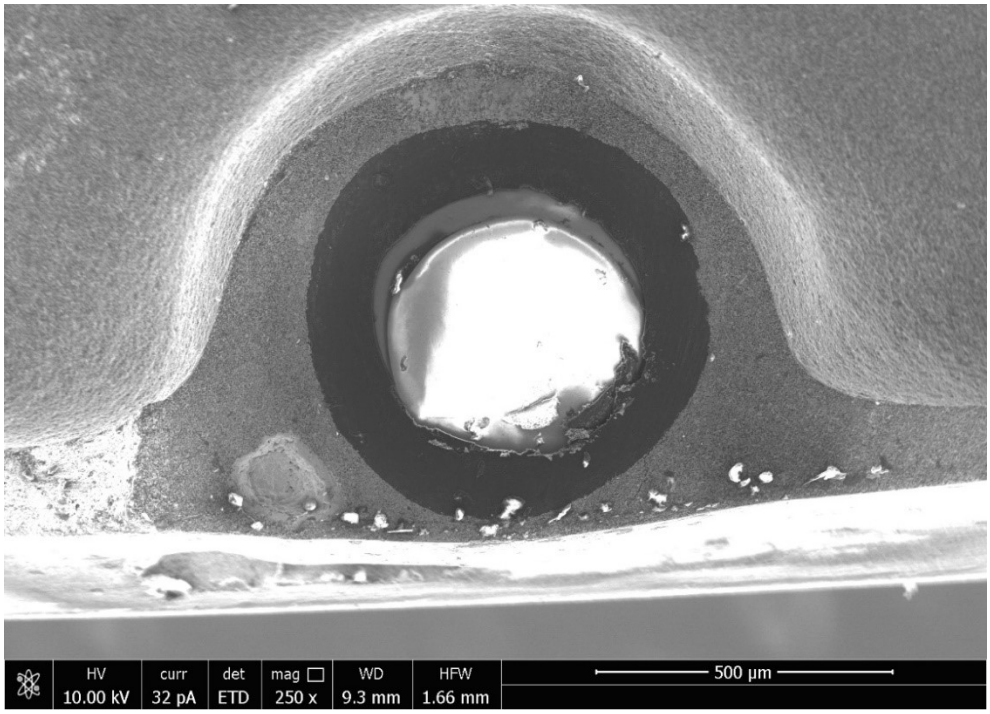

FIG. 5. 32 NON-IMPLANTED BUFFER LAYER.

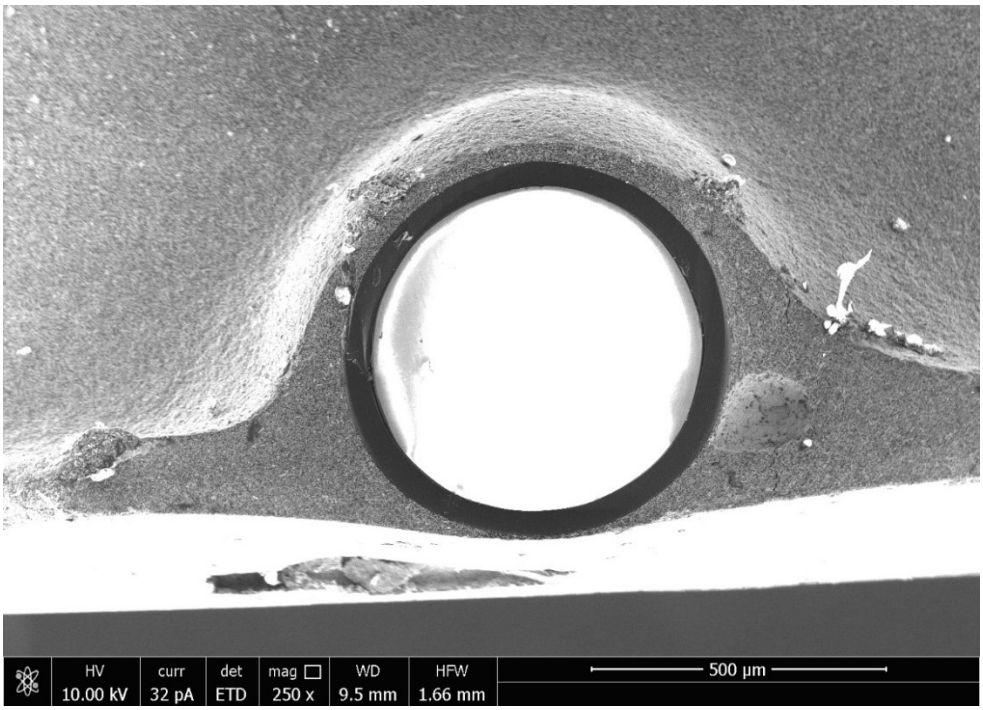

FIG. 5. 33 NON-IMPLANTED IPYC LAYER.

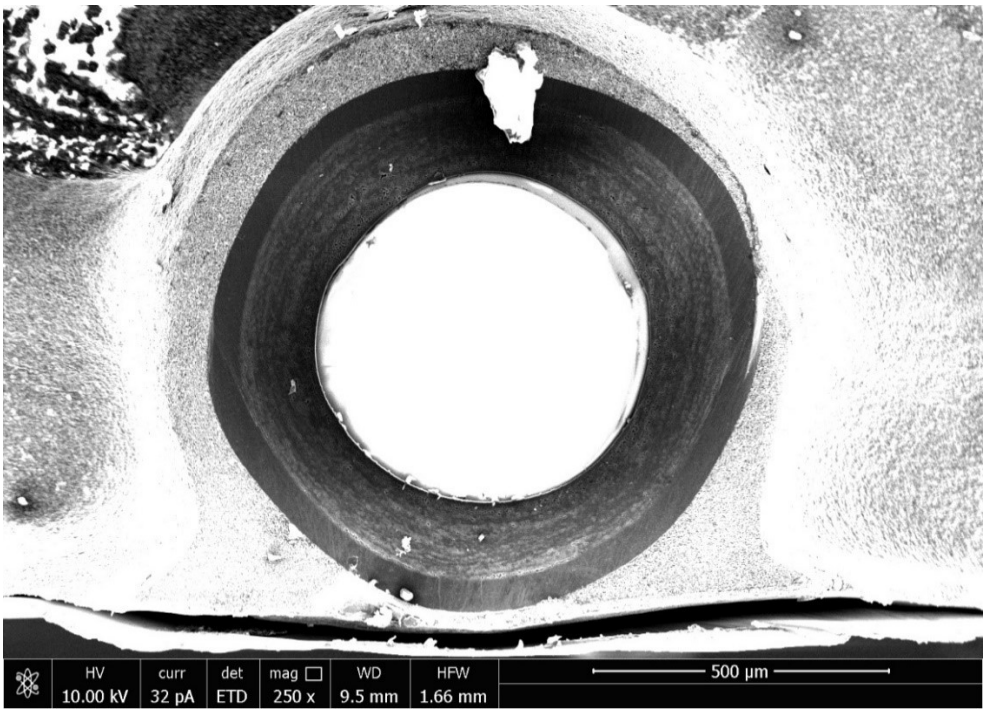

FIG. 5. 34 NON-IMPLANTED BUFFER+IPYC LAYRS.

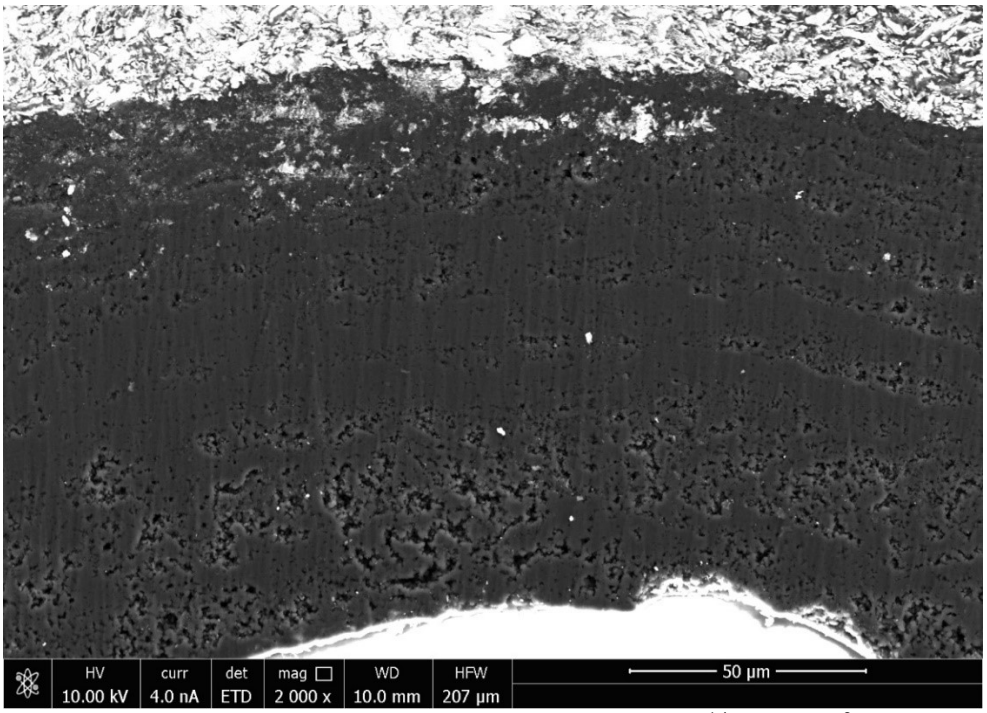

FIG. 5. 35 BUFFER LAYER IMPLANTED WITH 10^{14} IONS/CM^2.

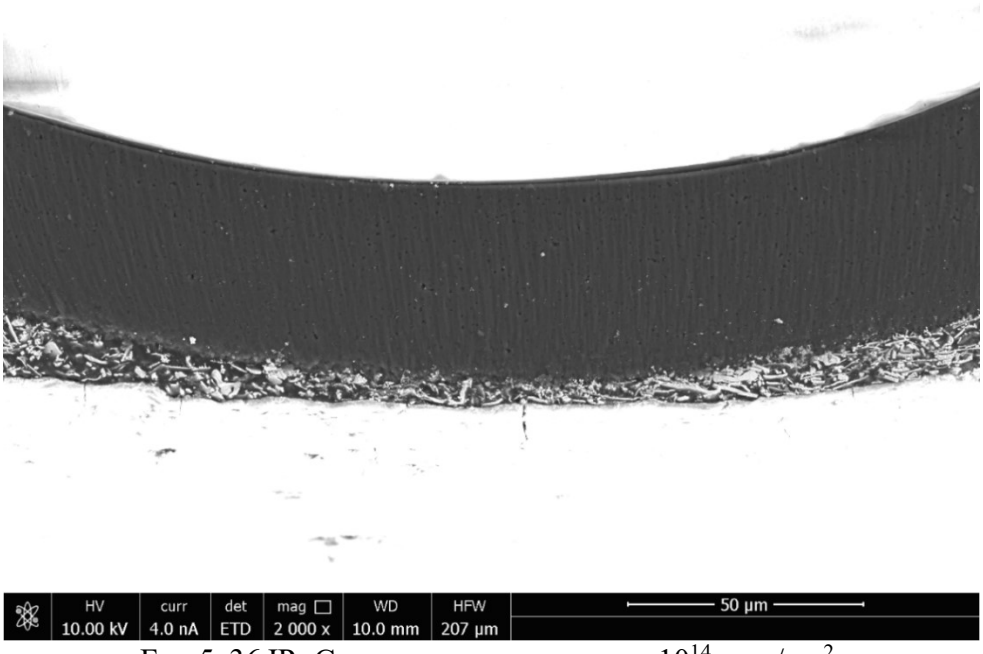

FIG. 5. 36 IPYC LAYER IMPLANTED WITH 10^{14} IONS/CM^2.

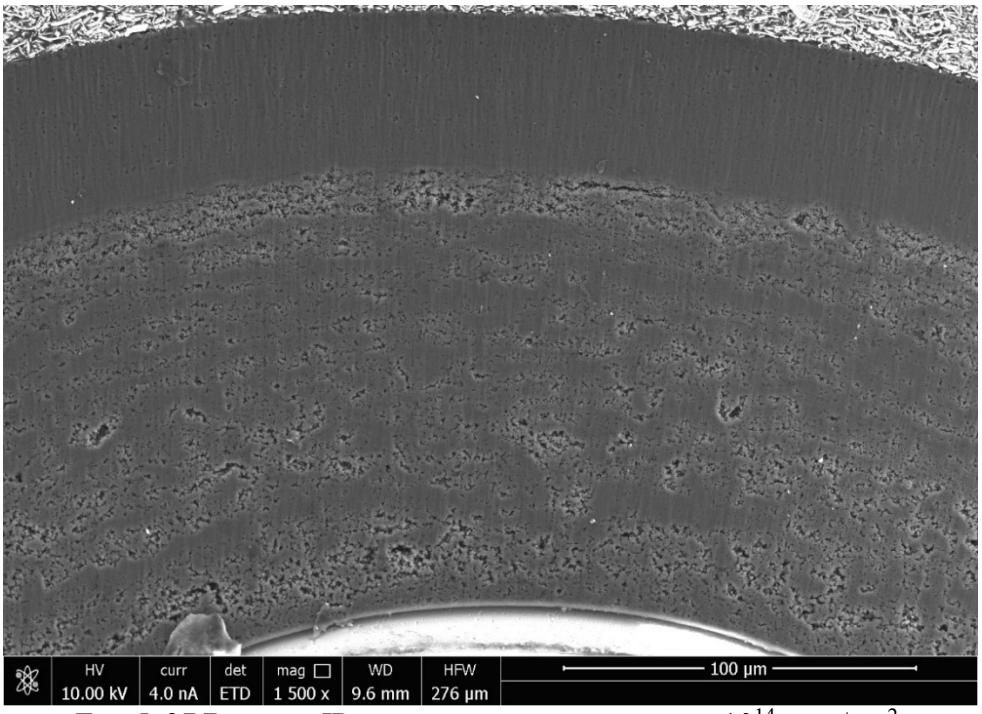

FIG. 5. 37 BUFFER+IPYC LAYERS IMPLANTED WITH 10^{14} IONS/CM^2.

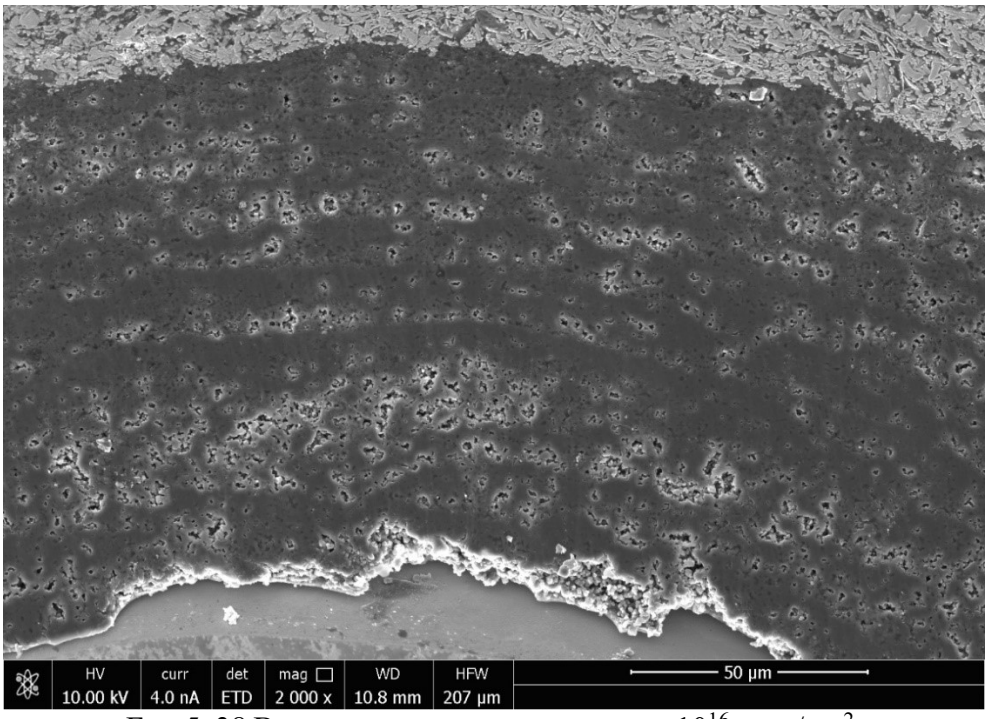

FIG. 5. 38 BUFFER LAYER IMPLANTED WITH 10^{16} IONS/CM^2.

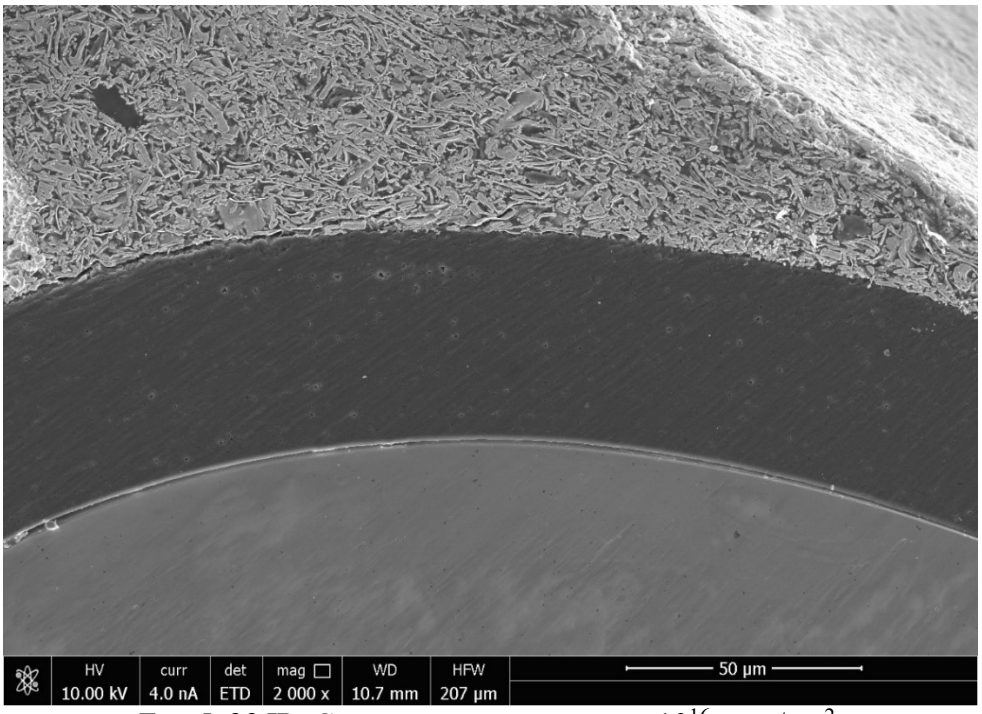

FIG. 5. 39 IPYC LAYER IMPLANTED WITH 10^{16} IONS/CM^2.

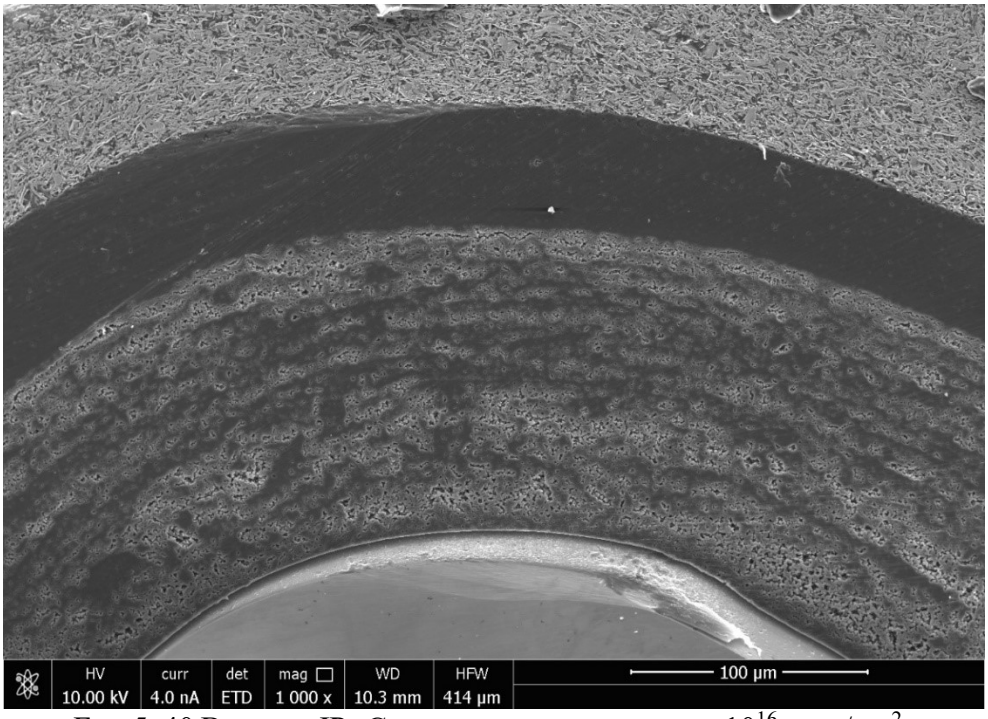

FIG. 5. 40 BUFFER+IPYC LAYERS IMPLANTED WITH 10^{16} IONS/CM^2 .

An additional parameter that determines structural changes is the L_a parameter. The L_a parameter was used to measure the crystallite size of the analyzed surface. This parameter was calculated due to the formula (1) presented in Ref. [139][172][173][174][175].

$$L_a\,[nm] = (2{,}4 * 10^{-10})\,\lambda_{laser}^4\,(\frac{I_D}{I_G})^{-1} \tag{5}$$

where, the wavelength λ_{laser} was set to 785 nm, and the values of the intensity ratio *ID/IG* were taken from Tab. 5. 5, Tab. 5. 6, Tab. 5. 7, and Tab. 5. 8. It should be noted that the value of L_a parameter depends on the laser wavelength, therefore the ratio of the intensity ratio ID/IG in the Raman spectrum is much higher for the applied in this experiment wavelength. Consequently, the obtained values are only for the comparison of the p-TRISO samples [160][176].

Tab. 5. 9 shows that the L_a parameter calculated for each p-TRISO sample decrease with the increase of the fluence. This behavior is observed until the formation of the D''-band. Then, with the fluence of 10^{16} ions/cm^2, the values of the L_a parameter start to grow for each case of the analyzed layer. As mentioned, the increase in the value of the L_a parameter may be due to the phenomenon of returning the knocked-on atoms to their positions, in which case the impression of repairing the damaged structure is formed.

TAB. 5. 9 THE CRYSTALLITE SIZE OF P-TRISO COVERING LAYERS

L_a [nm]	*before implantation*	*$1*10^{12}$ [ions/cm^2]*	*$1*10^{13}$ [ions/cm^2]*	*$1*10^{14}$ [ions/cm^2]*	*$1*10^{15}$ [ions/cm^2]*	*$1*10^{16}$ [ions/cm^2]*
S-1 (Buffer)	55.87	52.95	44.93	42.19	18.68	20.69
S-3 (Buffer)	53.95	54.86	50.95	46.75	14.16	31.53
S-3 (IPyC)	57.32	51.77	48.2	43.56	27.80	33.88
S-2 (IPyC)	43.56	43.56	43.02	36.55	18.50	21.44

Due to the polishing procedure or during the implantation process or even the measurements with other devices, contamination of the sample may have occurred. Fig. 5. 41 shows silver contamination that is present in the Buffer layer, as well as mechanical damage to the adhesive layer. The resulting contamination does not affect the experimental results, because only a 30μm×50μm region was selected for Raman measurements.

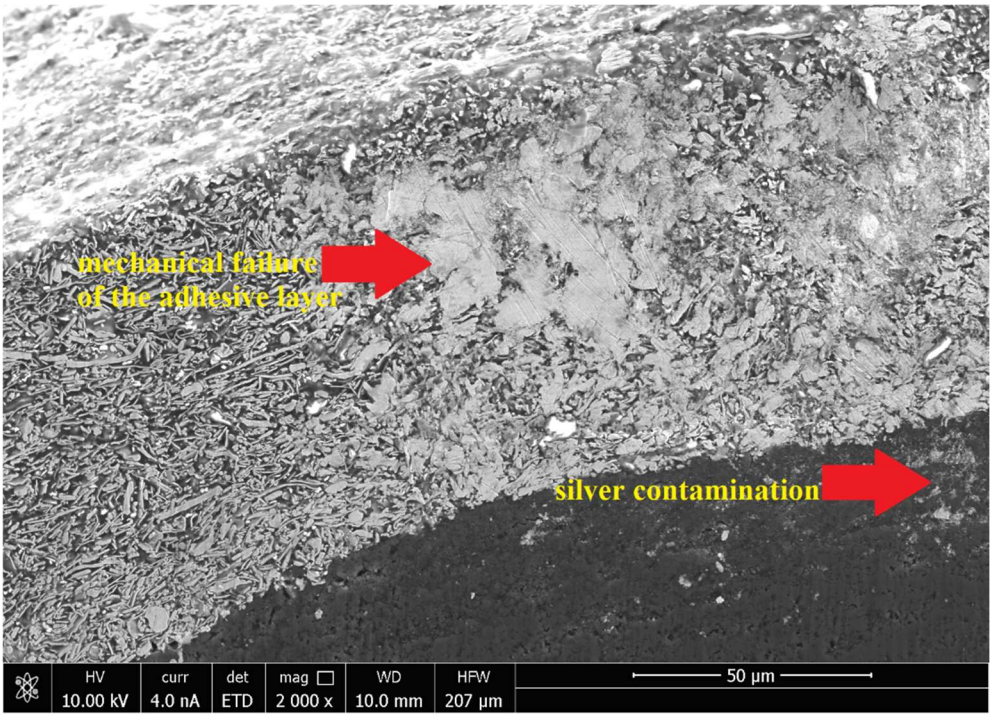

FIG. 5. 41 MECHANICAL FAILURE OF THE ADHESIVE LAYER AND SILVER CONTAMINATION.

Based on the performed experiment it was possible to observe the changes that occurred in the individual layers of each p-TRISO sample. The obtained results show that the primary damage in the Buffer and IPyC layers start to occur with an ion fluence equal to $1*10^{14}$ ions/cm^2. This primary fluence creates an interlayer that appears at the Buffer-IPyC interface, which may lead to create the gap between these layers at the further stage of irradiation. Analysing each layer separately, it was possible to understand the appearance of structural dislocations at the interface of the Buffer-IPyC layers.

5.2.3. EXPERIMENT ON THE S-3 P-TRISO SAMPLE

This part of the experiment focuses on the verification of the level of damage that might occur to the p-TRISO covering layers structure after 1st and 5th year of ion irradiation. The reason for choosing such a fluence is that the recirculation of the fuel in HTGRs takes 3 to 5 years in general. The calculations for ion fluences were performed with the use of the SRIM and TRIM programs. Based on the calculations, 1 year of neutron irradiation reflects an ion fluence equal to $3.8*10^{16}$ ions/cm^2 of Ne^+ ions, and 5 years of neutron irradiation reflects an ion fluence equal to $1.9*10^{17}$ ions/cm^2 of Ne^+ ions. The experiment was performed on the six S-3 type p-TRISO-particles, enabling statistical analysis on the obtained results. Detailed explanation is presented in Ref. [145]. This experiment was conducted in several steps:

- Polishing the sample with ion-polishing method;
- Raman spectroscopy measurement on the polished intact surface;

- Ne^+ ion irradiation with a fluence equal $3.8*10^{16}$ ions/cm^2 – 1 year of neutron irradiation;
- Raman spectroscopy and SEM measurement;
- Ne^+ ion re-irradiation up to the fluence equal $1.9*10^{17}$ ions/cm^2 – 5 years of neutron irradiation;
- Raman spectroscopy and SEM measurement.

Fig. 5. 42 and Fig. 5. 43 describes the average Raman spectra obtained for Buffer and IPyC layers of six S-3 p-TRISO-particles. The layer structure of both covering p-TRISO layers changed during the implantation procedure. It is observed, that due to the irradiation from two G-and D-bands, only one Raman band was created, which is due to the fact that the dislocation process starts to occur at the investigated layers. Comparing the changes that occur because of the increase of the fluence, it can be noted that for the Buffer layer, the change in the Raman spectra is more significant than for IPyC layer. This is due to the greater difference in the ID/IG ratio for the unmodified structure of the Buffer layer. In addition, analyzing the spectrum obtained for the Buffer layer after 1 year of irradiation, a merging of D- and G- bands in the single D'' band, is more visible than in the IPyC layer. Finally, in both cases of layers, the difference in the obtained spectra after 1 and 5 years of irradiation is negligible.

Tab. 5. 10, and Tab. 5. 11 presents the data obtained from the Raman spectra, such the position of D-, and G- bands, the width of the D-, and G-bands, and the intensity ratio of the D-Raman band and G-Raman band (ID/IG), as well as the area of ID/IG. As it can be noticed, in the case of Buffer and IPyC layers, the D-band position increase with the increasing fluence, which is reversed in the case of the G-band position. In both layers the D-band and G-band width increased with the increasing fluence, which results in the creation of one Raman - D'' band. The ratio of intensities, of the disorder-induced D- band and the first-order graphite G- band (ID/IG), is crucial to estimate the structural disorder. In both examined layers, one can observe that the intensity ratio ID/IG increases with the time of sample ion irradiation. Additional results based on Tab. 5. 10 and Tab. 5. 11 in the form of the Raman maps are shown in Fig. 5. 44. In the comparison to the previous Raman map results, it is noticeable that with increasing fluence the Buffer becomes more damaged than the IPyC layer.

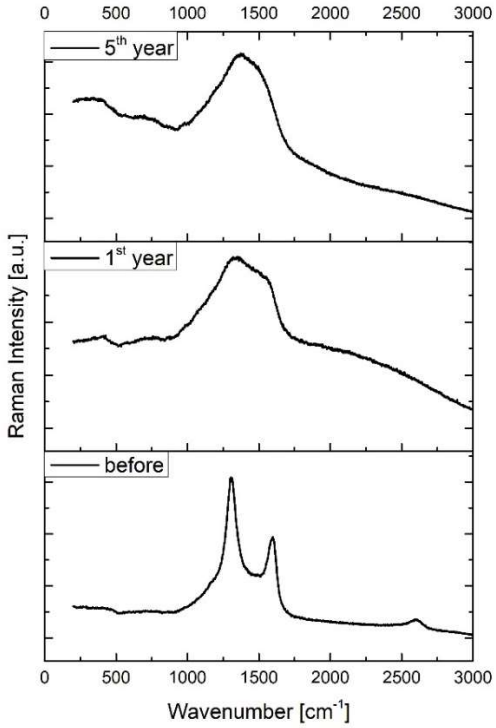

FIG. 5. 42 THE RAMAN SPECTRA OF THE BUFFER LAYER OF THE S-3 P-TRISO SAMPLE FOR DIFFERENT ION FLUENCES.

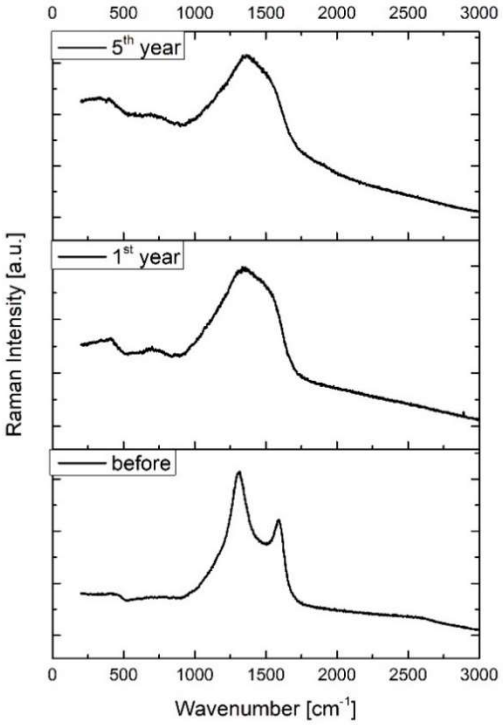

FIG. 5. 43 THE RAMAN SPECTRA OF THE IPYC LAYER OF THE S-3 P-TRISO SAMPLE FOR DIFFERENT ION FLUENCES.

TAB. 5. 10 PARAMETERS OBTAINED FOR THE BUFFER LAYER OF SAMPLE S-3

Fluence	*Position*		*Width*		*ID/IG*	*ID/IG area*
	D- band	**G-band**	**D- band**	**G-band**		
before implantation	1309± 0.4	1583.8±1.1	140.5±3.1	106±2.3	1.69±0.03	2.05±0.03
1st year of irradiation	1348.7±7.1	1551.7±12.6	461.8±26.9	133.8±19.6	3.85±0.58	18.38±5.0
5th year of irradiation	1373.3±5.4	1537.7±3.6	432.4±16.1	153.9±10.5	4.85±0.77	18.74±5.44

TAB. 5. 11 PARAMETERS OBTAINED FOR THE IPYC LAYER OF SAMPLE S-3

Fluence	*Position*		*Width*		*ID/IG*	*ID/IG area*
	D- band	**G-band**	**D- band**	**G-band**		
before implantation	1315.6± 1.5	1578.2±0.6	243.3±3.2	129±2.5	1.56±0.06	3.34±0.25
1st year of irradiation	1332.2±8.6	1529.4±8.2	426.5±24.8	177.6±16.2	2.85±0.56	9.05±3.9
5th year of irradiation	1371.7±5.5	1544.9±4.5	441.0±18.6	147.1±14.1	5.29±0.98	21.91±8.0

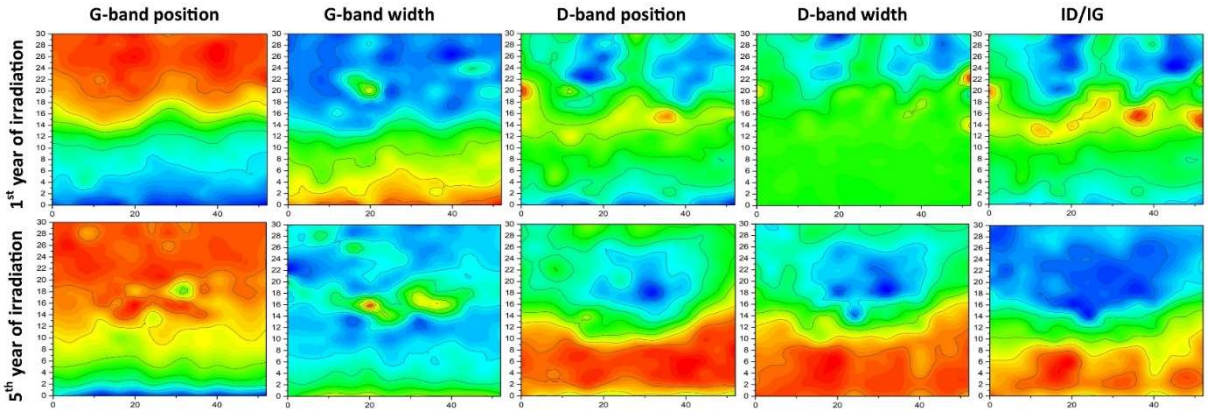

FIG. 5. 44 G-BAND AND D-BAND CHANGES DUE TO THE INCREASING FLUENCE.

As mentioned in the previous section, it is possible to observe that over a period of time the pyrolytic carbon structure begins to repair itself to its original form. This is due to the increase in the width parameter of the D-band, at a fluence corresponding to 5 years of irradiation, observed for both p-TRISO layers. Nevertheless, by analyzing the averaged values collected from measurements on the six p-TRISO samples, as the fluence (irradiation) increases, damage occurs in the analyzed layers. As confirmation, results are presented in Tab. 5. 12, showing the decreasing size of crystallites (L_a parameter) with increasing fluence.

TAB. 5. 12 THE CRYSTALLITE SIZE OF P-TRISO COVERING LAYERS

L_a [nm]	*before implantation*	*3.8*10^{16} [ions/cm^2]*	*1.9*10^{17} [ions/cm^2]*
S-3 (Buffer)	53.80	23.71	18.78
S-3 (IPyC)	58.37	31.92	16.42

In addition, the Raman maps were measured to illustrate the changes taking place at the interface of the Buffer-IPyC layers. The Raman surface maps are shown in Fig. 5. 45, Fig. 5. 46, and Fig. 5. 47. The figures present the results obtained for the average over six S-3 p-TRISO-particles. Those maps are divided according to the time of implantation, namely: before irradiation, 1st year of neutron irradiation, and 5th year of neutron irradiation. The Raman maps were obtained with the same procedure as is explained in Chapter 5.2.2. The maps on the left side represent the Buffer layer, while the maps on the right side the IPyC layer. With increasing fluence of ion irradiation, which reflect the time of neutron irradiation, the Buffer-IPyC interface was shifted from 15 μm to the level of 8 μm. This behavior indicates significant damage at the interface of the Buffer – IPyC layers.

The Buffer layer might become completely detached, or partially debonded from the IPyC layer, forming a gap. The width of the gap changes during the irradiation because the Buffer densifies with increasing neutron fast fluence while the kernel swells with increasing burn-up. At the beginning of irradiation, the combined shrinkage of the Buffer and IPyC creates a gap between these two layers. The gap thickness is controlled by the swelling of the kernel on one side, and by the Buffer and IPyC shrinkage/swelling on the other side. Consequently, if the swelling rate of the kernel exceeds the shrinking rate of the Buffer and IPyC, or if the Buffer and/or IPyC begin to swell, the Buffer-IPyC gap may close during irradiation [84][85].

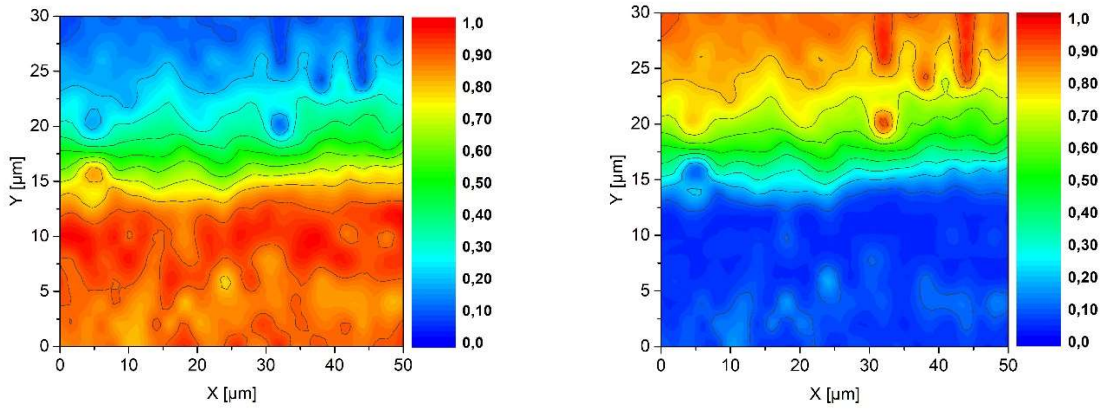

FIG. 5. 45 THE RAMAN MAP IMAGES OF SAMPLE S-3 – NON-IMPLANTED.

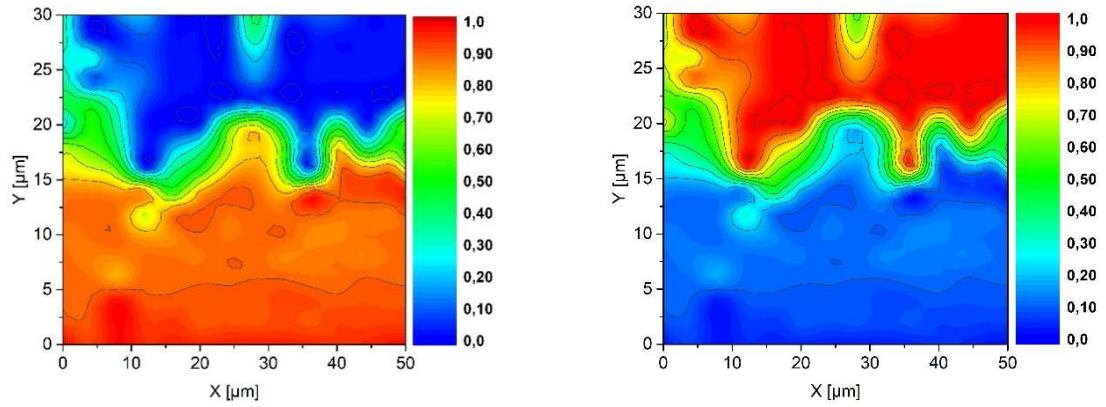

FIG. 5. 46 THE RAMAN MAP IMAGES OF SAMPLE S-3 - 1 YEAR.

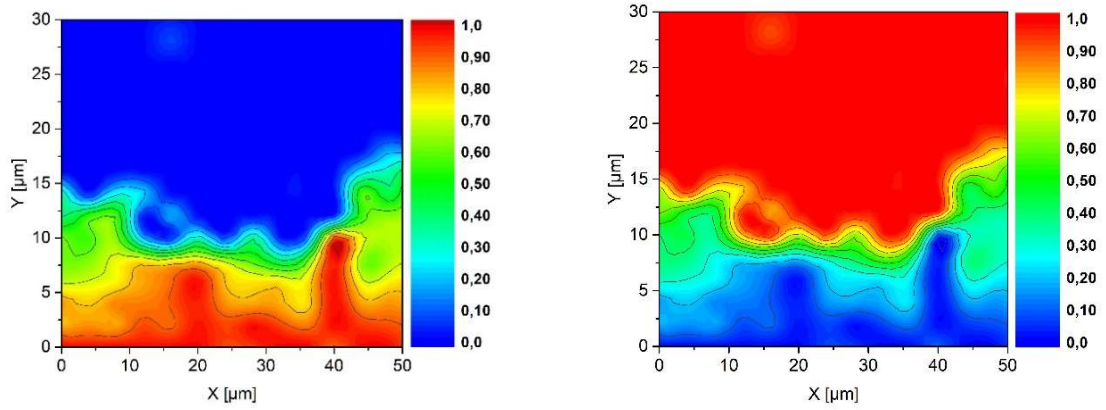

FIG. 5. 47 THE RAMAN MAP IMAGES OF SAMPLE S-3 - 5 YEARS.

To illustrate the structural changes that took place, SEM was used. The SEM images presented in Fig.5. 48, Fig. 5. 49, and Fig. 5. 50 that were obtained for S-3 p-TRISO shows that with increasing implantation fluence the structure of each layer becomes more damaged. It can be noticed, that the microstructure of the low-density porous pyrocarbon Buffer layer becomes globular, which is represented as the formation of circles. The microstructure of high density

isotropic IPyC layer becomes more conical, which is represented as the formation of cones. The difference in the microstructure of both layers is due to the difference in the density of the analyzed layers. The Buffer density is equal 0.97 g/cm^3, when the IPyC density is equal 1.84 g/cm^3.

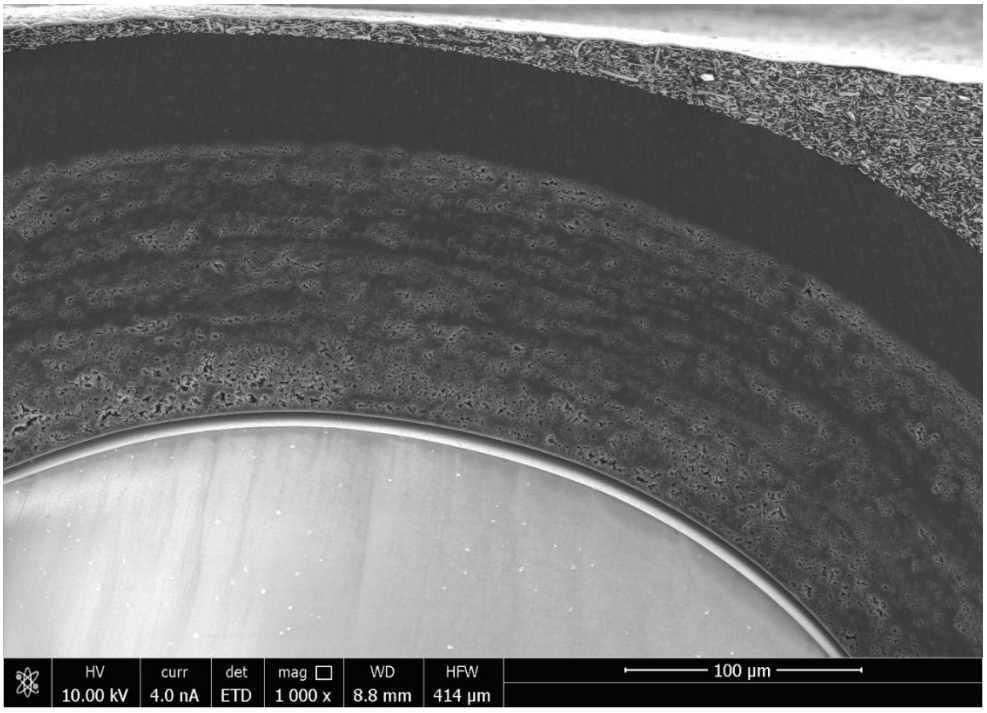

FIG.5. 48 BUFFER+IPYC LAYERS - BEFORE IRRADIATION.

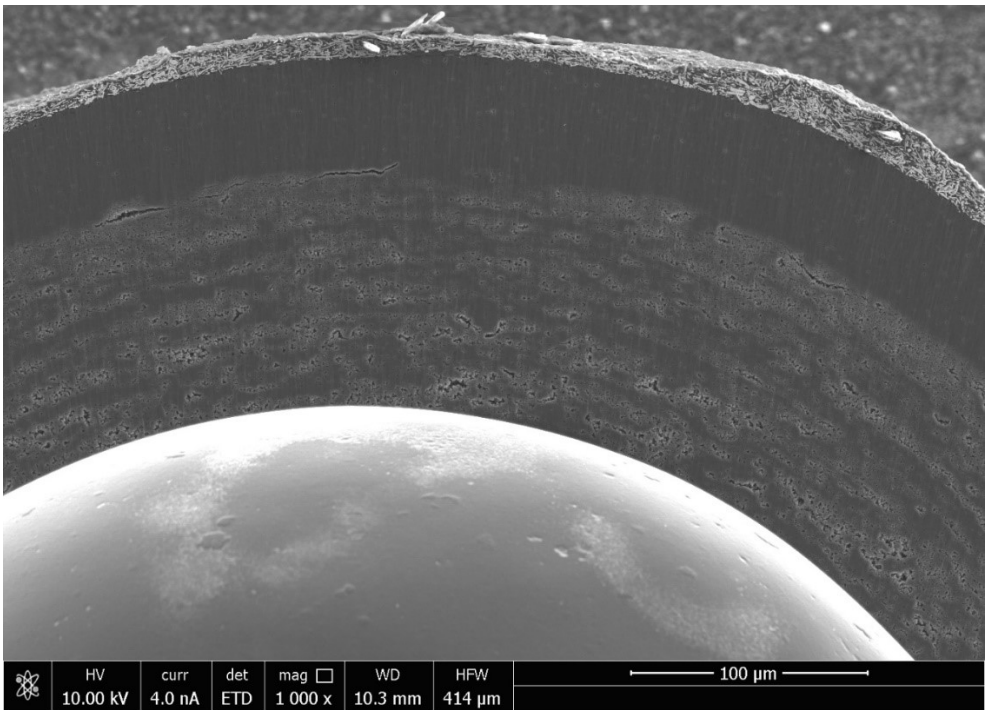

FIG. 5. 49 BUFFER+IPYC LAYERS - 1 YEAR.

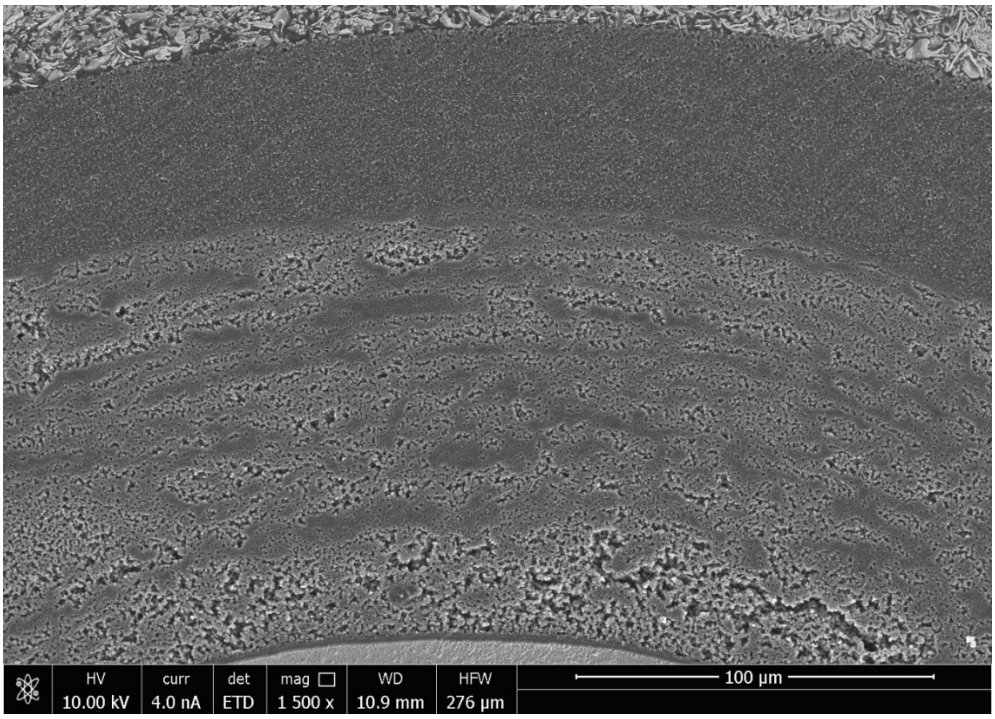

FIG. 5. 50 BUFFER+IPYC LAYERS - 5 YEARS.

Fig. 5. 51 present the magnification of the Buffer- IPyC interface. The high-density IPyC layer (top) has more laminar structure then the low-density Buffer layer (bottom) which represent the globular features [177]. The laminar structures tend to resemble the structure of graphite, which is due to the reordering of the structure, that the base planes become more parallel and closer to each other.

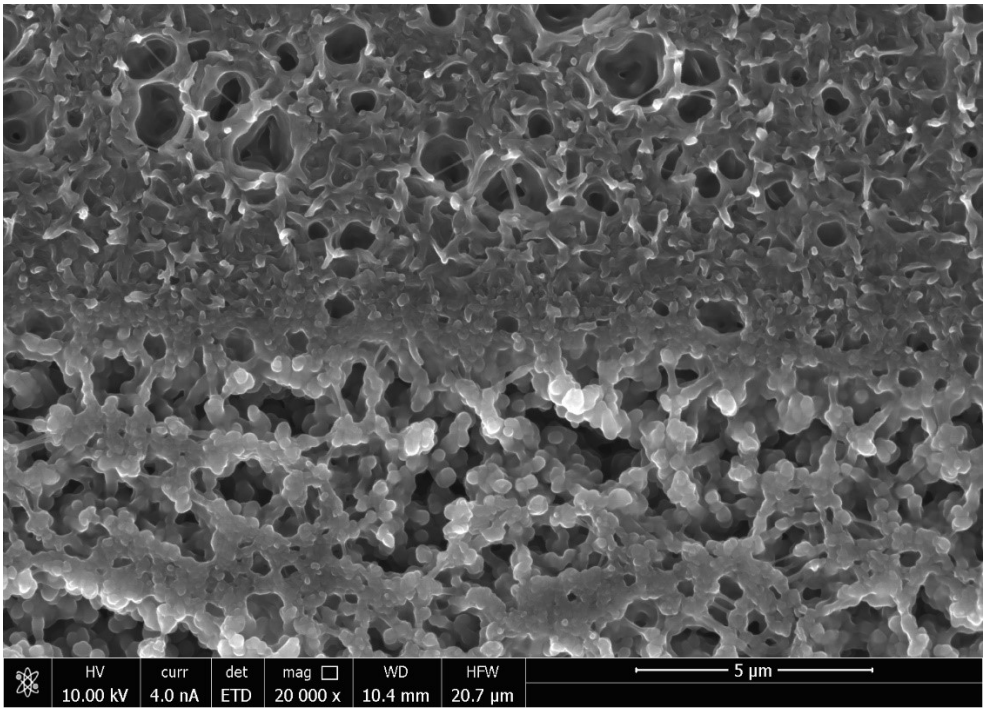

FIG. 5. 51 BUFFER-IPYC INTERFACE MAGNIFICATION.

The purpose of this experiment was to irradiate several S-3 p-TRISO samples, with ion fluences that reflect 1 and 5 years of the neutron irradiation, and to verify the irradiation effects on the Buffer-IPyC interface.

5.2.4 Experiment on non-polished p-TRISO sample

To be able to consider the ion irradiation method as a fast screening tool for newly produced or stored but unirradiated TRISO-particles, the p-TRISO samples that had not been polished were used in this experiment. Two p-TRISO-particles were chosen for this experiment. One sample was irradiated with the Ne^+ ions, when the second samples with He^+ ions. Detailed explanation is presented in the Ref. [145]. This experiment was conducted in several steps:

- Raman spectroscopy measurement on the outer surface of p-TRISO sample;
- Ne^+ and He^+ ion irradiation with a fluence that reflect 3 years of neutron irradiation;
- Raman spectroscopy and SEM measurements on the outer surface;
- polishing the samples with ion polishing method;
- Raman spectroscopy and SEM measurements on the samples cross-sections.

The ion irradiation, as well as the Raman spectroscopy and SEM measurements were performed on the p-TRISO spheres in such a way that the beam fell on the outer surface of the sample, in this case on the IPyC layer. The ion implantation on a curved surface can cause uneven implantation as a function of position. Nevertheless, the sample area analyzed under the Raman spectroscope is small enough that the above aspect is negligible. Fig. 5. 52 shows the outer surface of the p-TRISO-particle.

The experiment on non-polished samples was performed with an energy of 160 keV, and a fluence of $1.1*10^{17}$ ions/cm^2 for Ne^+ ions, and a fluence of $1.05*10^{18}$ ions/cm^2 for He^+ ions. Both fluences reflects 3 years of neutron irradiation in the reactor core. After irradiation, the p-TRISO samples were measured with the use of Raman spectroscopy (Fig. 5. 55) and SEM (Fig. 5. 53) techniques. Then, these two samples were polished with the ion polishing method, obtaining the cross-section, on which Raman spectroscopy (Fig. 5. 56) and SEM (Fig. 5. 54) measurements were performed. The purpose of measuring the outside and inside layer of the p-TRISO samples is the necessity to verify whether ion irradiation can be performed on the sphere of the samples, without the need to polish it to obtain satisfactory results.

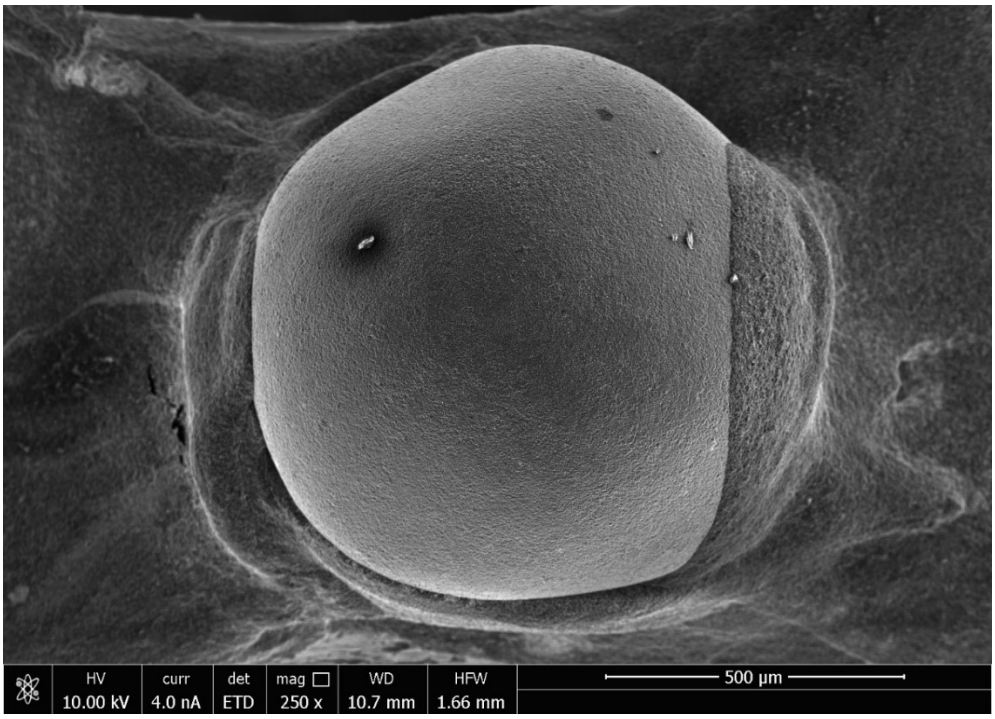

FIG. 5. 52 P-TRISO SAMPLE -SURFACE.

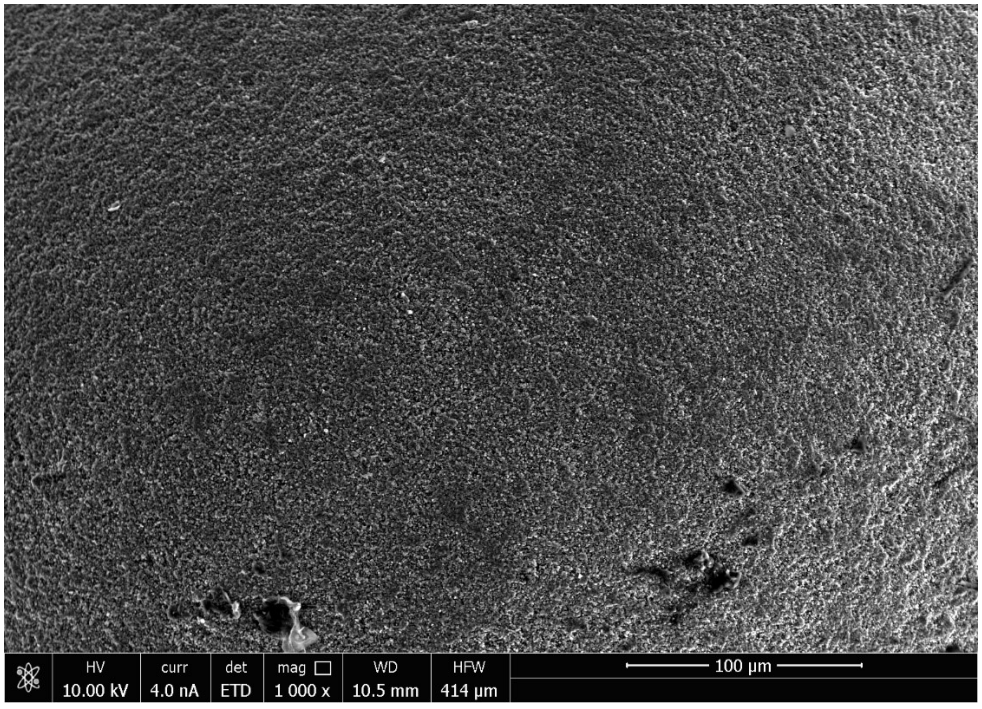

FIG. 5. 53 P-TRISO SAMPLE – SPHERE.

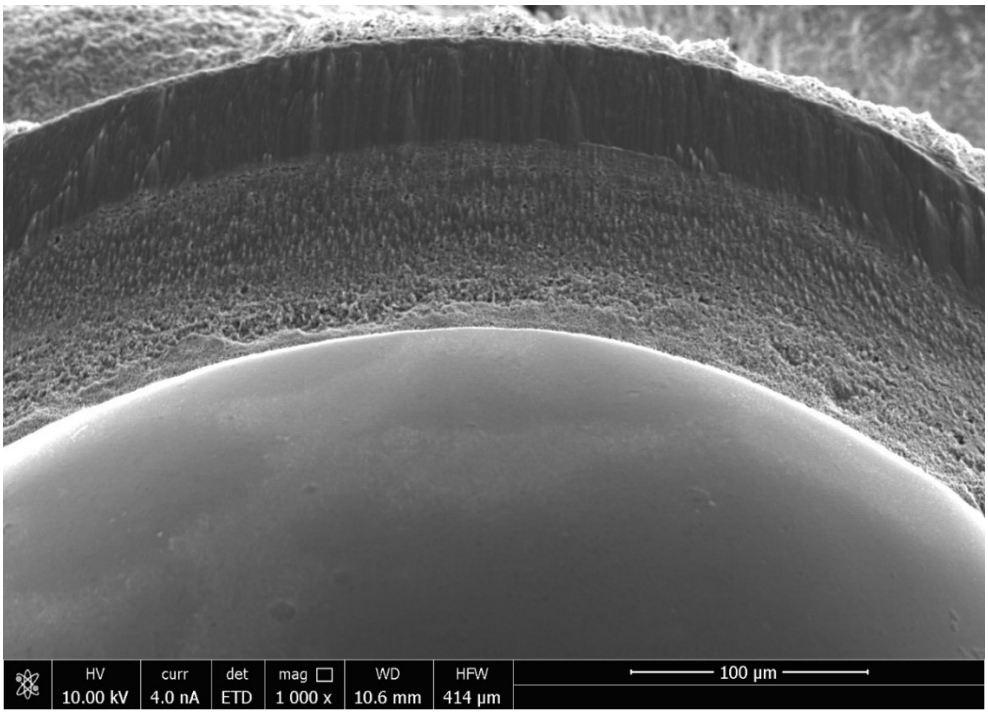

FIG. 5. 54 P-TRISO SAMPLE – CROSS-SECTION.

In this experiment the results are comparable to the ones obtained from previous experiments, described in this dissertation. As it was presented in the p-TRISO cases irradiated with fluences that reflects 1 and 5 years of neutron irradiation, the Raman spectra create only one D''- band. Fig. 5. 55 and Fig. 5. 56 shows that:

- regardless of the selected ion (Ne^+, He^+), the Raman spectrum obtained for an ion fluence equal to 3 years of neutron irradiation forms a single D''- band of similar shape;
- regardless of the place of measurement (outside, inside) of the p-TRISO-particle, the Raman spectrum obtained for an ion fluence equal to 3 years of neutron irradiation forms a single band of similar shape.

More detailed results obtained from Raman spectra are shown in Tab. 5. 13, and Tab. 5. 14. In both cases of analyzed ions (Ne^+, He^+), one can observe that the D-band position increases, when the G-band position decreases, which is related to the formation of disordered structure. For the rest of the selected parameters, it is observed that due to the 3 years of neutron irradiation the values of width for D-, and G-bands, as well as the intensity ratio of ID/IG increased over time.

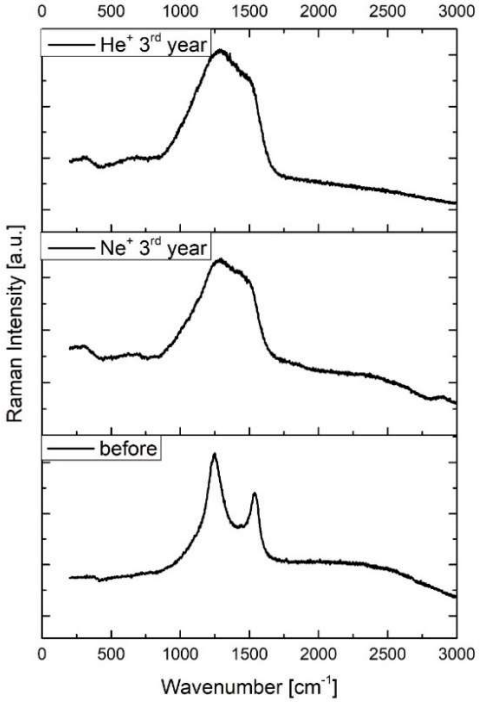

FIG. 5. 55 RAMAN SPECTRA OF THE S-3 P-TRISO SAMPLE FOR DIFFERENT ION FLUENCES – SPHERE.

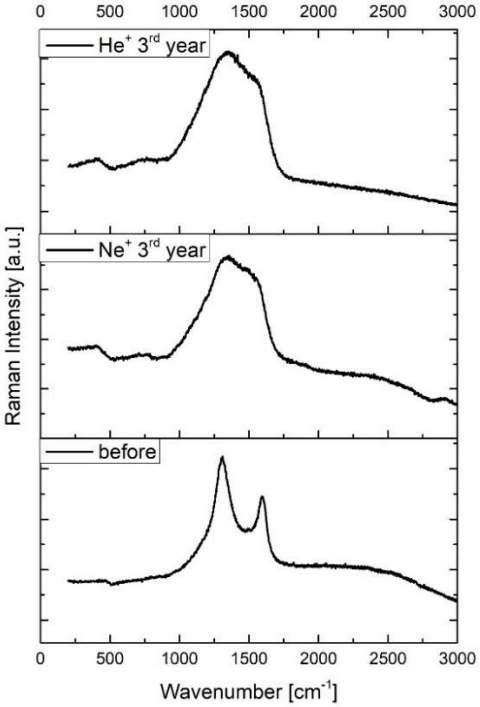

FIG. 5. 56 RAMAN SPECTRA OF THE S-3 P-TRISO SAMPLE FOR DIFFERENT ION FLUENCES – CROSS-SECTION.

TAB. 5. 13 NE^+ IMPLANTED P-TRISO SAMPLE

Fluence	*Position*		*Width*		*ID/IG*	*ID/IG area*
	D- band	**G-band**	**D- band**	**G-band**		
outer layer - before implantation	1309.9±1.7	1585.3±2.7	188.6±18.4	105.5±7.8	1.69±0.08	3.16±0.63
outer layer - 3rd year of Ne^+ irradiation	1332.5±3.7	1573±3.2	334.9±15.1	145.5±5.5	2.69±0.17	8.97±0.89
polished sample - 3rd year of Ne^+ irradiation	1347.2±10.4	1556.8±14.1	445.1±52.6	130.9±22.6	3.43±0.95	17.0±8.79

TAB. 5. 14 HE^+ IMPLANTED P-TRISO SAMPLE

Fluence	*Position*		*Width*		*ID/IG*	*ID/IG area*
	D- band	**G-band**	**D- band**	**G-band**		
outer layer -before implantation	1310.1±1.6	1585.7±2.9	188.6±18.2	105.9±7.9	1.69±0.1	3.15±0.67
outer layer - 3rd year of He^+ irradiation	1323.8±2.5	1578.3±2.2	332.8±22.6	129.7±11.1	2.64±0.19	9.59±1.73
polished sample - 3rd year of He^+ irradiation	1340.4±6.5	1567.6±4.5	483.6±45.7	137.2±12.8	3.7±0.82	17.39±6.95

The crystallite size (L_a) for the IPyC layer of the S-3 p-TRISO sample shows, like in previous calculations, that with increasing fluence the crystallite size decreases which is related to the amorphization process. Based on Tab. 5. 15, it can be noticed that the L_a parameter is lower for the measurements performed on the cross-section of the IPyC layer, than for ones obtained on the non-polished sphere of the S-3 p-TRISO-particle. At the same time, it is confirmed that the Ne-ion penetrate the IPyC layer more shallowly than the He^+ ions.

TAB. 5. 15 THE CRYSTALLITE SIZE OF P-TRISO COVERING LAYERS

L_a *[nm]*	*before implantation*	*sphere*	*cross-section*
$1.1*10^{17}$ ions/cm^2 for Ne^+	53.80	33.74	26.45
$1.05*10^{18}$ ions/cm^2 for He^+	53.80	34.66	24.62

In conclusion, in both presented situations (sphere vs cross-section) the same effect of detecting implantation-induced damage was obtained. It should be kept in mind that in this case only the IPyC layer was analyzed, as this is the outer layer of the p-TRISO sample. The performed ion irradiation with Ne^+ and He^+ ions, did not allow measurement of the Buffer layer. Because the depth of ion penetration not deep enough to reach the Buffer layer, the measurement on said layer would be unchanged, that is, it would be the same as for a non-irradiated Buffer layer. To determine the damage created in the Buffer layer on unpolished p-TRISO samples, it is necessary to increase the implantation energy, and thus to extend the depth of penetration of ions into the layer structures. This will make possible the quantification of the damage in both the IPyC layer and the Buffer layer. In addition, increasing the ion irradiation temperature will provide higher damage rates. Then it will be possible to meet the assumption that the ion irradiation can be performed on non-polished samples, and that ion implantation on the TRISO spheres is sufficient for the fuel fast screening method.

6. RESULTS

Operation of the HTGRs requires high-quality TRISO-particle fuel. Failure-free production of the TRISO fuel is a “condition sine qua non” for a good performance of HTGRs, aiming at minimal risk for release of radioactivity. Screening the TRISO-particle fuel for damage occurrence is a very important step to be completed before placing the fuel samples in the reactor core.

In particular, the following observations and conclusions are drawn from this dissertation:

- The key to the investigation of the research is the preparation of the sample for examination; and the selection of such a method that when it is used, causes no degradation of the material under examination. It was determined that of the two available methods, mechanical polishing and ionic polishing, it is optimal to use the ionic polishing method. As established from the experiments, mechanical polishing leads to damage, i.e. scratching the surface of the PyC layers. In addition, during the polishing process, the spreading of the polished material over the PyC surface occurs, leading to the clogging of pores in the Buffer layer. Both of these factors could falsify the measurement of the level of damage to PyC layers caused by ion implantation. An experiment using an ion polishing method confirmed that it does not cause damage to the TRISO covering layers, and does not interfere with the structure of the layers. It can, therefore, be assumed that the choice of ion polishing as a less invasive polishing technique provides better sample preparation for screening verification of TRISO fuel samples.
- To reflect the work in the reactor core, ion implantation was used. For this purpose, it was necessary to determine the ion fluence, which corresponds to the fluence of neutrons in the HTGR in terms of induced damage. Calculations were carried out using two different computer codes, SRIM/TRIM and MCB. Using these programs, it was possible to determine the DPA parameter, based on which the corresponding ion fluence needed for the ion irradiation experiment was determined. It was found that a fluence of $3.8*10^{16}$ ions/cm^2 corresponds to a neutron fluence of $1.6*10^{13}$ neutrons/cm^2 - in one year of constant irradiation (neutron flux equal to $5.02*10^{13}$ n/cm^{2}s). Furthermore, to determine the energy at which TRISO samples were implanted, additional experiments were conducted on graphite. Graphite, as a material similar to PyC, made it possible to determine that the implantation energy was equal to 160 keV. In addition, thanks to the implantation on graphite samples, the initial fluence with which p-TRISO samples were irradiated was determined.

- In the next step, the research was conducted on three p-TRISO samples called S-1 (Buffer), S-2 (IPyC), and S-3 (Buffer and IPyC). Samples of this type were implanted in several steps, with the final fluence not reflecting a year of neutron irradiation. The idea behind this study was to investigate how each of the individual layers changed under irradiation. In addition, it was also meant to find out what occurs at the interface between the Buffer - IPyC layers. The obtained results show that the primary damage in the Buffer and IPyC layers starts to occur with an ion fluence equal to $1*10^{14}$ ions/cm^2. This primary fluence creates an interlayer between the Buffer-IPyC interface, which may lead to creating a gap between those layers. Irradiation damage was analyzed using Raman spectra and maps, SEM images, and by calculating the size of crystallites using the L_a parameter. The results obtained from Raman maps for the position of the band and its width did not always clearly reflect the resulting changes in the analyzed structure. Nevertheless, a detailed analysis of the spectra supported by SEM imaging provided a good understanding of the amorphization occurring in each of the p-TRISO-particle coating layers.
- To reflect the damage caused by neutron irradiation over time, several S-3 p-TRISO samples were selected to be implanted with fluences corresponding to 1, 3, and 5 years of irradiation in the reactor core. As indicated by the results from Raman and SEM analysis, the formation of damage in the p-TRISO-coating layers is already evident after one year of implantation. The dislocation of the layers increases to a stage corresponding to the three years of irradiation of the samples, after which, at the end of the irradiation cycle (5 years), the damage formation process is stopped. The effect of structured damage formation in PyC layers is observable regardless of whether irradiation was carried out on polished or unpolished p-TRISO samples. In all analyzed cases, as the irradiation time of the samples increases, the Buffer-IPyC transitional layer is displaced, suggesting the formation of a Buffer – IPyC debonding. Based on the experiment it was possible to capture the point at which damage starts to occur to the individual layers, as well as to understand the appearance of damage at the interface of the Buffer-IPyC layers.

Based on performed experiments it can be concluded that ion irradiation serves as a surrogate for neutron damage irradiation. The research proves that for a fast screening method of produced but never used fuel or for a newly manufactured fuel, the ion implantation technique may be used to verify the quality of TRISO-particles before being placed the reactor core. It is important to note that analyzed p-TRISO-particles consist only of two coating layers (they lack

the most protective SiC layer) and are 22 years old. The experiment performed on p-TRISO samples confirmed that significant structural changes appear already after one year of ion irradiation of the samples. Significantly, with further time (i.e., after 3 and 5 years) of irradiation, no noticeable changes were observed in the p-TRISO-coating layers. The results of the experiment allow us to conclude that also the stored but unirradiated fuel can be effectively used as fuel in the reactor core. However, the results obtained in the mentioned scope should be compared with freshly manufactured TRISO samples within the occurrence of damage in the coating layers. Then the question of whether the damage in the TRISO sample layers is more progressive in "old" (stored, but unirradiated) fuel than in "new" (freshly manufactured) fuel could be answered. Such research, however, was not the subject of this dissertation, nevertheless, it should be undertaken in the future.

Further research on the uranium-kernel TRISO as well as on the surrogate p-TRISO-particles is needed to:

- simulate the damage in p-TRISO-particles with Molecular Dynamics, using the LAMMPS program – to better understand the ion irradiation-induced damages;
- improve the ion implantation experiment using higher energies and ions with a greater range of penetration into the analyzed structure – which will allow analyzing SiC and OPyC layers of the TRISO fuel;
- perform the ion implantation with the high temperature – that could better reflect damages that might happen in the HTGR;
- perform an irradiation experiment at the MARIA research reactor, which will require constructing an irradiation probe, performing the irradiation experiments, and conducting the PIE in the hot-cell lab;
- developing methods for reprocessing TRISO spent fuel for final disposal.

To conclude this dissertation, the similarity of the causes, subject matter, and nature of the p- TRISO fuel under study to the currently produced TRISO fuel (or fuel already produced but stored and non-irradiated) - as well as the possibility of applying the same procedures (when investigating damage) allows us to assume that a significant part of the conclusions drawn from this work are of a general nature, while the proposed proposals for the damage investigation procedure can be used in practice. Although the collected empirical material cannot be considered to be representative, the analysis of p- TRISO fuel damage made in the present work can provide a basis for certain generalizations, i.e. the dissertation confirms that:

- ion implantation mimics the process of neutron irradiation in the reactor core by radically shortening the time for inducing damages, and without the necessity to deal with activated material;
- diagnostic tools, i.e. Raman spectroscopy and SEM, allow to quickly and effectively detect the damage formation in the structure of the coating layers;
- the passage of irradiation time affects the level of damage to the coating p-TRISO layers.

7. LITERATURE

[1] Polish Nuclear Power Programme, Uchwała Rady Ministrów z 2/10/2020, Monitor Polski Dziennik Urzędowy Rzeczypospolitej Polskiej z 2020 poz. 964.

[2] Investigation Benefits and Challenges of Converting Retiring Coal Plants into Nuclear Plants, Nuclear Fuel Cycle and Supply Chain, INL/RPT-22-67964 (2022)

[3] A.H. Wells, L. Danese, Tri-Isotropic (TRISO) based Light Water Reactor fuel, United States Patent US8,774,344 B1 (2014).

[4] N.R. Brown, R. Hernandez, A.T. Nelson, High volume packing fraction TRISO-based fuel in Light Water Reactors, Progress in Nuclear Energy 146, p. 104151 (2022).

[5] J. Rosales, J.L. Francois, C. Garcia, Neutronic assessment of a PWR-type SMR core with TRISO particles using mixed-oxide fuel strategies, Progress in Nuclear Energy 154, 10440 (2022).

[6] P. Venneri, M. Eades, Space nuclear power and propulsion at USNC-Tech, Nuclear Technology 207, p. 876-881 (2021).

[7] https://x-energy.com/

[8] https://kairospower.com/

[9] https://www.u-battery.com/

[10] https://www.bwxt.com/

[11] https://www.usnc.com/

[12] J.J. Powers, W.J. Lee, F. Venneri, L.L. Snead, C.K. Jo, D.H. Hwang, J.H. Chun, Y.M. Kim, K.A. Terrani, Fully Ceramic Microencapsulated (FCM) Replacement Fuel for LWRs, ORNL/TM-2013/173, KAERI/TR-5136/2013 (2013).

[13] N.M. George, I. Maldonado, K. Terrani, A. Godfrey, J. Gehin, J. Powers, Neutronics studies of uranium-bearing fully ceramic microencapsulated fuel for pressurized water reactor, Nuclear Technology 188, p. 238-251 (2014).

[14] K. A. Terrani, L.L. Snead, J.C. Gehin, Microencapsulated fuel technology for commercial light water and advanced reactor application, Journal of Nuclear Materials 427, p. 209-224 (2012).

[15] L.L. Snead, F. Venneri, Y.Kim, K.A. Terrani, J.E. Tulenko, C.W. Forsberg, P.F. Peterson, E.J. Lahoda, Fully Ceramic Microencapsulated Fuels: A Transformational Technology for Present and Next Generation Reactors, Transactions of the American Nuclear Society 104 (2011).

[16] Z.M. Krajewska, W. Gudowski, Raman Spectroscopy Studies of TRISO -Particle Fuel, International Conference on High Temperature Reactor Technology (HTR) 2021, Journal of Physics: Conference Series, 2048 (2021).

[17] B. Zohuri, P. McDaniel, Thermodynamics in nuclear power plant systems, Springer (2015).

[18] Y. Tang, L. Zhang, Q. Guo, J. Cao, J. Tong, Numerical solutions for the kinematic model of pebble flow velocity profiles and its applications in pebble-bed nuclear reactor, Journal of Nuclear Science and Technology 54, p. 991-1001 (2017).

[19] A. Xhonneux, C. Druska, S. Struth, H.J. Allelein, Calculation of the fission product release for the HTR-10 based on its operation history, Proceedings of the HTR 2014, HTR 2014-5-181.

[20] High Temperature Gas Cooled Reactor Fuels and Materials, IAEA-TECDOC-1645 (2010).
[21] F. Guittonneau, A. Abdelouas, B. Grambow, HTR fuel waste management: TRISO separation and acid-graphite intercalation compounds preparation, Journal of Nuclear Materials 402, p. 71-77 (2010).
[22] S.T. Arm, G.B. Hall, G.J. Lumetta, B.E. Wells, Plan for developing TRISO fuel processing technologies, Pacific Northwest National Laboratory PNNL-32969 (2022).
[23] Performance Analysis Review of Thorium TRISO Coated Particles during Manufacture, Irradiation and accident Condition Heating Tests, IAEA-TECDOC- 1761 (2015).
[24] T. Hashimoto, M. Yamamoto, K. Kobayashi, Preparation of Uranium-233 with low Uranium-232 content, Journal of Nuclear Science and Technology 13, p.119-124 (1975).
[25] W. Hoffelner, Materials for nuclear plants – From safe design to residual life assessments, Springer (2013).
[26] L. Luneville, D. Simeone, C. Jouanne, Calculation of radiation damage induced by neutrons in compound materials, Journal of Nuclear Materials 353, p.89-100 (2006).
[27] M.R. Ammar, N. Galy, J.N. Rouzaud, N.Toulhoat, C.E. Vaudey, P. Simon, N. Moncoffre, Characterizing various types of defects in nuclear graphite using Raman scattering: Heat treatment, ion irradiation and polishing, Carbon 95, p.364-373 (2015).
[28] M.A. Amirkhani, M.A. Asadabad M. Hassanzadeh, S.M. Mirvakili, Calculation of dpa rate in graphite box of Teheran Research Reactor (TRR), Nuclear Science and Techniques (2019).
[29] J.C. Sublet, I.P. Bondarenko, G. Bonny, J.L. Conlin, M.R. Gilbert, L.R. Greenwood, P.J, Griffin, P. Helgesson, Y. Iwamoto, V.A. Khryachkov, T.A. Khromyleva, A.Yu. Konobeyev, N. Lazarev, L. Luneville, F. Mota, C.J. Ortiz, D. Rochman, S.P. Simakov, D. Simeone, H. Sjostrand, D. Terentyev, R. Vila, Neutron-induced damage simulations: Beyond defect production cross-section, displacement per atom and iron-based metrics, Eur. Phys. J. Plus 134 (2019).
[30] H.M Qadr, A.M. Hamad, Using of Stopping and Range of Ions in Matter Code to study of radiation damage in materials, Solid State Physics 451 (2020).
[31] A. Hamzah, Suwoto, A. Rohanda, H. Adrial, S. Bakhri, G.R. Sunaryo, Neutron fluence and DPA rate analysis in pebble-bed HTR reactor vessel using MCNP, Journal of Physics Conference Series 962 (2018).
[32] G.F. Naterer, I. Dincer, C. Zamfirescu, Hydrogen production from nuclear energy, Springer (2013).
[33] Technology Roadmap Update for Generation IV Nuclear Energy Systems, OECD Nuclear Energy Agency for the Generation IV International Forum (2014).
[34] Raport Instytutu Sobieskiego „Reaktory jądrowe IV Generacji, Program jądrowy w Stanach Zjednoczonych", Program Polskiej Energetyki Jądrowej Analizy i Opracowania, Departament Energii Jądrowej Ministerstwa Energii (2017).
[35] B.A. Gabaraev, A.V. Lopatkin, I.T. Tretyakov, V.V. Khmelshchikov, V.L. Aksenov, Research reactors – a look into the future, Atomic Energy 103 (2007).
[36] D. Olander, Nuclear fuels – Present and future, Journal of Nuclear Materials 389, p. 1-22 (2009).

[37] G.F. Naterer, I. Dincer, C. Zamfirescu, Hydrogen Production from Nuclear Energy, Springer-Verlag London (2013).
[38] B. Zohuri, P. McDaniel, Thermodynamics in Nuclear Power Plant Systems, Springer International Publishing Switzerland (2015).
[39] E.O. Adamov, Y. Fuji-ie, 58. Development and Tendencies in Fission Reactor Concepts, A. Vertes, S. Nagy, Z. Klencsar, R.G. Lovas, F. Roesch, Handbook of Nuclear Chemistry, Springer (2011).
[40] K. Kugler, Z. Zhang, Modular High-temperature Gas-cooled Reactor Power Plant, 15. Future Aspects of HTR Development, Springer (2019).
[41] H. Ohashi, H. Sato, Y. Tachibana, K. Kunitomi, M. Ogawa, Concept of an inherently-safe high temperature gas-cooled reactor, AIP Conference Proceedings 1448, p.50-58 (2012).
[42] G. Longoni, R.O. Gates, B.K. McDowell, High Temperature Gas Reactors: Assessment of Applicable Codes and Standards, PNNL-20869 (2015).
[43] NGNP Fuel Qualification White Paper, INL/EXT-10-176886 (2010).
[44] C. Kueppers, L. Hahn, V. Heinzel L. Weil, The AVR experimental reactor – development, operation and incidents, Final Report of the AVR Expert Group (2014).
[45] C.C. Bramblett, C.R. Fisher, F.E. Swart, Operational experience at Fort St. Vrain, General Atomic Company (1981).
[46] C.H. Fuller, Fort Saint Vrain operational experience, Public Service Company of Colorado, (1989).
[47] H.L. Brey, Fort St. Vrain operations and future, Energy 16, p. 47-58 (1991).
[48] D.A. Copinger, D.L. Moses, Fort Saint Vrain Gas Cooled Reactor Operational Experience, NUREG/CR-XXX ORNL/TM-2003/223, Oak Ridge National Laboratory (2003).
[49] M. Fisher, Fort St. Vrain decommissioning project, Public Service Company of Colorado (1998).
[50] D.L. Moses, W.D. Lanning, The analysis and evaluation of recent operational experience from the Fort St. Vrain HTGR, IAEA Specialists Meeting on Safety and Accident Analysis for Gas-cooled Reactors (1985).
[51] Evaluation of High Temperature Gas Cooled Reactor Performance: Benchmark Analysis Related to the PBMR-400, PBMM, GT-MHR, HTR-10 and the ASTRA Critical Facility, IAEA-TECDOC-1694 (2013).
[52] R. Li, Z. Liu, Z. Feng, J. Liang, L. Zhang, High-fidelity MC-DEM modeling and uncertainty analysis of HTR-PM first criticality, Front. Energy Res (2022).
[53] J. Zhang, F. Li, Y. Sun, Physical analysis of the initial core and running-in phase for pebble bed reactor HTR-PM, Science and Technology of Nuclear Installations (2017).
[54] B. Kwiecińska, S. Pusz, Pyrolytic carbon – definition, classification and occurrence, International Journal of Coal Geology 163, p.1-7 (2016).
[55] World Nuclear Performance Report 2018, World Nuclear Association Report No. 2018/004 (2018).
[56] A. Chetaine, A. Benchrif, H. Amsil, V. Kuznetsov, Y. Shimazu, Study of some innovant reactors without on-site refueling with TRISO and Cermet fuel, World Academy of Science, Engineering and Technology International Journal of Physical and Mathematical Sciences 6 (2012).

[57] J.J. Powers, B.D. Wirth, A review of TRISO fuel performance models, Journal of Nuclear Materials 405, p. 74-82 (2010).
[58] Y. Oka, H. Madarame, M. Uesaka, An advanced course in nuclear engineering, Springer (2014).
[59] K. Verfondern, H. Nabielek, M.J. Kania, H.J. Allelein, High-Quality Thorium TRISO Fuel Performance in HTGRs, Forschungszentrum Juelich (2013).
[60] M.A. Fuetterer, L. Fu, C. Sink, S. de Groot, M. Pouchon, Y.W. Kim, F. Carre, Y. Tachibana, Status of the very high temperature reactor system, Progress in Nuclear Energy 77, p. 266-281 (2014).
[61] P.A. Demkowicz, B. Liu, J.D. Hunn, Coated particle fuel: Historical and current progress, Journal of Nuclear Materials 515, p. 434-450 (2019).
[62] J.D. Balcomb, L.A. Booth, High-temperature nuclear reactors as an energy source for hydrogen production, Los Alamos Scientific Laboratory of the University of California (1975).
[63] S. Furui, L. Yong, G. Qiang, On power refueling management of HTR-PM, Proceedings of the HTR, Paper HTR2014-5130 (2014).
[64] P.A. Demkowicz, E.L. Reber, D.M. Scates, L. Scott, B.P. Collin, First high temperature safety test of AGR-1 TRISO fuel with Fuel Accident Condition Simulator (FACS) furnace, Journal of Nuclear Materials 464, p. 320-330 (2015).
[65] P.A. Demkowicz, J.D. Hunn, S.A. Ploger, R.N. Morris, Ch.A. Baldwin, J.M. Harp, P.L. Winston, T.J. Gerczak, I.J. van Rooyen, F.C. Montgomery, Ch.M. Silva, Irradiation Performance of AGR-1 High Temperature Reactor Fuel, Nuclear Engineering and Design 306, p.2-13 (2016).
[66] S. Yeo, J. Yun, S. Kim, M.S. Cho, Y.W. Lee, Fabricated methods and anisotropic properties of graphite matrix compacts for use in HTGR, Journal of Nuclear Materials 499, p.383-393 (2018).
[67] X. Zhou, C.H. Tang, Current status and future development of coated fuel particles for high temperature gas-cooled reactors, Progress in Nuclear Energy, 53(2), p.182-188 (2011).
[68] B. Collin, AGR-1 Safety test predictions using the PARFUME code, INL/EXT-12-26014 (2012).
[69] X Energy, LLC Xe-100 Topical Report: TRISO-X Pebble Fuel Qualification Methodology, Project No. 99902071 (2021).
[70] B.P. Collin, D.A. Petti, P.A. Demkowicz, J.T. Maki, Comparison of fission product release predictions using PARFUME with results from AGR-1 safety tests, INL/JOU-15-34147 (2016).
[71] Z.M. Krajewska, T. Buchwald, T. Tokarski, W. Gudowski, Front -end investigations of the coated particles of nuclear fuel samples – ion polishing method, Nuclear Engineering and Technology, Vol.54, p.1935-1946 (2022).
[72] Review of Generation IV Nuclear Energy Systems, Institut de Radioprotection et de Surete Nucleaire (IRSN) (2015).
[73] Uranium Oxycarbide (UCO) Tristructural Isotropic (TRISO) Coated Particle Fuel Performance: Topical Report EPRIAR-1(NP), EPRI, PaloAlto, CA:2019, 3002015750.
[74] A. Sowder, C. Marciulescu, Uranium Oxycarbide (UCO) Tristructural Isotropic (TRISO) Coated Particle Fuel Performance, Topical Report EPRI-AR-1 (NP), Technical Report (2019).

[75] J.D. Arregui-Mena, R.L. Seibert, T.J. Gerczak, Characterization of PyC/SiC interfaces with FIB-SEM tomography, Journal of Nuclear Materials 545, 152736 (2021).
[76] K. Verfondern, H. Nabielek, J.M. Kendall, Coated particle fuel for high temperature gas cooled reactors, Nuclear Engineering and Technology 39 (2007).
[77] I.J. van Rooyen, M.L. Dunzik-Gougar, P.M. van Rooyen, Silver (Ag) transport mechanisms in TRISO coated particle: A critical review, Nuclear Engineering and Design 271, p.180-188 (2014).
[78] I.J. van Rooyen, D.E. Janney, B.D. Miller, P.A. Demkowicz, J. Riesterer, Electron microscopic evaluation and fission product identification of irradiated TRISO coated particles from the AGR-1 experiment: A preliminary review, Nuclear Engineering and Design 271, p.114-122 (2014).
[79] H. Nabielek, P.E. Brown, P. Offermann, Silver release from coated particle fuel, Nuclear Technology 35, p. 483-493 (2017).
[80] B.P. Collin, Diffusivities of Ag, Cs, Sr, and Kr in TRISO fuel particles and graphite, INL/EXT-16-39548 (2016).
[81] T.M. Besmann, R.E. Stoller, G. Samolyuk, P.C. Schuck, S.I. Golubov, S.P. Rudin, J.M. Wills, J.D. Coe, B.D. Wirth, S. Kim, D.D. Morgan, I. Szlufarska, Modeling deep burn TRISO particle nuclear fuel, Journal of Nuclear Materials 430, p. 181-189 (2012).
[82] W.E. Lee, M. Gilbert, S.T. Murphy, R.W. Grimes, Opportunities for Advanced Ceramic and Composites in the Nuclear Sector, Journal of the American Ceramic Society 96, p. 2005-2030 (2013).
[83] L.P. Rodriguez Garcia, D.M. Perez, C.R. Garcia Hernandez, D.E. Milian Lorenzo, C.A. Brayner de Oliveira Lira, Development of a Methodology for the Evaluation of the Thermomechanical Behavior of the TRISO Fuel, INAC (2017).
[84] B.P. Collin, Modeling and analysis of FCM UN TRISO fuel using the PARFUME code, Idaho National Laboratory Fuel Performance & Design, INL/EXT-13-30193 (2013).
[85] G.R. Bower, S.A. Ploger, P.A. Demkowicz, J.D. Hunn, Measurement of kernel swelling and buffer densification in irradiated UCO-TRISO particles, Journal of Nuclear Materials 486, p. 339-349 (2017).
[86] S.A. Ploger, P.A. Demkowicz, J.D. Hunn, J.S. Kehn, Microscopic analysis of irradiated AGR-1 coated particle fuel compacts, Nuclear Engineering and Design 271, p. 221-230 (2014).
[87] G.W. Helmreich, J.D. Hunn, J.W. McMurray, R.D. Hunt, B.C. Jolly, M.P. Trammell, D.R. Brown, B.J. Blamer, T.J. Reif, H.T. Kim, Year one summary of X-energy pebble fuel development at ORNL, ORNL/TM-2017/337 (2017).
[88] F. Charollais, Ch. Perrais, D. Moulinier, M. Perez, M.P. Vitali, Latest achievements of CEA and AREVA NP on HTR fuel fabrication, Nuclear Engineering and Design 238, p. 2854-2860 (2008).
[89] W.W. Delle, K. Koizlik, H. Luhleich, H. Nickel, Quality Control Procedures for HTGR Fuel Element Components. Report, Jül-1333, Research Center Jülich (1976).
[90] H.J. Hantke, Performance of High Quality HTR-LEU Fuel Elements with TRISO Coated Particles – A Summary Report. Internal Report HTA-IB-7/92, Research Center Jülich (1992).
[91] Advances in High Temperature Gas cooled Reactor fuel technology, International Atomic Energy Agency, IAEA-TECDOC-1674 (2012).

[92] P.A. Demkowicz, D. Marshall, J. Palmer, G. Hawkes, J. Sterbentz, TRISO Fuel Experience and Capabilities in the DOE Advanced Gas Reactor Program, ART INL, GAIN-EPRI-NEI Advanced Fuels Workshop March 5-6, Boise State University (2019).
[93] H.X. Xu, J. Lin, J.J Li, Z.Y. Zhu, G.L. Zeng, J.D. Liu, B.C. Gu, B. Liu, Characterization the microstructure and defects of matrix graphite irradiated with Xe ions, Nuclear Instruments and Methods in Physics Research B 406, p. 638-642 (2017).
[94] E.S. Kim, Y.W. Kim, Characterization of 3 MeV H^+ irradiation induced defects in nuclear grade graphite, Solid State Communications 150, p. 1633-1636 (2010).
[95] E. Gyarmati, H. Hoven, A method of Electrolytically Etching Pyrolytic Silicon Carbide, HBK-projekt, Kernforschunsanlage Julich GmbH (1970).
[96] B.A. Budiman, P. Sambegoro, P.N. Halimah, Graphite surface profile with different polishing treatment, Journal Phys.: Conf. Ser.1402 055094 (2019).
[97] Q. Huang, Q. Lei, Q. Deng, H. Tang, Y. Wang, J. Li, H. Huang, L. Yan, G. Lei, R. Xie, Raman spectra and modulus measurement on the cross section of proton-irradiated graphite, Nuclear Instruments and Methods in Physics Research B 412, p. 221-226 (2017).
[98] https://www.struers.com/en/Products/Grinding-and-Polishing/Grinding-and-polishing-equipment/Tegramin#
[99] https://acmin.agh.edu.pl/2017/12/zestaw-do-polerowania-jonowego-powierzchni-plaskich-oraz-wykonywania-przekrojow-poprzecznych-cial-stalych/
[100] O.P. Choudhary, Priyanka, Scanning Electron Microscope: Advantages and Disadvantages in Imaging Components, Ins. J. Curr. Microbiol. App. Sci. 6, p. 1877-1882 (2017).
[101] M. Dunlap, J.E. Adaskaveg, Introduction to the Scanning Electron Microscope: Theory, Practice, & Procedures, Facility for Advanced Instrumentation U.C. Davis (1997).
[102] http://acmin.agh.edu.pl/en/laboratories/18-laboratory-of-transmission-electron-microscopy/37-scanning-electron-microscope-sem-fib-quanta-3d-200i-fei
[103] J.A.M. Belien, F.G. Wouterlood, 1- Confocal Laser Scanning: of instruments, Computer Processing, and Men, Cellular Imaging Techniques for Neuroscience and Beyond, p. 1-34 (2012).
[104] C.B. Johansson, R. Jimbo, K. Roeser, 3.313 – Histological Analysis, Comprehensive Biomaterials 3, p. 215-233 (2011).
[105] http://www.wczt.pl/node/720
[106] P. Finnie, J. Ouyang, J. Lefebvre, Full Spectrum Raman Excitation Mapping Spectroscopy, Scientific Reports 10, 9172 (2020).
[107] M. Drozdowski, Spektroskopia ciała stałego, Wydawnictwo Politechniki Poznańskiej, Poznań (2001).
[108] Z.M. Krajewska, Metodologia wytwarzania sztucznie próchnicy o danym stopniu zaawansowania w szkliwie ludzkich zębów, Inżynierska Praca Dyplomowa, Poznań, (2017).
[109] J.R. Ferraro, K. Nakamoto, C.W. Brown, Introductory Raman Spectroscopy, Academic Press (2003).
[110] T. Dieing, O. Hollricher, J. Toporski, Confocal Raman Microscopy, Springer, Berlin Heidelberg (2010).
[111] https://www.renishaw.com/en/invia-confocal-raman-microscope--6260
[112] https://www.umcs.pl/pl/implantator-jonow,20623.htm#page-1

[113] K. Pyszniak, Wykorzystanie zjawisk towarzyszących bombardowaniu jonowemu w diagnostyce procesu implantacji, Rozprawa doktorska, Narodowe Centrum Badań Jądrowych (2015)
[114] J. Chang, J. Cho, C. Gil, W. Lee, A simple method to calculate the displacement damage cross section of silicon carbide, Nuclear Engineering and Technology 46(4), p. 475-480 (2014).
[115] G.P. Adhikari, H.K. Limbu, Damage formation and calculation of energy loss during implantation of antimony and boron ion in silicon target, JNPS 5 p.103-110 (2019).
[116] H. Liu, W. Ge, Y. Wang, Re-evaluating ion and neutron irradiation data with calculated applicable arc-dpa, Radiation Effects & Defects in Solids 176, p.441-452 (2021).
[117] J.F. Ziegler, M.D. Ziegler, J.P. Biersack, SRIM – The stopping and range of ions in matter, Nuclear Instruments and Methods in Physics Research B 268, p. 1818-1823 (2010).
[118] M.I. Bratchenko, V.V. Bryk, S.V. Dyuldya, A.S. Kalchenko, N.P. Lazarev, V.N. Voyevodin, Comments on DPA calculation methods for ion beam driven simulation irradiations, Voprosy Atomnoj Nauki i Tekhniki. Fizika Radiatsionnykh Povrezhdenij i Radiatsionnoe Materialovedenie (2-84/101), p.11-16 (2013).
[119] U. Saha, K. Devan, S. Ganesan, A study to compute integrated dpa for neutron and ion irradiation environments using SRIM-2013, Journal of Nuclear Materials 503, p.30-41 (2018).
[120] D. Lingis, E. Lagzdina, A. Plukis, R. Plukiene, V. Remeikis, Evaluation of the primary displacement damage in neutron irradiated RBMK-1500 graphite, Nuclear Inst. And Methods in Physics Research B 436, p.9-17 (2018).
[121] W.J. Weber, Y. Zhang, Predicting damage production in monoatomic and multi-elemental targets using stopping and range of ions in matter code: Challenges and recommendations, Current Opinion in Solid State & Materials Science, 23 100757 (2019).
[122] JP. Crocombette, C. Van Wambeke, Quick calculation of damage for ion irradiation: implementation in Iradina and comparisons to SRIM, EPJ Nuclear Sci. Technol. 5, 7 (2019).
[123] M. Akahori, Nuclear handbook, Ohmsha, Tokyo (2007).
[124] Z. Krajewska, M. Górkiewicz, W. Gudowski, Fluence calculations for the TRISO-particle fuel ion implantation experiment - submitted to journal.
[125] M.A. Amirkhani, F. Khoshahval, Evaluation of the radiation damage effect on mechanical properties in Teheran research reactor (TRR) clad, Nuclear Engineering and Technology 52, p. 2975-2981 (2020).
[126] A. Mohammadi, S. Hamidi, M.A. Asadabad, The use of the SRIM code for calculation of radiation damage induced by neutrons, Nuclear Instruments and Methods in Physics Research B 412, p. 19-27 (2017).
[127] J.F. Ziegler, J.P. Biersack, M.D. Ziegler, SRIM The Stopping and Range of Ions in Matter, srim.org
[128] R.E. Stoller, M.B. Toloczko, G.S. Was, A.G. Certain, S. Dwaraknath, F.A. Garner, On the use of SRIM for computing radiation damage exposure, Nuclear Instruments and Methods in Physics Research B 310, p. 75-80 (2013).
[129] M.I. Norgett, M.T. Robinson, I.M. Torrens, A proposed method of calculating displacement dose rates, Nuclear Engineering and Design 33, p.50-54 (1975).
[130] M.A. Kirk, M. Li, D. Xu, B.D. Wirth, Predicting neutron damage using TEM with in situ ion irradiation and computer modeling, Journal of Nuclear Materials 498 (2017).

[131] Y. Iwamoto, S. Meigo, S. Hashimoto, Estimation of reliable displacement-per-atom based on athermal-recombination- corrected model in radiation environments at nuclear fission, fusion and accelerator facilities, Journal of Nuclear Materials 538, 152261 (2020).
[132] E.A. Read, C.R.E. de Oliveira, A functional method for estimating DPA tallies in Monte Carlo Calculations of Light Water Reactors, International Conference on Mathematics and Computational Methods Applied to Nuclear Science and Engineering (M&C 2011) Rio de Janeiro, RJ, Brazil, May 8-12 (2011).
[133] A.Yu. Konobeyev, U. Fischer, Yu. A. Korovin, S.P. Simakov, Evaluation of effective threshold displacement energies and other data required for the calculation of advanced atomic displacement cross-sections, Nuclear Energy and Technology 3, p.169-175 (2017).
[134] B.J. Cowen, Radiation effects in metal oxides and carbides, nuclear Engineering ETDs, University of New Mexico UNM Digital Repository (2018).
[135] D. Guo, Ch. He, H. Zang, P. Zhang, L. Ma, T. Li, X. Cao, Re-evaluation of neutron displacement cross sections for silicon carbide by a Monte Carlo approach, Journal of Nuclear Science and Technology 53,p.161- 172 (2016).
[136] J. Gao, S. Lv, Y. Zhao, D. Chen, Z. Li, Simulation of primary knock-on atom distribution in HTGR graphite under neutron and ion irradiation, Nuclear Inst. And Methods in Physics Research B 492, p.15-22 (2021).
[137] B. Dacus, B. Beeler, D. Schwen, Calculation of threshold displacement energies in UO_2, Journal of Nuclear Materials 520, p. 152-164 (2019).
[138] Z.M. Krajewska, T.Buchwald, A. Droździel, W. Gudowski, K. Pyszniak, T. Tokarski, M. Turek, Mechanical defects in the TRISO-article covering layers obtained through the ion implantation process - submitted to journal.
[139] H. Zhang, Mechanical and microstructural study of silicon carbide and pyrolytic carbon coatings in TRISO fuel particles, PhD thesis – University of Menchester (2012).
[140] A.C. Ferrari, Raman spectroscopy of graphene and graphite: Disorder, electron -phonon coupling, doping and nonadiabatic effects, Solid State Communication 143, p. 47-57 (2007).
[141] A.C. Ferrari, J. Robertson, Interpretation of Raman spectra of disordered and amorphous carbon, Physical Review B 61 (2000).
[142] L.G. Cancado, A. Jorio, E.H. Martins Ferreira, F. Stavale, C.A. Achete, R.B. Capaz, M.V.O. Fho, A. Lombardo, T.S. Kulmala, A.C. Ferrari, Quantifying defects in graphene via Raman spectroscopy at excitation energies, Nano Letters 11, p.3190-3196 (2011).
[143] K. Nakamura, M. Kitajima, Ion-irradiation effects on the phonon correlation length of graphite studied by Raman spectroscopy, Physical Review B 45 (1992).
[144] A. Kaniyoor, S. Ramaprabhu, A Raman spectroscopic investigation of graphite oxide derived graphene, AIP Advances 2, 032183 (2012).
[145] Z.M. Krajewska, T.Buchwald, A. Droździel, W. Gudowski, K. Pyszniak, T. Tokarski, M. Turek, The Influence of the Ion Implantation on the Degradation level of the Coated Particles of Nuclear Fuel Samples, Coatings 13, 556 (2023).
[146] Irradiation damage in graphite due to fast neutrons in fission and fusion systems, IAEA-TECDOC-1154 (2000).
[147] M. Lasithiotakis, B.J. Marsden, T.J. Marrow, Annealing of ion irradiation damage in nuclear graphite, Journal of Nuclear Materials 434, p. 334-346 (2013).

[148] M. Yuan, X. Zhang, A.M.A. Saeedi, W. Cheng, Ch. Guo, B. Liao, X. Zhang, M. Ying, G.A. Gehring, Study of the radiation damage caused by ion implantation in ZnO and its relations to magnetism, Nuclear Inst. And Methods in Physics Research Section B 455, p.7-12 (2019).
[149] T. Kimata, K. Kakitani, S. Yamamoto, T. Yamaki, T. Terai, K.G. Nakamura, Raman spectroscopy of Ar^+ -irradiated graphite surfaces supporting platinum nanoparticles, Nuclear Inst. and Methods in Physics Research B 444, p.6-9 (2019).
[150] Z. Li, D. Chen, X. Fu, W. Miao, Z. Zhang, The influence of pores on irradiation property of selected nuclear graphites, Advances in Materials Science and Engineering 3 (2012).
[151] H. Gupta, K. Joshi, S.K. Gautam, R.G. Singh, F. Singh, Raman scattering from irradiated nanocrystalline zinc oxide thin films: Perspective view on effects of energy loss, ion fluence and ion flux, Vacuum 181, 109598 (2020).
[152] P. Wegierek, J. Pastuszak, Application of Neon Ion Implantation to Generate Intermediate Energy Levels in the Band Gap of Boron-Doped Silicon as a Material for Photovoltaic Cells, Materials 14, 6950 (2021).
[153] R.A.Hakvoort, A.van Veen, J. Noordhuis, J.Th.M.de Hosson, Defect profiling of neon-implanted and laser-melted steel by positron annihilation, Surface and Coatings Technology Volume 66, Issues 1–3 (1994).
[154] E. Oliviero S. Peripolli L. Amaral, P.F.P. Fichtner, M.F. Beaufort, J.F. Barbot, S.E. Donnelly, Damage accumulation in neon implanted silicon, Journal of Applied Physics 100(4):043505 (2006).
[155] S. Taller, G. Van Coevering, B.D. Wirth, G.S. Was, Predicting structural material degradation in advanced nuclear reactors with ion irradiation, Scientific Reports 11, 2949 (2021).
[156] J. Cetnar, W. Gudowski, J. Wallenius, MCB: A continuous energy Monte Carlo Burnup simulation code, Actin. Fission Prod. Partit. Transmutat 30, EUR 18898 EN, OECD/NEA, p. 523–527 (1999).
[157] J. Cetnar, W. Gudowski, J. Wallenius, MCB1C: Monte-Carlo Continuous Energy Burnup Program Release to Nuclear Energy Agency Data Bank, Package-ID: NEA-1643.
[158] T. Lambert, B. Grover, P. Guillermier, D. Moulinier, F. I. Huart, AGR-2: The first irradiation of French HTR fuel in Advanced Test Reactor, Nuclear Engineering and Design 251, p.360-368 (2012).
[159] R.E. Nightingale, Graphite: Advantages, Limitations, and Applications, Battelle Memorial Institute, Pacific Northwest Laboratory, Richland, Washington (1966).
[160] G. Zheng, P. Xu, K. Sridharan, T. Allen, Characterization of structural defect in nuclear graphite IG-110 and NBG-18, Journal of Nuclear Materials 446, p.193-199 (2014).
[161] J.R. Lamarsh, A.J Baratta., Introduction to Nuclear Engineering, Prentie Hall, Upper Saddle River, New Jersey (2001).
[162] H.J. Steffen, D. Marton, J.W. Rabalais, Displacement energy threshold for Ne+ irradiation of graphite, Physical Review Letters (1992).
[163] G.L. Montet, Threshold energy for the displacement of atoms in graphite, Carbon, p.19-23 (1967).
[164] T. Iwata, T. Nihira, Atomic Displacement by electron irradiation in pyrolytic graphite, Journal of the Physical Society of Japan Vo.31 (1971).

[165] F. Vukovic, J.M. Leyssale, P. Aurel, N. A. Marks, Evolution of threshold displacement energy in irradiated graphite, Physical Review Applied 10, 064040 (2018).
[166] K. Nordlund, S.J. Zinkle, A.E. Sand, F. Granberg, R.S. Averback, R.E. Stoller, T. Suzudo, L. Malerba, F. Banhart, W.J. Weber, F. Willaime, S.L. Dudarev, D. Simeone, Primary radiation damage: A review of current understanding and models, Journal of Nuclear Materials 512, p.450-479 (2018).
[167] A.J. McKenna, T. Trevethan, C.D. Latham, P.J. Young, M.I. Heggie, Threshold displacement energy and damage function in graphite from molecular dynamics, Carbon 99, p.71-78 (2016).
[168] G.W. Egeland, J.A. Valdez, S.A. Maloy, K.J. McClellan, K.E. Sickafus, G.M. Bond, Heavy-ion irradiation defect accumulation in ZrN characterized by TEM, GIXRD, nanoindentation, and helium desorption, Journal of Nuclear Materials 435, p.77-87 (2013).
[169] B. Abyshev, A.L. Kozlovskiy, K.S. Zhumadilov, A.V. Trukhanov, Study of radiation embitterment and degradation processes of Li2ZrO3 ceramic under irradiation with swift heavy ions, Ceramics 5(1), p.13-23 (2021).
[170] J.M. Vallerot, X. Bourrat, A. Mouchon, G. Chollon, Quantitative structural and textural assessment of laminar pyrocarbons through Raman spectroscopy, electron diffraction and few other techniques, Carbon 44, p. 1833-1844 (2006).
[171] D. Helary, O. Dugne, X. Bourrat, Advanced characterization techniques for SiC and PyC coatings on high-temperature reactor fuel particles, Journal of Nuclear Materials 373, p.150-156 (2008).
[172] M.S. Dresselhaus, A. Jario, A.G. Souza Filho, R. Saito, Defect characterization in graphene and carbon nanotubes using Raman spectroscopy, Phil. Trans. R. Soc. A 365, p. 5355-5377 (2010).
[173] L.G. Cancado K. Takai, T. Enoki, M. Endo, Y.A. Kim, H. Mizusaki, A. Jorio, L.N. Coelho, R. Magalhaes-Paniago, M.A. Pimenta, General equation for the determination of the crystallite size L_a of nanographite by Raman spectroscopy, Applied Physics Letteres 88, 163106 (2006).
[174] E. Demir, M.N. Mirzayev, E.P. Popov, P. Horodek, I.G. Genov, K. Siemek, D. M. Mirzayeva, V.A. Turchenko, M. Bulavin, A.I. Beskrovnyi, A.H. Valizade, H. V Akhundzada, S.I. Karaaslan, Effect of high-energetic 3H+ ion irradiation on tungsten-based composites, Vacuum 184, 109934 (2021).
[175] M.A. Pimenta, G. Dresselhaus, M.S. Dresselhaus, L.G. Cancado, A. Jorio, R. Saito, Studying disorder in graphite-based systems by Raman spectroscopy, Physical Chemistry Chemical Physics 9, 1276-1291 (2007).
[176] N.J. Dutta, S.R. Mohanty, N. Buzarbaruah, M. Ranjan, R.S. Rawat, Self-organized nanostructure formation on the graphite surface induced by helium ion irradiation, Physics Letters A 382, p. 1601-1608 (2018).
[177] E. Lopez-Honorato, P.J. Meadows, P. Xiao, Fluidized bed chemical vapor deposition of pyrolytic carbon – I. Effect of deposition conditions on microstructure, Carbon 47, p. 396-410 (2009).